PERVASIVE SHOCK-MELTING AT >65 GPa IN A MARTIAN BASALT, THE SHERGOTTITE NORTHWEST AFRICA 14672

Roger Hewins, H. Leroux, D. Jacob, S. Pont, O. Beyssac, V. Malarewicz, J.-P. Lorand, P. -M. Zanetta, B. Zanda

To cite this version:

Roger Hewins, H. Leroux, D. Jacob, S. Pont, O. Beyssac, et al.. PERVASIVE SHOCK-MELTING AT >65 GPa IN A MARTIAN BASALT, THE SHERGOTTITE NORTHWEST AFRICA 14672. 2023. hal-04125476

HAL Id: hal-04125476
https://hal.science/hal-04125476v1

Preprint submitted on 13 Jun 2023

PERVASIVE SHOCK-MELTING AT >65 GPa IN A MARTIAN BASALT, THE SHERGOTTITE NORTHWEST AFRICA 14672

R.H. Hewins[1,2], H. Leroux[3], D. Jacob[3], S. Pont[1], O. Beyssac[1], V. Malarewicz[1], J.-P. Lorand[4], P.-M. Zanetta[5] and B. Zanda[1]

[1]IMPMC, Sorbonne Université, MNHN, UMR CNRS7590, F-75005 Paris, [2]Earth and Planetary Sciences, Rutgers University, Piscataway, NJ 08854, USA, [3]Univ. Lille, CNRS, INRAE, Centrale Lille, UMR 8207 - UMET - Unité Matériaux et Transformations, F-59000 Lille, [4]LPG Nantes, UMR CNRS 6112, Univ. Nantes, F-44322 Nantes. [5]Lunar and Planetary Laboratory, University of Arizona, Tucson, AZ, USA.

Special Issue for Ed Scott

Abstract—Shergottites have provided abundant information on the volcanic and impact history of Mars. Northwest Africa (NWA) 14672 contributes to both of these aspects. It is a vesicular ophitic depleted olivine-phyric shergottite, with average plagioclase $An_{61}Ab_{39}Or_{0.2}$. It is highly ferroan, with pigeonite compositions $En_{49-25}Fs_{41-61}Wo_{10-14}$ like those of basaltic shergottites, e.g. NWA 12335. Olivine (Fo_{53-15}) has discrete ferroan overgrowths, more ferroan when in contact with plagioclase than when enclosed by pyroxene. The pyroxene (a continuum of augite, subcalcic augite, and pigeonite) is patchy, with ragged 'cores' enveloped or invaded by ferroan pyroxene. Magma mixing may be responsible for capture of olivine and formation of pyroxene mantles. The plagioclase is maskelynite-like in appearance, but the original laths were (congruently) melted and the melt partly crystallized as fine dendrites. Most of the 14% vesicles occur within plagioclase. Olivine, pyroxene, and ilmenite occur in part as fine aggregates crystallized after congruent melting with limited subsequent liquid mixing. There are two fine-grained melt components, barred plagioclase with interstitial Fe-bearing phases, and glass with olivine dendrites, derived by melting of mainly plagioclase and mainly pyroxene, respectively. Rare silica particles contain coesite and/or quartz, and silica glass. The rock has experienced >50% melting, compatible with peak pressure >~65 GPa. It is the most highly shocked shergottite so far, at shock stage S6/7. It may belong to the group of depleted shergottites ejected at ~1 myr from Tooting Crater.

INTRODUCTION

A planetary origin for some igneous meteorites (nakhlites) was first suggested by Papanastassiou and Wasserburg (1974) and Reid and Bunch (1975), and a Mars source was generally accepted after Mars atmosphere was found trapped in another meteorite (shergottite; Bogard and Johnson, 1983; Pepin, 1985). Current work with the Perseverance rover is dramatically changing the study of Mars, with the discovery of olivine-rich rocks (Liu et al., 2022; Wiens et al., 2022) resembling chassignite and nakhlite meteorites. The close similarity of Jezero olivine cumulate (Liu et al., 2020) to the chassignite NWA 8694 (Hewins et al., 2021) provides a proof, if any were still needed, that these meteorites come from Mars. However, for now, meteorites are the only samples from Mars that we can analyze exhaustively in our laboratories. These are mainly mafic and ultramafic igneous rocks, which yield details of Mars history, particularly of basaltic volcanism. The most abundant (>200 samples) of these are the shergottites (Udry et al., 2020), followed by nakhlites (Udry and Day, 2018) and then chassignites (Hewins et al., 2020), probably formed in shield volcano systems. Isotopic studies show that one group of shergottites (depleted in incompatible elements) formed during > 2 Gyr from a single volcanic center (Lapen et al., 2017). Comparison of meteorite and crater ages indicates that shergottites formed in the Tharsis volcanic province (Lagain et al., 2021). Differences in incompatible element abundances in these meteorites indicate the nature of different mantle sources of magma (Day et al., 2018).

There are three main mineralogical types of shergottite, poikilitic, olivine-phyric and basaltic and, relative to nakhlites and chassignites, they experienced more shock metamorphism. Northwest Africa (NWA) 14672 is interesting because it combines some of the characteristics of fine-grained olivine-phyric and basaltic shergottites, and indeed is even slightly poikilitic, but even more interesting because it is heavily shocked. The shock metamorphism of martian rocks has proved very useful in deciphering their geologic history and the details of the impact(s) that caused their ejection from Mars. The young ages indicated by internal isochrons for shergottites might reflect recent resetting by impacts, rather than the Noachian crystallization ages proposed by Bouvier et al. (2009). However, since a primary baddeleyite in shergottite NWA 5298 was dated at ~173 Myr from U-Pb systematics, but had been partly transformed by shock to zircon at 22 Myr, the young shergottite mineral isochron ages were validated (Moser et al., 2013).

Most shergottites are moderately or strongly shocked, some with recrystallization giving neoblasts (Darling et al., 2016) and many with high pressure polymorphs, indicating shock stage 5 (Fritz et al., 2017). Most have only relatively small-scale impact melt pockets and veins with a few exceptions, e.g. NWA 1950 (Walton and Herd, 2007). The trapping of martian atmosphere in a shergottite was due to impact producing glass veins (Bogard and Johnson, 1983; Pepin, 1985). The sole martian impact breccia NWA 7034/7533 has impact melt clasts and spherules (shock stage 7; Stöffler et al., 2018) crystallized at ~4.4 Gyr, mixed with unshocked crystal clasts, etc. (Humayun et al., 2013; Hewins et al., 2017). There must be a transition stage 6/7 between heavily shock melted but still coherent rocks (S6) and whole-rock melts (S7) as accumulated in NWA 7533 (Hewins et al., 2017), particularly for mafic rocks (Stöffler et al., 2018). Here we show that shergottite NWA 14672 is such a rock, and more heavily shocked than other shergottites.

ANALYTICAL METHODS

All investigations were carried out on a polished section showing ~1cm^2 of shergottite.

Scanning electron microscopy (SEM)

Global or local textural and chemical examination of the sample were performed with a field emission gun environmental microscope equipped with two opposed X-ray spectrometers (FEG-ESEM/dual-EDS) on the *Plateforme de Microscopie Electronique* of the *Muséum National d'Histoire Naturelle* (Paris, France). The FEG-ESEM is a last generation TESCAN CLARA model coupled with two BRUKER X-Flash EDS detectors characterized by a resolution of 133 eV and a total collecting area of 60 mm^2. Mapping of the whole polished-section using backscattered electrons (BSE) and EDS was conducted using the Spirit 2.3 software stitching module under an accelerating voltage of 15kV and a beam current of 10 nA. Each BSE/EDS tile covers an area of 1024x1024 µm^2 and was acquired using a dwell time of 64µs/pixel. More local information concerning chemical zoning and micro textural chemistry were obtained with single EDS hypermaps (one spectrum per pixel) acquired under an accelerating voltage of 15kV and a beam current of 1 nA or point analyses using the same voltage but a beam current of 300 pA. Quantitative analyses of sulfides were made using the Phi-Rho-Z procedure. A phase map was obtained using the method of Zanetta et al. (2019). High resolution images were also acquired using a FEGSEM JEOL JSM-7800F LV at the

University of Lille equipped with an EDX/EBSD Aztec system from Oxford Instruments and a silicon drift detector (SDD XMaxN) of 80 mm².

To resolve fine-grained intergrowths of sulfides with other phases, chemical analyses of sulfides were made on the MNHN SEM using a PhiRoZ EDS procedure at high magnification, following Lorand et al. (2018).

Electron Microprobe (EMP)

All quantitative mineral analyses except those of sulfides were made by wavelength-dispersive spectrometry on the Cameca SXFive electron microprobe equipped with an LaB_6 source at the Plateforme Camparis of the Université Sorbonne. Analytical conditions were mainly 15keV and 10 nA, with a focused beam. Five-micron rasters were used to estimate the bulk composition of fine-grained components. Dwell time was 10 sec for peaks and backgrounds, increased to 20 or 60 sec for some minor elements, e.g. Mn and Cr. We used silicate, oxide and phosphate standards. Kα lines were measured on standards using diffracting crystals as follows: Na, albite LTAP; Mg olivine LTAP; Si olivine TAP; Al orthoclase LPET; K orthoclase LTAP; Ca, diopside LPET; Ti, MnTiO3; Cr, Cr2O3 PET; Mn, MnTiO3LLIF;Fe, FeS2 LLIF; F, apatite LTAP; P, apatite LPET; Cl, scapolite PET; F (sic) CaF2 TAP; Ni NiO LLIF. The calibrations were checked with San Carlos and Eagle Station internal standards.

Transmission electron microscopy (TEM)

TEM characterization was conducted on a granular pyroxene and a granular ilmenite aggregate. TEM samples about 100 nm thick were prepared by the focused ion beam (FIB) technique using an FEI Strata DB 235 at IEMN (University of Lille). The samples were studied using a Thermo Fisher Scientific^{TM} Tecnai G2-20 operating at 200 kV for conventional bright field imaging, for selected area electron diffraction (SAED) and for automated crystal orientation mapping (ACOM) using the ASTAR^{TM} tool (Rauch and Véron, 2014). The samples were also studied using Thermo Fisher Scientific^{TM} Titan Themis operating at 300 kV for high angle annular dark field (HAADF) imaging and for energy dispersive X-ray spectroscopy (EDXS) analyses. For EDXS, the Titan Themis microscope is equipped with a four-quadrant, windowless, super-X SDD detector system. EDXS data were acquired as hyperspectral maps. Quantification of regions of interest was achieved by applying k-factors and absorption corrections. K-factors for the major elements O, Mg, Al, Ca, Ti and Fe were experimentally determined using standards. “Point” analyses were made of selected areas (ROI) 200x200 nm square.

Raman Spectroscopy

Raman spectroscopy was carried out using a continuous-wave Raman microspectrometer Renishaw InVia Reflex (IMPMC Paris). Analyses were performed using a green 532 nm solid-state laser focused on the sample through a Leica DM2500 microscope with short-working distance objectives 50X (NA = 0.75) and 100X (NA=0.85). This configuration yields a planar resolution of ≈1 µm for a laser power delivered at the sample surface set at less than 1 mW using neutral density filters to prevent irreversible thermal damage (Fau et al., 2019). All measurements were performed with a circularly polarized laser using a ¼-wave plate placed before the microscope in order to minimize polarization effects. The Raman signal was dispersed by a grating with 2400 lines per mm and the signal was analyzed with a RENCAM CCD detector. The spectral resolution for visible light was 1–1.9 cm^{-1} and the wavenumber accuracy was better than 0.5 cm^{-1}. For Raman mapping and the acquisition of hyperspectral maps, the sample was moved with an appropriate step size using an XYZ Renishaw motorized stage. Laser focus was optimized by correcting topographic variation prior to analysis (surface mode using the Renishaw Wire 4.3 software) and all maps were processed using the Wire 4.3 software. More about Raman mapping can be found in Bernard et al. (2009). All spectra were measured directly on the polished section at room temperature.

OVERVIEW OF METEORITE

Textures

Back-scattered electron **(**BSE) and phase maps of the whole section of NWA 14672 are shown in Fig. 1a,b, but the variations in texture are seen better in Fig. 2a,b. This is a vesicular ophitic olivine-phyric shergottite (Fig. 2a) but it has complex fine-grained portions (Fig. 2b). Feldspar (dark blue) with vesicles (black), and fine-grained components, violet or purple in the phase map Fig. 1b, are present throughout the section. Olivine cores (red) and overgrowths (orange) can be seen in this image. Multispectral mapping (Zanetta et al., 2019) gives 6.9% olivine (2.5% magnesian, 4.4% ferroan), 25.7% pyroxene, 31.9% plagioclase, 3.6% merrillite,1.9% accessory phases, 14.9% fine-grained components (labelled “glass” for convenience; this is a minimum estimate as they were in part resolved into their constituent phases), and 14.8% vesicles plus cracks (Fig. 1b). An estimate of vesicle abundance from the BSE map is 12%.

The feldspar occurs mainly as maskelynite (e.g. Fig. 2a), as in Shergotty (Tschermak, 1872) and other shergottites where it is smooth, lacks cracks, but has some schlieren, and is interpreted as formed by quenching of a melt to a glass (e.g. Chen and El Goresy, 2010). Though the term maskelynite is also applied to diaplectic glass (e.g. Stöffler et al., 1986) we see no evidence of amorphization of plagioclase in the solid state in this meteorite. Therefore, we consider glass of plagioclase composition (maskelynite) to be quenched melt. Much feldspar became glass pseudomorphous after plagioclase originally crystallized as laths embedded ophitically in pyroxene, as seen in low magnification BSE images. In addition, barred plagioclase occurs in the fine-grained melt component. Raman spectroscopy shows that plagioclase (including some that looks like maskelynite glass), poorly crystallized plagioclase (dendritic) and glass (maskelynite) are present (Fig. 3).

Olivine is irregular in form, mainly ~500 µm in longest dimension, much more anhedral than in typical olivine-phyric shergottites, and partly enclosed by poikilitic pyroxene (Fig. 4). A large phenocryst near the bottom apex of the section (Fig. S1) is subhedral but its rim has irregular extensions, and it contains enclaves of fine-grained material. In some cases, the olivine is seen to be aggregates of smaller microphenocrysts within pyroxene, or chains of highly anhedral grains (Fig. 4f). Olivine has irregular ferroan outer mantles and core - mantle contacts are abrupt in some cases but gradational in others. Pyroxene occurs mainly as anhedral masses, in many cases with patchy zoning, consisting of irregular low-Z pyroxene within ferrroan pigeonite (e.g. Fig. 4b,d); this is discussed in detail in a later section).

Merrillite (3.6% of the section, Fig. 1b) is anhedral, either smooth and sausage shaped, or angular with a few short dendritic growths attached. The vesicles are 5-200 µm in size, occurring mainly in plagioclase. Vesicles within pyroxene and olivine generally appear to be associated with fine-grained material. Minor minerals include chromite (~0.1%), ulvöspinel and ilmenite (1.0%), Fe sulfide (0.7%), silica phases (0.4%), and traces of micron-sized baddeleyite (Fig. S21). The chromite (a few 5-50 µm grains) and ulvöspinel (associated with fine-grained veins) are mainly enclosed by olivine or pyroxene. The other accessories are interstitial, the ilmenite forming blades up to 400 µm long and the silica phases occurring within or in contact with feldspar. The sulfide forms globules with intergrown magnetite. The anhedral and scalloped sulfide blebs documented in other shergottites (Lorand et al., 2005; Baumgartner et al., 2017) are rarely preserved in NWA 14672 (e.g. Fig. 5a), in either the ophitic-textured or the fine-grained parts of the meteorite. Sulfides occur both as irregular grains and especially as spherical bodies in the fine-grained material (Fig. 5a,b).

Mineral Compositions

The mineral assemblage, the FeO/MnO ratio of olivine (53.4, s.d. 2.9, n=41), the FeO/MnO ratio of the pyroxene (34.2, s.d. 2.7, n=56) and the feldspar composition (An_{68-50} $Or_{0.1-0.6}$) are consistent with shergottite. Compositions of the major minerals and spinel are shown in Fig. 6 and Table S1-S4. The range of olivine compositions is Fo_{53-15}, with overlap between large crystals and dendrites. Pyroxene compositions lie in the central region of the quadrilateral with a continuum of augite, sub-calcic augite, and pigeonite for magnesian compositions. The most extreme pyroxene compositions are $En_{49}Fs_{41}Wo_{10}$ (Mg#54) and $En_{35-37}Fs_{22-24}Wo_{39-43}$ (Mg# 61), while the most ferroan pyroxene is $En_{25}Fs_{61}Wo_{14}$ (Mg#29).

Olivine - pyroxene zonation and textural relationships are seen in Fig. 4.The olivine enclosed by the pyroxene may be subhedral, highly irregular, or glomeroporphyritic, and tends to have a restricted range of zoning. Olivine projecting outside pyroxene, or within maskelynite, has highly ferroan margins (Fig. 4a,c). The combined BSE and iron X-ray maps (Fig. S2a,b) show the strong zoning and irregular form of both olivine (a) and pyroxene (b) across the whole section. They also show that olivine inside pyroxene is less Fe-rich, i.e. more magnesian, and olivine rims in feldspar are highly ferroan.

The phosphate is ferromerrillite (Table S4), approximately stoichiometric, $X_{2.8}Ca_{18.2}P_{13.9}O_{56.00}$, where X is Fe, Mn, Mg, and Na, ignoring different site occupancies and possible REE contents (Shearer et al., 2015). An F Kα peak observed in the merrillite was interpreted as due to interference from a third order P Kα line, following McCubbin et al.

(2018). Both spinel (Usp_{85}) and ilmenite (with ~zero hematite component, Table S5)) are very poor in Fe^{3+}. The sulfide consists of fine-grained intergrowths between troilite (FeS) and hexagonal pyrrhotite (Fe_9S_{10}). SEM-EDX analyses with the Phi-Rho-Z procedure were used because of fine grainsize: they give an average metal/sulfur ratio of 0.97±0.02 (mean of 75 analyses) suggesting a very limited amount of vacancies (and low Fe^{3+}) in the pyrrhotite structure (e.g. Wang and Salveson, 2005). Both phases are nearly devoid of Ni in solid solution (<0.5 wt.%) and pentlandite exsolution was not detected. Silica particles contain coesite, quartz, and silica glass (see Raman spectra in Fig. 3); details of silica phases are given at the end of the section "FINE-GRAINED …" below.

FINE-GRAINED MELT REGIONS

Certain parts of the meteorite are dominantly fine-grained, and consist mainly of either dendritic olivine in more or less basaltic glass, or bars of plagioclase intergrown with pyroxene and other phases, associated with large aggregates of olivine or pyroxene. All of these features are individually described in detail below.

The largest fine-grained area is found in Fig. 1a top; it contains fewer and smaller vesicles than elsewhere. It is seen in Fig. 2b to contain a 1 mm wide patch of light grey glass with fine white olivine dendrites, surrounded by grey material with prominent black plagioclase bars. This barred plagioclase component generally separates smooth maskelynite pools (glass and partly dendritic plagioclase, black or dark grey in Fig. 2b, 7a) and both olivine (white) and pyroxene grains, masses, or aggregates.

Fine-grained material occurs elsewhere throughout the section as small interstitial patches, schlieren, teardrops and globules (Fig. 1a; purple in Fig. 2b). These materials, and sulfide globules in them, wet vesicles. Both types, barred plagioclase and olivine dendrite-bearing, may occur in olivine phenocrysts as enclaves or embayments containing vesicles, e.g. in Fig. S2. Fine-grained embayments or veins within pyroxene may also be associated with vesicles. Plagioclase bars also occur locally in regions of glass with olivine dendrites (e.g., in parts of Fig. 2b, and Fig. 7b).

A region incorporating the bottom edge of Fig. 2b was chosen to show the relationship of fine-grained melt to other components (Fig. 8a). The large olivine and pyroxene masses in this region are clearly not single crystals. The barred olivine and dendritic olivine components are associated with granular pyroxene (Fig. 8b,f) and granular ilmenite (Fig. 8d) aggregates, both with various interstitial phases, and olivine dendritic (Fig. 8c,e) aggregates. In addition, the apparent maskelynite patches (Fig. 8a) are partly dendritic grading into barred plagioclase. The bars may be associated with a cellular texture marked by Fe-rich material in the massive feldspar, which is in part an aggregate of plagioclase dendrites (Fig. 8c). Where they abut a pyroxene grain or aggregate (Fig. 8b,d,f) they are accompanied by interstitial pyroxene; similarly, close to olivine the bars are separated by olivine. The minerals of the melt components and crystal aggregates are discussed below with multi-element X-ray maps and TEM observations.

Fine-Grained Melt Products

Glass with Olivine Dendrites

The olivine dendrites in glass (Fig. 9a,c) resemble feather or swallowtail olivine morphologically (Donaldson, 1976; Faure et al., 2003) and a preferred orientation of dendrites is seen locally. The dendrites are ferroan (the larger ones are Fa_{70-74}, analyzed by EMPA but not phosphoran. The composition range is larger if olivine interstitial to plagioclase bars is included, Fa_{59-74}, but this is still smaller than that of larger olivine crystals. Finer dendrites were found to be Fa_{62-80} (by SEM Phi-Rho-Z EDS). Modest normal zoning is evident in Fig. 9d.

The glass is speckled with Fe sulfide globules tens of microns wide to nanometric and too small to be analyzed with the EMP (Fig. 5b). A generation of submicron ulvöspinel dendrites has nucleated on Fe sulfide grains or droplets (Fig. 9b)) and is seen in high resolution BSE in Fig. S3. Both the glass and the barred plagioclase assemblage contain large (up to 100μm) Fe sulfide (FeS-Fe_9S_{10}) globules, often attached to vesicles and enclosing (Ti) magnetite (Fig. 5). These spherical sulfide bodies display fine-scale intergrowths of iron oxides (with variable amounts of Ti) as well as P-rich silicate glass intergrowths where the spherical sulfide blebs are coated by dendritic olivine. Other tiny inclusions inside the pyrrhotite are euhedral ulvöspinel (common), anhedral P-rich olivine and/or pyroxene (rare). All these determinations are based on EDS spectra that provide only semiquantitative information for the fine-grained intergrowths of iron oxides (with variable amounts of Ti) as well as P-rich silicate glass intergrowths where the spherical sulfide blebs are coated by dendritic olivine.

Barred Plagioclase Component

In the barred plagioclase regions (e.g. Fig. 7,8), the bars range in width from submicron to ~25 μm, and are typically 2-5 μm. The plagioclase bars appear to emanate from large crystals or aggregates of pyroxene and olivine (Fig. 2, 8). Barred plagioclase also separates maskelynite pools from domains of glass with olivine dendrites containing olivine or pyroxene phenocrysts or aggregates (Fig. 7c,8a). Locally, maskelynite enclosed ophitically in pyroxene has been converted to barred plagioclase with interstitial pyroxene (Fig. 7d), at plagioclase-pyroxene grain boundaries. Vesicles are seen in the barred plagioclase component (e.g. Fig. 8e). Barred plagioclase regions show large sulfide bodies (up to 100 μm across, usually attached to vesicles) as well as micrometric sulfide disseminated between bars. The uncommon spherical/anhedral bodies display scalloped grain boundaries (Fig. 5a). They contain embayments of host minerals (plagioclase, pyroxene, ülvöspinel and/or silicate glass (Fig. 3a), and myrmekytic intergrowths of sulfide and ulvöspinel.

Barred plagioclase shows the same composition range as large feldspar and is included with it in Fig. 6. The olivine between plagioclase bars is phosphoran (1.8-2.3 wt. % P_2O_5, Fig. S4), the pyroxene weakly phosphoran (0.2-0.8 wt. % P_2O_5); see Tables S1, S2. In contrast, olivine dendrites in glass have 0.27 wt. % P_2O_5, s.d. 0.08, n = 0.08. Vesicles are seen in the barred plagioclase component (e.g. Fig. 8e,9e).

The two melt components are seen in Fig. 9c (BSE) with barred plagioclase (green, at top) in contact with dendrite-rich glass (dark blue) in the composite X-ray map Fig. 9d (Mg, Al, S, Ca, Ti, Fe). The plagioclase does not penetrate into the glass here. Individual X-ray maps are given in Fig. S5. Olivine (zoned orange-red), and plagioclase (green) with yellow-orange pyroxene are obvious, though the minor glass present is not. Fe-Ti oxide and Fe sulfide are coarse enough to be seen in the plagioclase-rich region, where merrillite that was inconspicuous in the BSE image is also seen (in blue, as confirmed by the individual P Kα map (Fig. S5). Thus, the plagioclase bars are set in a multiphase assemblage (apparently with no interstitial olivine in this case) unlike the olivine dendrites set in glass.

In Fig. 9e,f and Fig. S6, a barred plagioclase assemblage is seen adjacent to a large olivine with wide overgrown dendrites(from Fig. 8e): here olivine appears to be the main mineral interstitial to plagioclase. Pyroxene is scarce or absent but Fe sulfide and Fe-Ti oxide are abundant and are also seen along with plagioclase within the massive dendritic olivine aggregate (Fig. S6-Ti-Al). Merrillite (blue in Fig. 9f, mainly black in Fig. S6) resembles fragments of originally larger grains in the barred plagioclase component. The bars grade into a cellular texture marked by Fe-rich material at the top left of Fig. 9e,g (towards massive feldspar). Elsewhere the bars may terminate in glass with olivine dendrites (Fig. 9a,c,g) but here (Fig. 9e,f) they form bridges between large grains in a kind of ladder structure.

Both dendritic olivine and barred plagioclase domains are in contact with another large olivine dendritic aggregate shown in Fig. 9g (BSE) and Fig. 9h (composite X-ray map), and in Fig. S7 (individual X-ray maps).The plagioclase bars on the left side appear to emanate from a feldspar mass off the left edge of the image passing through a cellular zone of higher Z material (Fig. 9g and S9a). Olivine dendrites show preferred orientations in the central glass region, which contains a rounded merrillite grain. In the top left corner there is an angular particle that is low-Z (Fig. 9g), silica-rich (Fig. 9h), and pure silica S7-Si). It is part of a cluster of similar grains that can be located in Fig. 1 (*indicate if higher resolution version is uploaded*) and that is discussed in detail below. FeS and Fe-Ti oxide are abundant in the barred plagioclase regions, less so in the dendritic olivine region.

A region of barred plagioclase close to the olivine of Fig. S1 is surrounded by fibrous pyroxene and contains two pyroxene aggregates. It is shown in Fig. 9i, 9j (the FeAlMgS map), and individual X-ray images (Fig. S8) reveal that feldspar is intercalated with pyroxene, olivine, Fe-Ti oxide and Fe sulfide. The Ca image shows variation in the pyroxene composition, and stubby merrillite needles crossing the material between the plagioclase bars. On the right edge of this region is a fibrous aggregate of pyroxene (though fibers are not resolved here) discussed below.

Bulk Compositions

The bulk compositions (Table S6) of the fine-grained material determined by EMP rastering are seen in Fig. S9 to be picritic or tholeiitic (Le Maitre et al., 1989; Jensen and Pike, 1982). The main chemical differences between the two components are that the barred plagioclase regions are Al-rich and the olivine dendrite-bearing regions are Fe-rich (Fig. 10). The glass with olivine dendrites is highly pyroxene normative, with up to 80 % for the most dendrite-rich glass. The barred plagioclase component is highly plagioclase normative, with subordinate pyroxene. The major element compositions of the fine-grained components, barred plagioclase and glass with olivine dendrites, define an approximate mixing line in Fig. 10 between plagioclase and a 50-50% pyroxene-olivine mixture. Deviations from the simple mixing line for P, Ti, and S are due to the high abundances of merrillite, ilmenite and Fe sulfide (Fig. 10).

Glass with < ~30% FeO is mainly quartz normative and with >30 % FeO mainly olivine normative (Table S6). The barred plagioclase assemblage has less P_2O_5 (3.76%, s.d. 0.16, n = 4) than two estimates of glass composition (4.79, 4.19%, s.d. 0.43, 0.25, n = 5, 4). The norm calculation suggests the presence of ~6% phosphate in the barred plagioclase bulk and ~8% in the glass on average. However, only the olivine associated with the barred plagioclase is phosphoran.

Features Linked to Fine-grained Components

Overgrowths and aggregates

Some apparent crystals within fine-grained regions, especially in barred plagioclase, are fine granular or dendritic aggregates of a single mineral, in part with interstitial crystals of other phases. Such aggregates are a striking feature of NWA 14672. Examples of olivine, pyroxene and ilmenite aggregates are shown in Fig. 8. Large olivine grains adjacent to fine-grained material have coarse dendritic overgrowths that, in turn, become interstitial to plagioclase bars (Fig. 8c,e). Pyroxene granular aggregates (e.g. Fig. 8b,d,f) are likewise associated with fine-grained material. Large masses of patchy zoned pyroxene may also contain regions of fine-grained material.

The region of barred plagioclase, close to the olivine of Fig. S1, and seen in the FeAlMgS map of Fig. 9j, contains a small elongated aggregate of pyroxene and is bordered by another pyroxene aggregate. The Ca image (Fig. S8) shows that the small pyroxene aggregate has a calcic interior and that stubby merrillite needles cross the material between the plagioclase bars. Though it is not clear in Fig. S9i, with high magnification BSE (Fig. S10) the pyroxene is seen to consist of fibrous chains studded with ferroan pyroxene, speckled with an Fe-rich phase and containing interstitial feldspar, similar to pyroxene in Dar al Gani 476 (Greshake and Stöffler, 2000).

We studied the granular pyroxene aggregate of Fig. 8f (and 8d) using TEM techniques. Pyroxene grains are subhedral and have an average size of the order of a micrometer (Fig. 11a). They contain very few internal crystalline defects. Only a few dislocations were detected in some grains. Tweed texture (Fig. 11b) was observed in the pyroxene, with a fluctuation scale of <10 nm but no well-developed exsolution lamellae were observed. Tweed texture in pyroxene reveals that spinodal decomposition occurred, likely acting as a prelude to exsolution, as is commonly observed in rapidly-cooled augite (e.g., Grove, 1982). EDXS mapping shows that the composition of pyroxene grains is highly variable within a given grain (Fig. 11c). The core of the grains is rich in Mg and the Fe concentration gradually increases towards the edges. The periphery of the grains is often enriched in Ca. We used the ACOM (Automated Crystal Orientation Mapping) technique to determine the crystallographic orientation of the pyroxene grains, indexing for a *C*2/*c* structure . None of the orientation maps showed any preferred grain orientation; an example map is shown in Fig. 11d.

The pyroxene composition range is approximately $Fs_{40-65}Wo_{10-30}$ (Table S7, Fig. 11e). This continuum of sub-calcic augite and pigeonite compositions is similar to EMP results (Fig. 6), but it extends to slightly more ferroan compositions and lacks magnesian augite. Interstitial material is scarce and partly located at triple junctions (Fig. 11c). This material is mainly composed of feldspar (~$An_{58,}$ within the range for coarse feldspar), an iron and titanium oxide with Fe/Ti ratio = 2 (likely ulvöspinel), tiny quantities of a silicate phase of dacite-rhyolite composition (Fig. S9), very rich in SiO_2 and Al_2O_3 (Table 7), and tiny Ca-phosphate grains (Fig. 11c). Locally, the ulvöspinel crystallized in the form of very small dendrites.

The ilmenite aggregate located in Fig. 8d is a cluster, about 100 µm long, of euhedral grains embedded in barred plagioclase and pyroxene. The grain size of ilmenite in the aggregate is typically 1-2 µm (HAADF image, Fig. S11a). The phases interstitial to ilmenite crystals are identified in X-ray map Fig. S11b and they resemble those of the barred plagioclase component: the sub-micron interstices contain plagioclase and calcic pyroxene with rare ~100 nm silica-rich particles. The ilmenite grains contain no internal crystalline defects except some small rounded inclusions of silicate (Fig. S11c). These 10-40 nm inclusions in ilmenite (Fig. 8d, S11) are rich in Si, Al and Ca, and probably feldspathic. Fig. S11d shows rare magnetite and a silica-rich phase interstitial to ilmenite.

Patchy Pyroxene

The occurrence of pyroxene as patchily zoned masses of pyroxene rather than simple crystals or aggregates is well known in shergottites (e.g. El Goresy et al., 2013; Orr et al., 2022) and is strongly developed here (e.g. Fig. 4). While ferroan pigeonite and olivine can be recognized in BSE images, magnesian pigeonite, augite, and associated phases (merrillite, glass) have similar grey tones. X-ray images show that patchy pyroxene may be speckled, streaky, laminated or brecciated-looking, with Ca-rich pyroxene (augite) often set in Ca-poor pyroxene (Ca-Mg map, Fig. 12).

An EMP traverse (Fig. S12) was made across part of a patchy pyroxene mass to identify the phases, and it showed only 25-30% (mainly ferroan) pyroxene. A large (~1 mm) patchy pyroxene mass incorporating this traverse is seen in annotated BSE and corresponding X-ray maps (Fig. S13). There are separate relatively magnesian and relatively calcic “cores” that are separated by a mesh of ferroan pyroxene.

X-ray mapping shows that this patchy pyroxene contains fine-grained schlieren of glass with olivine dendrites (speckled in Fig. S13a,b). It is also associated with elongated and undulating merrillite blobs (difficult to distinguish in BSE) intertwined with or enclosing glass containing olivine dendrites and vesicles. The phosphate is unequivocally merrillite with twin Raman peaks at 956 and 971 cm^{-1} and not glass (Fig. 3). These schlieren of glass are in part continuous with the branching films of Fe-rich pyroxene making a network linking vesicles, merrillite, and small pods of barred plagioclase

The highly irregular contact of ferroan (inter patch) pyroxene with “core” pyroxene and the composition variation are illustrated in the individual Ca, Fe, and Mg Kα X-ray maps (Fig. S13 d,e,f), where the % Wo, Fs, and En are also given. The magnesian and calcic “cores” (e.g. pigeonite and augite, En_{48} $Fs_{41}Wo_{11}$ and $En_{38}Fs_{35}Wo_{37}$) are separated by ferroan pigeonite (e.g. $En_{26}Fa_{60}Wo_{14}$). This ferroan patchy pyroxene has a higher Ti/Al ratio (~2) than most of the pyroxene in NWA 14672 (~4), except that interstitial to plagioclase bars (Fig. S14).

Plagioclase/Maskelynite

Feldspars may be easily identified using Raman spectroscopy by a characteristic peak doublet, caused by rotational and bending modes in the tetrahedral frame, found between 470 cm^{-1} and 515 cm^{-1} depending on the mineral composition. Other minor peaks are observed below 400 cm^{-1} (Mernagh 1991 ; Freeman et al. 2008, Bersani et al. 2017). Large feldspar regions in NWA 14672 resemble maskelynite in BSE images, i.e. "the grains are smooth and lack cleavage, cracks, and fractures that pre-date the shock event” (Chen and El Goresy, 2000). However, Raman spectra indicate that they are mainly composed of plagioclase but glass quenched from melted plagioclase melt is also present (Fig. 3). Barred plagioclase also has Raman spectra consistent with plagioclase. In some regions grain boundaries between plagioclase and plagioclase glass are seen in maskelynite-like regions: one such grain shown in Fig. 13a has a plagioclase-like Raman spectrum and a dendritic structure like the barred plagioclase, but without interstitial phases. Fig. S15 shows the region of plagioclase glass with this dendritic plagioclase mass and another smoother mass (partly dendritic), both of which have a broad band centered at about 500 cm^{-1} replacing the plagioclase doublet, as observed in plagioclase shocked to >45 GPa (Fritz et al., 2005b), and suggesting poorly crystalline plagioclase. The smooth grain also has a ~160 cm^{-1} plagioclase band, and both have a peak at ~220-230 cm^{-1} of unknown origin. Barred plagioclase has nucleated from original laths (Fig. 7), and near pyroxene-plagioclase contacts (as in Fig. 7a), in continuity with ‘maskelynite’.

Silica Polymorphs

An Si X-ray map of the section (Fig. S16) made after the discovery of a silica grain in Fig. 9g,h showed the presence of 0.5% SiO_2 particles. We used Raman spectroscopy (Gillet et al., 1990) to identify the polymorphs (Fig. 3, S17). Silica glass is always in the center of the particles, with a rim of fine grained coesite and/or larger grains of quartz (Fig. 13b). Quartz is identified by main Raman bands at ~125, 193, 461 cm^{-1} which are all downshifted compared to reference values. Coesite is identified by main Raman bands at ~114, 173, 266, 427, 520 cm^{-1}, with peaks slightly downshifted. Raman glass exhibits the typical Raman spectrum of glassy silica with a main asymmetric large band in the range 200-540 cm^{-1} and bands at ~603 and 812 cm^{-1}. In many cases (e.g. Fig. 3), it was not possible to obtain a spectrum of pure quartz due to contributions from underlying or adjacent coesite, as with the glassy silica, even using a confocal configuration for the Raman microspectrometer.

Silica particles always occur in association with the impact melt features, mainly with the barred plagioclase component and maskelynite, but also in contact with granular pyroxene aggregates (Fig. S17a). Fine-grained melt veins, some with pyroxene dendrites, have entered some silica particles among fractures and grain boundaries (Fig. 13b, S17a,b). Silica glass with sulfide droplets and nanopores (both ~300 nm) occurs on or near the particle surface in some cases(Fig. 13b, S17b,c).

By comparing BSE images with Raman hyperspectral maps (Fig. S17), we established that coesite is relatively brighter in BSE images, has a higher relief and a mottled surface appearance suggesting an aggregate of tiny grains, while quartz is smooth and subhedral, with moderate relief; silica glass is dark and featureless with low relief (Fig. 13b). Their appearance is similar to those of coesite, quartz and silica glass in a clast in Ries suevite (Fig. 3c of Fazio et al., 2017). Quartz is often surrounded by a film of high-Z glass, containing Si, Fe, Mg, Ca and Na, sometimes with tiny dendrites (Fig. 13b, S17c). The silica glass in many cases occurs in the center of the particle, with coesite and/or and quartz on the margins, in some cases projecting inwards. Based on the EDS Al Kα peak height relative to the Si Kα upper background, quartz contains about half as much Al as coesite and silica glass.

COMPARISON OF PHASE COMPOSITIONS WITH OTHER SHERGOTTITES

Many olivine-phyric shergottites contain subhedral to euhedral microphenocrysts (~500 μm) but lack the irregular ferroan overgrowths seen in NWA 14672. In addition, their phenocryst olivine is much more magnesian ($Fo_{79-61,}$ Papike et al., 2009) than in NWA 14672. Moreover, shergottite-like rocks analyzed using LIBS (Laser Induced Breakdown Spectroscopy) by the Perseverance rover also contain magnesian olivine, Fo_{72-54} (Wiens et al., 2022). The total range of olivine in NWA 14672 is $\mathbf{Fo_{53-15}}$, including overgrowths. Its rim compositions are like those of olivine rims only in a very few other shergottites (e.g. Fo_{58-31} in NWA 5789; Gross et al., 2010). However, the olivine core compositions overlap those of microphenocrysts in one olivine-phyric shergottite, NWA 8686 ($Fo_{51.5}$, 2s.d. 3.5, n = 79); Nicklas et al., 2022).

The pyroxene in NWA 14672 does not match the composition of any other olivine-phyric shergottite exactly: it lacks highly magnesian orthopyroxene and pigeonite, and only its most Mg-rich compositions $En_{41}Fs_{49}Wo_{10}$ and $En_{35-37}Fs_{22-24}Wo_{39-43}$ overlap with the pyroxene compositions of NWA 8686 (Nicklas et al., 2022). In addition, NWA 14672 extends to more ferroan compositions in rims and in veins in patchy pyroxene. The olivine-bearing shergottite-like rocks on Mars (Wiens et al., 2022) contain Ca-poor pyroxene ($En_{44-50}Fs_{40–51}Wo_{3–10}$) and augite ($En_{38-44}Fs_{18–27}Wo_{32–38}$), quite similar to the cores in NWA 14672, but any ferroan rims could probably not be resolved by LIBS. The composition range of NWA 14672 is closest among olivine-phyric shergottites to that of NWA1068/1110 (Barrat et al., 2002; Papike et al., 2009) and even there we see little overlap.

A better match for the pyroxene composition range is found in basaltic/gabbroic shergottites. It is similar to but more ferroan than QUE 94201 (Mikouchi et al.1998; Kring et al., 2003; Papike et al., 2009) and NWA 5298 (Hui et al., 2011; Udry et al., 2017). It is also similar to Shergotty (Stolper and McSween, 1979; Papike et al. 2009) though there the pigeonite and augite have a wide composition gap. The best matches for NWA 14672 pyroxene are to Los Angeles (Rubin et al., 2000; Warren et al., 2004; Papike et al, 2009), Dhofar 378 (Ikeda et al., 2006), NWA 7320 (Udry et al., 2017), and (Fig. S18) NWA 12335 (Orr et al., 2022), though its pyroxene fractionation did not go as far as to produce pyroxferroite.

The merrillite is ferroan, as in QUE 94201 (Mikouchi et al., 1998), and plots close to that of Shergotty on the shergottite Mn fractionation trend of Shearer et al. (2015). However, the Na in merrillite is much lower than the Shearer trend. The average plagioclase composition for NWA 14672 is almost identical to that of QUE 94201 with which it shares the lowest K/Na ratio among the 13 shergottites analyzed by Papike et al., (2009). The K content, $An_{61}Ab_{39}Or_{0.2,}$ is very low and indicates that NWA 14672 is also a depleted shergottite like QUE 94201, NWA 7635, and NWA 8159 (Mikouchi et al., 1998; Irving et al., 2013; Herd et al., 2017). Despite shock melting and vesiculation, maskelynite retains its stoichiometry, consistent with Papike et al. (2009). Like NWA 12335 (Orr et al., 2022), it almost lacks the chromite typical of olivine-phyric shergottites (e.g. Goodrich, 2002), except for a few 5-50 µm grains, but contains ulvöspinel as in QUE 94201 (Kring et al., 2003) and Shergotty (Stolper and McSween, 1979).

To summarize the mineral composition data described above, NWA 14672 resembles the basaltic shergottites, especially Los Angeles and NWA 12335, though it is an olivine-phyric shergottite similar to NWA 8686, but more ferroan. This conclusion is supported by minor phases such as sulfides that compare quite well to basaltic shergottite sulfide in their Ni/Fe ratio (Los Angeles, Shergotty) despite being modified by shock, being even more depleted in Ni than these latter two samples (Lorand et al., 2005; Baumgartner et al., 2017). However, all these mineralogically similar meteorites are enriched shergottites (Udry et al., 2020; Orr et al., 2022), except NWA 8686 and QUE 94201 which are depleted. We therefore conclude that these two are the only shergottites to which NWA 14672 could be genetically related; that is only to either NWA 8686, as a similar but more fractionated basaltic magma with olivine phenocrysts, or to QUE 94201, as a more fractionated olivine-free pyroxene-saturated liquid, that has scavenged olivine autocrysts (“xenocrysts in their own magma”; Peslier et al., 2010).

Few olivine-phyric shergottites have compositions consistent with total liquids that appear not to have incorporated earlier formed crystals. Yamato 980459 (Mikouchi et al., 2004; Shearer et al., 2008; Usui et al., 2009) and NWA 5789 (Gross et al., 2010) are notable exceptions to this, each having an olivine composition in equilibrium with a liquid of the bulk composition; NWA 2990 (Filiberto and Das Gupta, 2011) and NWA 6234 (Gross et al, 2013) are similar but more ferroan examples. Other shergottites appear to have accumulated olivine autocrysts. Thus LAR 06319 appears to be near its parent liquid composition but with10% added olivine modified by diffusion (Peslier et al., 2010; Balta et al., 2013). In NWA 1068, olivine occurs as corroded megacrysts and not in the groundmass, suggesting that the rock formed when a basaltic shergottite liquid accumulated olivine autocrysts (Barrat et al., 2002). Olivine more ferroan than pyroxene in olivine-phyric shergottites, e.g. olivine (Fo_{55-48}) in NWA 8686 (Nicklas et al., 2022) that occurs with pigeonite with Mg# up to 72, is also significant. This disequilibrium is taken as evidence that some basaltic shergottite magmas scavenged olivine autocrysts shortly before their eruption (e.g. Nicklas et al., 2022), thus becoming “olivine-phyric” with no olivine in their groundmass.

In NWA 14672, the olivine enclosed by the pyroxene has varied morphology (Fig. S23, but has a restricted magnesian composition range. Olivine projecting outside pyroxene, or within maskelynite, has highly ferroan margins (Fig. S2). The sharp contacts between olivine core and margin suggest a hiatus – two stages of crystallization: this has been noted for other shergottites (e.g. Yamato 980459, Greshake et al., 2004; LAR 06319, Balta et al, 2013; NWA 12335, Orr et al., 2022). The hiatus could be explained by transport of the magma and continuation of crystallization under different conditions. The ferroan olivine rims are in contact with maskelynite, like the ferroan pigeonite rims. A possible explanation might be that liquid saturated with pyroxene a little less magnesian than those of QUE 94201 encountered and scavenged olivine crystals, giving rise first to partial enclosure by pyroxene and then to formation of the ferroan overgrowths on both phases. Irregularities at some olivine-pyroxene contacts suggest the possibility of corrosion of olivine when scavenged, but olivine crystals enclosed only on one side suggest that olivine was already coated with pyroxene when scavenged.

In magnesian shergottites, the first pyroxene is orthopyroxene or pigeonite that becomes more ferroan before augite crystallizes (e.g. Treiman et al., 1994); on further cooling ferroan pigeonite may crystallize. However, in many basaltic shergottites pigeonite crystallizes only shortly before augite, and then pigeonite and augite co-crystallize (e.g. Stolper and McSween, 1979). The unusual crystallization sequence of pigeonite-augite-pigeonite is explained by strong undercooling of the magma (Mikouchi et al., 1998, 1999) resulting in crystallization on a metastable extension of the pigeonite solidus. This may be due to failure of plagioclase to nucleate causing Ca enrichment (Mikouchi et al., 1999), as previously observed in some Apollo basalts (Papike et al., 1976). The higher Ti/Al ratio of the late ferroan pigeonite is consistent with crystallization simultaneous with or later than plagioclase (Fig. S19). The continuum of compositions of early Mg-rich pigeonite and augite in NWA 14672 suggests a similar origin by undercooling. The simultaneous crystallization of the margins of plagioclase laths and their enclosing pigeonite rims is consistent with the interpretation of Mikouchi et al. (1998, 1999). However, though this trend is seen in other shergottites, the sub-calcic augite compositions may in part be due to a mixture of phases and electron beam overlap, as a complex history is indicated for the patchy pyroxene, as discussed below.

If NWA 14672 formed from an olivine-saturated liquid like NWA 8686, the olivine-pyroxene relationship is particularly hard to explain. If it formed from a pyroxene-saturated liquid like a more fractionated QUE 94201, that has scavenged olivine autocrysts, partial corrosion of olivine could be explained, and perhaps also the complexities of the patchy pyroxene if the magma mixing was energetic.

PHENOMENA RELATED TO SHOCK MELTING

Fine-Grained Melt Components

There are three kinds of fine-grained materials in shergottites: pyroxenoid breakdown material (PBM), normal mesostasis, in some cases with a silica phase (e.g. NWA 6963, Filiberto et al., 2014), and impact melt. Obviously, there is no PBM as Fe-enrichment of pyroxenes is limited, so no pyroxenoid or olivine-silica-augite intergrowths formed. Equally obviously the meteorite is shocked, but there are no crosscutting veins or well-defined melt pockets. However, the “mesostasis” is heterogeneously distributed. Are the fine-grained materials, glass with olivine dendrites and the barred plagioclase assemblage, quenched mesostasis or impact melts? Here we discuss these two components and links between them and features of the major minerals, all of which are consistent with an origin by shock melting.

Glass with Olivine Dendrites

Olivine dendrites are not common in shergottites, but are observed in normal mesostasis glass interstitial to olivine (macro)phenocrysts in Yamato 980459 (Greshake et al., 2004; Mikouchi et al., 2004; Usui et al., 2009). This is the most magnesian olivine-phyric shergottite and is interpreted as representing a total liquid composition. NWA 5789 (Gross et al., 2010) is very similar to Y980459 but crystallized olivine microphenocrysts in the mesostasis, before its radiating/parallel plagioclase and pyroxene. The textural differences are explained by more rapid cooling of Y980459, quenching a still olivine-normative late liquid.

Dendritic olivine is also observed in melt pockets in NWA 1950 (Walton and Herd, 2007) and in a thin shock vein in Tissint (Walton et al., 2014). The interior of the shock vein consists of relatively homogeneous glass and Fe-sulfide spheres, like the host glass of NWA 14672. Interestingly, a vein of shock glass in NWA 4797 (Walton et al., 2012) contains skeletal phosphoran olivine, whereas in NWA 14672 it is observed in the barred plagioclase component, indicating more phosphate was melted for the barred plagioclase than for the glass with olivine component.

In terrestrial basaltic rocks, olivine dendrites in glass are well known where they are associated with high degrees of supercooling and high cooling rates (Faure et al., 2003). First and Hammer (2016) determined cooling conditions reproducing dendrites in basalts experimentally (~100 °C/hr) and suggested that this required formation cooling near surface in a thin flow, such as a pahoehoe toe or flow breakout. Thus, the presence of similar olivine dendrites in NWA 14672, as well as glass, and tweed texture in pyroxene, mean relatively rapid cooling though significantly longer than the shock dwell time.

A signature feature of shock melts is the formation of globular sulfide droplets (e.g. Walton et al., 2010; Baumgartner et al., 2017). Sulfide droplets in impact glass also served as nucleation sites in other shergottites, e.g. QUE 94201 (Mikouchi et al., 2003). Sulfide globules with silicate inclusions were observed in silicate shock melt in shergottite SAU 094 (Gnos et al., 2002). In NWA 14672, the submicron size of many sulfide droplets (Fig. S9) and sulfide-spinel intergrowth suggest rapid exsolution from the silicate melt, a feature not observed in normal shergottite crystallization. Ilmenite in NWA 14672 has zero hematite component, and the spinel is also poor in Fe^{3+}, $Usp_{86}Mag_{11}$ (Table S5). These compositions reflect an overall low fO_2, below the wüstite-magnetite (WM) buffer (e.g. Frost and Lindsley, 1991) as does the sulfide composition indicating a high proportion of troilite component ($Fe_{0.98}S$, EDS and WDS analyses). This is reminiscent of Los Angeles and SaU008, and also the most shocked chassignite NWA 2737 (Lorand et al., 2012).

Barred Plagioclase

Walton et al. (2012) reported that NWA 4797 contains plagioclase that has been completely melted by shock and crystallized radiating ~5 um plagioclase dendrites or laths in glass. Parallel fingers of low-Ca pyroxene and plagioclase extend tens of μm from pyroxene grain margins into maskelynite in NWA 5789 (Gross et al., 2010; Darling et al., 2016). Dendritic plagioclase was also inferred to have crystallized from totally melted primary plagioclase in NWA 6342 (O'Neill et al., 1987; Kizovski et al., 2019), where it is associated with vesicles and veining of pyroxene.

Wang and Chen (2006) reported that bar-shaped plagioclase in GRV 99027 interleaved with narrow pyroxene and olivine crystals crystallized from "liquid plagioclase pools" that had not been quenched to glass, requiring longer cooling than with typical shock dwell times of 10–100 ms (Sharp et al. 2019). This mechanism, with a limited amount of liquid mixing explains the barred plagioclase component in NWA 14672. The preservation of the metastable phase phosphoran olivine (Boesenberg et al., 2012), between the plagioclase bars in NWA 14672, as well as the dendritic textures, shows that the cooling was not really slow, possibly ~100°C/hr (First and Hammer (2016). The frequent departure of plagioclase bars from masses of melted plagioclase (maskelynite) in NWA 14672 is also evidence of crystallization after extensive melting. The scarcity of angular crystal clasts (e.g. Fig. 9f) indicates large regions of near total melting.

Many eucrites display few shock features, mainly fracturing, and lack maskelynite (e.g. Kanemaru et al., 2020). Indeed, very few high-pressure minerals have been found in eucrites, suggesting a small source crater on Vesta (Pang et al., 2016). However, eucrites may also contain shock melt veins (e.g. NWA 10784, Fig. S19). In this genomict breccia, the grainsize of the melt is ~1 μm, but locally there is 10-20 μm plagioclase in a barred to trachytic texture, comparable to the barred plagioclase component in NWA 14672. There are also schlieren of maskelynite. However, there are abundant somewhat rounded pyroxene clasts in NWA 10784, that are lacking in the shergottite, where the aggregates of granular or dendritic pyroxene and olivine probably represent transiently melted clasts. The differences from NWA 14672 are consistent with less intense shock in eucrites, which seems to correspond only to peak conditions S3-S5 (Fritz et al., 2017, Stöffler et al., 2018), suggesting smaller source craters for eucrites than for shergottites (Kanemaru et al., 2020; Ono et al., 2023) .

Crystallization Models

The differences in mesostases in shergottites are partly explained by different cooling rates. The two fine-grained components observed in NWA 14672 have similar textures, but differ in bulk compositions. They are intermingled (e.g. Fig. 1, 6, S2) and there is glass with both olivine and plagioclase dendrites so the differences are not due to cooling history. They might be due to fractionation within the late igneous liquid or to incomplete mixing of shock-generated localized partial melts.

We have calculated liquidus phase relations and fractional crystallization paths for the average bulk compositions (Fig.8, S14) of the two fine-grained components using PetroLog (Danyuchevsky and Plechov, 2011), using similar parameters to those of Hewins et al. (2020). The liquidus phases deduced from textures, plagioclase for the barred plagioclase component, and olivine for the glass with dendrites, are confirmed with liquidus temperatures of 1280 °C and 1114 °C, respectively, at 1 bar and fO_2 of the FMQ buffer. The glass component crystallizes Fe-rich olivine and moves to Si-Al-poor compositions, and the barred plagioclase component crystallizing plagioclase moves to Si-poor, Fe-rich compositions (Fig. S20). No relationship by fractional crystallization is possible.

The normative compositions suggest two coexisting partial melts, one mainly pyroxene-derived and one largely plagioclase-derived. This is consistent with the crossing paths for fractional crystallization of Fig. S20.

As the glass with dendrites has up to 80 % normative pyroxene, the large pool in Figure 1b suggests total melting of a large pyroxene grain and partial mixing with melted plagioclase, etc. The barred plagioclase component is highly plagioclase normative, but with abundant pyroxene and olivine too, suggesting eutectic melting that is consistent with its location between plagioclase and pyroxene or olivine grains (Fig. 2b,8,S7). It appears that initial congruent melting was followed by limited grain boundary melting and/or limited mixing.

Patchy pyroxene

Patchy pyroxene is common in basaltic shergottites, e.g. NWA 856 (El Goresy et al., 2013). In NWA 7320 pigeonite and augite grains appear to make up a network of grains (cores) attached by ferroan rims with irregular, ragged contacts; a lamellar structure indicates exsolution (Udry et al., 2017, their Fig. 2). They also suggested that pyroxene rims in NWA 7320 crystallized after complete crystallization of pigeonite and augite cores. Hui et al. (2011) reported pyroxene cores in NWA 5298 consisting of heterogeneous amoeboid patches containing both pigeonite and augite, which grade into Fe-rich rims; the textures were explained by resorption during magma evolution rather than re-equilibration.

In NWA 14672 it appears that loose clusters of original pyroxene microphenocrysts have been attached by the growth of a late all-pervading rim, consistent with two stages of crystallization. Alternatively, attached clusters might have been penetrated by veins of late liquid. A complex history is indicated for the pyroxene in BSE maps (e.g. Fig. 4) and X-ray maps (Fig. 12, S13) that show not merely patchy but speckled, streaky, laminated brecciated-looking grains. The streaky texture suggests the (former) presence of exsolution lamellae.

The potentially ‘invading’ ferroan pyroxene is accompanied by veins or blobs of glass with dendrites and the barred plagioclase assemblage (e.g. Fig. 7e,f, S17, S23). The latter are offshoots from large fine-grained domains, and are probably shock-derived liquids that have followed the path of late stage liquid crystallizing ferroan pigeonite. These veins may be analogous to the offshoots of maskelynite seen in shergottite pyroxene (Walton et al., 2012). Because rims of ferroan pigeonite are common in less shocked basaltic shergottites, it seems unlikely that they formed from shock-melted pyroxene: impact melting that produces glass with dendrites may require quenching too rapid for the growth of thick rims. This strengthens the argument for very forceful magma mixing.

Granular aggregates

Many accessory minerals of geochemical and geochronological interest occur as granular aggregates at terrestrial impact structures, where they may provide accurate impact ages, though granular silicates have not been noted. These include zircon (McGregor et al., 2018; Cavoisie and Köberl, 2019), apatite (McGregor et al., 2019; Kenney et al., 2019), titanite (McGregor et al., 2020) and monazite (Erickson, 2019), from shocked rocks. They are generally interpreted as neoblasts, due to solid state recrystallization after severe shock deformation. However, granular titanite from the Roter Kamm crater was formed by regional metamorphism (Cavoisie et al., 2022).

Granular aggregates occur in shergottites, e.g. of baddelyite in NWA 5298 (Darling et al., 2016). However, deformation of olivine and pyroxene is usually described as mosaicism or the formation in the solid state of small subgrains with slightly different orientations (Stöffler and Langenhorst, 1994; French and Koeberl, 2010. In NWA 5298, euhedral granules of melt-grown pyroxene with random orientation were also described in association with melt pockets and veins (Darling et al., 2016). There are partial melt zones in LEW 88516 adjacent to melt pockets in which olivine and pyroxene have been converted to small euhedra with interstitial glass (Keller et al., 1992; Treiman et al., 1994). Micron-sized grains in olivine and pyroxene aggregates are seen in NWA 6342, for which a pressure of 60 GPa was estimated (Irving et al., 2011). Aggregates of melt-grown euhedra of chromite in ALH 77005 (Walton and Herd, 2007) also occur. These aggregates are interpreted as crystallized from melts, not from solid state recrystallization, and indicate more intense shock than mosaicism . The above shergottites combine vesiculated plagioclase melt and fine mosaic or granular pyroxene and olivine. This combination appears to define the higher shock stages in shergottites (before total melting). Indeed, recent definitions of shock stage S6 include regrown olivine and vesicular and melted plagioclase (Fritz et al., 2017; Stöffler et al., 2018).

The aggregates in NWA 14672, particularly of olivine, like the melt components, appear more abundant than in other shergottites. They tend to consist of solid crystal-like masses grading outwards with increasingly large pores filled with “mesostasis” to individual granules set (generally) in the barred plagioclase component. The tweed texture in the pyroxene (Fig. 9b) plus the absence of exsolution, and the presence of dendrites of ulvöspinel indicate rapid cooling. The random orientations of the granules (Fig. 9e,) and the chemical zoning of the pyroxene (Fig. 9c) indicate that they are grown from the melt. This is not a texture found in normal volcanic rocks. We interpret them as representing pools of congruently melted pyroxene (or olivine, or ilmenite) that crystallized after being slightly mixed with cotectic or eutectic melt. In some cases, there are dendritic overgrowths on relict grains and on aggregates.

INDICATIONS OF SHOCK LEVEL

Coesite

Coesite is a common phase at terrestrial impact craters, especially well known where porous sandstone occurs in the target, e.g. Meteor crater (Kieffer, 1971). It is also found in crystalline targets, e.g. in granite and gneiss clasts at the Ries (Stöffler, 1971; Fazio et al., 2017), where much of the original quartz is converted to coesite. There has been much discussion of the possible formation mechanisms of coesite. Folco et al. (2018) and Campanele et al. (2021) proposed that coesite at Kamil formed by direct subsolidus transformation from quartz. At Meteor Crater, coesite was interpreted as the product of the inversion of stishovite formed at pressures near 30 GPa (Stöffler and Langenhorst, 1994). Coesite at the Ries crater was also suggested to have formed during pressure release, from a stishovite-like high-pressure phase (Stöffler, 1971). Alternatively, Ries coesite, which has a granular appearance like that in NWA 14672, could have formed by crystallization from high-pressure silica melt (Fazio et al., 2017).

In NWA 14672, the silica particles (mainly silica glass) may be inherited from an original mesostasis phase (e.g. quartz), and they may have been totally melted. Alternatively, a polymorph such as stishovite could be formed in conjunction with mafic minerals such as majorite (of which we have no evidence). Impact may cause single-phase melting (congruent), typically seen in plagioclase/maskelynite, or bulk melting (eutectic) forming melt pockets and ultimately melt rocks. Congruent melting of superheated silicates is extremely rapid. Even 1 mm grains of diopside and anorthite melt in less than 1 sec at 1600°C and 1 bar (Greenwood and Hess, 1966). While quartz is expected to be part of the lowest temperature melting fraction with normal (eutectic or cotectic) melting, its congruent melting point makes it the most refractory phase in a basalt like a ferroan shergottite (Kayama et al., 2018; Fei and Bertka, 1999). If there is congruent melting because of a rapid temperature rise, silica could survive as discrete silica melt particles.

The coesite in NWA 14672 projects from the margins of the particles into the central silica glass (Fig. 10b) along with quartz, consistent with the idea of crystallization from a high-pressure melt. Coesite has been observed in a few other shergottites. In NWA 8159, both stishovite and coesite are present, plagioclase is only partly converted to maskelynite (Herd et al., 2017), and a pressure of 16 GPa was estimated based on the presence of a majorite assemblage (Sharp et al., 2019). In NWA 8657, the coesite was present with quartz and silica glass in shock melt (Hu et al., 2020), as in NWA 14672. Peak conditions were estimated as ~18-30 GPa. Liquid-coesite stability in the system SiO_2 (Kayama et al., 2018) is limited by the triple points with stishovite (~13.3GPa) and with quartz (~4.1 GPa). We derive (below) a decompression curve entering the coesite field between these pressures and passing into the quartz stability field (before the remaining liquid was quenched, based on the model of Hu and Sharp (2022).

Maskelynite and Plagioclase

Maskelynite, a glass of plagioclase composition, is ubiquitous in shergottites and the nature of its formation and the level of shock attained have been much discussed. Maskelynite in terrestrial craters is mainly a diaplectic (solid-state-formed) glass, and was identified in Shergotty by Stöffler et al. (1986). However, O'Neill et al. (1987) showed that igneous feldspar in the shergottite ALH 77005 had been melted by shock and the melt partly crystallized to plagioclase. This interpretation was subsequently confirmed by many. Fritz et al. (2005a) identified vesicles in the glass of ALH 75005. Chen and El Goresy (2010) emphasized that the rare fractured birefringent relicts of plagioclase, evidence of flow, and rare plagioclase dendrites in smooth continuous maskelynite, show that maskelynite in many shergottites was liquid. El Goresy et al. (2013) showed that melt schlieren in maskelynite in NWA 856 commenced at maskelynite-pyroxene contacts as a result of two-phase melting. Fritz et al. (2005b) showed a range of structural states for feldspar in martian meteorites, ranging from diaplectic glass to plagioclase with higher shock conditions. In the shergottite NWA 1950, maskelynite is rimmed by birefringent plagioclase dendrites (Walton and Herd, 2007). In NWA 5298, as in Dhofar 378 (Ikeda et al., 2004), birefringent spherulitic plagioclase was crystallized on the rims of isotropic maskelynite grains (Hui et al., 2011; Darling et al., 2016). Darling et al. (2016) interpreted these spherulitic textures and melt veins in surrounding clinopyroxene, as due to crystallization after impact melting. In many shergottites, including NWA 14672, the smooth glass-like feldspar observed in BSE has to be called 'maskelynite', unless Raman spectra or microscopic dendrites prove otherwise.

Stöffler et al. (1986) used plagioclase refractive index data from shock experiments to calibrate shergottite shock history, and concluded that Shergotty maskelynite was formed at 29 GPa. Takenouchi et al. (2017) also reported maskelynite formation at >29 GPa in shock experiments on olivine-phyric terrestrial basalt. Shock transformation of plagioclase in NWA 5298 (An_{40-55}) to maskelynite was similarly attributed to a shock pressure of at least 29 GPa (Hui et al., 2011). For ALH 77005, one of the most shocked shergottites containing vesiculated maskelynite and post-shock plagioclase, Stöffler et al. (1986) estimated shock pressure of 43 GPa and, in a Raman spectroscopy study, Fritz et al. (2005b) indicated >45 GPa.

Fritz et al. (2005b) measured the Raman spectra of pressure-calibrated SNC feldspars that had experienced shock deformation. They showed peak broadening, disappearance of the plagioclase 510 cm^{-1} peak, and appearance of a ~600 cm^{-1} peak when isotropic maskelynite has formed as diaplectic glass, i. e. at 26-32 GPa, based on Stöffler et al. (1986), ALHA 77005 feldspar (shock pressure > 45GPa), consists of vesiculated maskelynite glass with a very broad ~500 cm^{-1} peak and crystallized plagioclase with both 490 and ~510 cm^{-1} peaks (Fritz et al., 2005b). Note that ‘maskelynite’ contains most of the vesicles in NWA 14672. Raman spectra in part show a single band replacing the plagioclase doublet (Fig. S15) as observed in plagioclase inferred to be shocked to >45 GPa (Fritz et al. (2005b): this may be poorly crystallized plagioclase. It consists of dendritic plagioclase masses and plagioclase glass; it is associated with the fine-grained barred plagioclase component, and glass plus olivine patches and schlieren. In view of the presence of abundant plagioclase with a plagioclase Raman spectrum (Fig. S15), we consider it to be crystallized after strong shock melting at >45 GPa (at least). In this respect the sample resembles NWA 4797, a highly shocked shergottite in which plagioclase was completely melted and quench-crystallized to form plagioclase dendrites in highly vesiculated glass (Walton et al., 2012).

Vesicles

The shergottites containing vesicles are generally considered as among the most heavily shocked. These include Dhofar 378 (Ikeda et al., 2006) and NWA 6342 (Irving et al., 2011; He et al., 2015). In Sayh al Uhaymir (SaU) 094 millimeter-sized vesicles occur throughout the rock, especially in the centers of large shock melt pockets. For NWA 5298, Hui et al. (2011) reported vesicles (up to hundreds of microns in diameter; Darling et al., 2016), in maskelynite grains. El Goresy et al. (2013) reported vesicular maskelynite in ALH 77005, typically rimmed by birefringent plagioclase (Walton and Herd, 2007). In addition, NWA 2975 (Hui et al., 2011; He et al., 2015), and NWA 4797 (Walton et al., 2012) contain vesicles in plagioclase in shock veins and melt pockets. The volatile species in vesicles in maskelynite as in NWA 14672 is not Na because the glass has a stoichiometric plagioclase composition. Because trapped atmospheric gases are found in shergottite shock melts (e.g. Bogard and Johnson, 1983) they are probably the cause of the vesicles in plagioclase melt.

Vesiculated plagioclase glass was not detected by Meyer et al. (2011) in a 50 GPa shock recovery experiment. However, Niihara et al. (2012) performed shock experiments on Hawaiian basalt doped with baddeleyite and first observed partial melting at 34 GPa. Small vesicles (10–40 μm) were found in the 47 GPa sample, and totally melted matrix with abundant uncoalesced vesicles were observed in the 57 GPa sample. Vesicular multicomponent melts suggest a shock pressure >57 GPa.

Olivine aggregates

In contrast to plagioclase, pyroxene and olivine in experimentally shocked olivine-phyric basalt were not melted even at 48.5 GPa (Takenouchi et al., 2017). In the basalt shocked at 57 GPa by Niihara et al. (2012), the olivine was neither melted nor transformed to high pressure phases. The reactions depend on the duration of the shock and the P-T-t path of the shocked rock (Hu and Sharp, 2022). Reimold and Stöffler (1978) observed vesicles and fine-grained olivine crystallized from sparse intergranular melt, along with solid-state recrystallization in the cores of some olivine grains, in a dunite experimentally shocked at 59 GPa. These textures are somewhat different from the features in NWA 14672, where the olivine has reacted with the large volume of impact melt. This is an alternative maximum pressure estimate to that for the formation of vesiculated melts.

The ubiquity (~14%) of large vesicles in the maskelynite in NWA 14672, and in particular the partial melting and crystallization of olivine in dendritic aggregates, show a shock pressure of at least 59 GPa was experienced, based on the experiments of Reimold and Stöffler (1978) and Niihara (2012). Stöffler et al. (2018) indicate melting and subsequent crystallization of olivine, as observed in NWA 14672, at >60 GPa.

Extensive Melting

Congruent melting is indicated for the plagioclase dendrites associated with plagioclase glass (Fig. 13a) and for the silica particles. The aggregates of olivine, pyroxene, and ilmenite suggest mixing of pools of congruent melt with each other, or limited grain boundary melting. The greater survival of plagioclase melt as coherent entities may be related to differences in viscosity of more and less polymerized liquids. We used Petrolog (Danyuchevsky and Plechov, 2011) with the models of Drake (1976) for plagioclase crystallization and of Bottinga and Weill (1972) to calculate the viscosity of our average plagioclase at its 1 bar liquidus. The liquid plagioclase is about five times more viscous than the barred plagioclase and olivine dendrite melts. This is consistent with limited penetration of maskelynite by multicomponent, usually pyroxene-rich melts (e.g. El Goresy et al., 2013).

The presence of two fine-grained interstitial assemblages is consistent with fairly extensive polyphase melting on a very local scale (~1 mm), following the congruent melting. The barred plagioclase component has normative plagioclase>pyroxene>olivine, consistent with its common occurrence (Fig. S6) between plagioclase and pyroxene (or olivine), and the glass with olivine dendrites has normative pyroxene>>plagioclase. The Petrolog liquidus temperatures of our two fine-grained components are 1280°C (barred plagioclase) and 1114°C (glass with dendrites) at 1 bar. The glass, which crystallized only a few olivine dendrites, was probably superheated. The presence of Fe-Mg-bearing schlieren and blobs in NWA 14672 maskelynite (Fig. 4e,7b) indicates a small amount of eutectic melting or mixing of single-phase melts. There is also mixing of plagioclase bar and olivine dendrite components in the schlieren or blobs (Fig. 2b,7b).

If we eliminate the vesicle content from the modal analysis (Fig. S1e) we see that ‘maskelynite’ and ‘glass’ (olivine-bearing glass and the finest grained part of the barred plagioclase component) alone make up more than 50% of the rock. This is a clear indication that NWA 14672 is more highly shocked than other shergottites.

Shock conditions

The key shock indicators in NWA 14672 are the formation of the two melt rock components, the melting of olivine and plagioclase, and the crystallization of silica polymorphs. The pressure conditions, > 60-65 for large-scale melting (Stöffler et al. (2018), >59 GPa for olivine melting (Reimold and Stöffler, 1978; Niihara et al., 2012), > 45 GPa required for vesiculated maskelynite (Fritz et al., 2005b), and liquid-coesite triple points (Kayama et al., 2018) with stishovite (~13.3GPa) and with quartz (~4.1 GPa), are constraints on the cooling path. All are consistent with temperatures higher than the melting curve of FeS Kavner et al, 2001; Boehler, 1992; Saxena and Erikson, 2015; Manthilake et al., 2019), in agreement with overabundance of sulfides with globular shapes throughout the meteorite, in contrast to polyhedral sulfide textures reported so far for shergottites (Lorand et al., 2005; Baumgartner et al., 2017).

Hu and Sharp (2022) developed a model for the thermal history of shocked basaltic rocks (shergottites compared to MORB liquidus). They emphasize the importance of the quantity of melt produced and the consequent nature of heat transfer between melt and solid rock. Thin veins can be quenched preserving high pressure phases while large volumes of melt decompress at or above liquidus temperatures (Fig. 6 and 7 in Hu and Sharp, 2022). In highly shocked shergottites, thick veins consisting of olivine and pyroxene indicate cooling paths close to the adiabatic release path of melt, rather than quenching at high pressure (Hu and Sharp, 2022). Adapting their model to the potential peak pressures of NWA 14672 >60 GPa, we find that the melt follows the near-adiabatic release curve well above a bulk basalt liquidus (Fig. 14). Based on our interpretation of the textures (coesite crystallized from the silica melt) we would expect the decompression curve to descend into the coesite field between 4 and 15 GPa and pass into the quartz stability field (at <~2000°C, Kayama et al., 2018) before the remaining silica liquid was quenched. If we were to use a 45 or 59 GPa release path this would require a trajectory across the stability fields of stishovite, coesite, and quartz before the formation of silica melt, i.e. the particles would finally have had their interiors melted, inconsistent with the interpretation of the textures.

The abundance of melt components is so high (>50%) that the rock is close to becoming an impact melt rock. We assume this abundance requires a pressure close to the >60-65 GPa limit indicated by Stöffler et al. (2018) for total melting of mafic rocks. We extrapolate an adiabatic decompression curve from a peak pressure of 70 GPa from Hu and Sharp (2022), and find that a melt release curve from ~65 GPa can pass through the liquid silica field and descend through the coesite and then quartz fields (Fig. 14). We therefore conclude that a peak pressure of at least ~65 GPa is appropriate for NWA 14672.

We interpret NWA 14672 'maskelynite' largely as plagioclase crystallized from plagioclase liquid, in part surviving as glass (Fig. 10a) after a strong shock, in agreement with O'Neill et al. (1987) and Walton et al. (2007) for ALH 77005. Similarly, the plagioclase bars were crystallized from a shock melt. The association with vesicles and granular aggregates is characteristic of the most highly shocked shergottites, classified as shock stage S6 by Fritz et al. (2017), as is fusion of adjacent minerals. Stöffler et al. (2018) also include coesite as a signature of S6. Walton and Herd (2007) reported a continuum of melt pockets associated with highly vesiculated plagioclase glass in ALH 77005 and suggested that it is transitional between discrete shock melting (stage S6) and bulk rock melting (stage S7, Stöffler et al., 2018).

During the NWA 14672 impact event we envisage liquid plagioclase, liquid silica, liquid sulfide, and heterogeneous Fe-Mg-bearing melts locally containing remnants or concentrated nuclei of olivine, etc., within a framework of relict igneous material. During decompression and cooling, plagioclase, coesite, quartz, sulfide, and both olivine and plagioclase dendrites and some granular aggregates of olivine, etc., crystallized. We estimate >~50% melt present (based on maskelynite and 'glass'), and part of the olivine and pyroxene was melted, while the vesicle content is ~14%. The pervasive distribution of impact melt in NWA 14672, rather than discrete pockets and veins, indicates conditions even closer to those for impact melt rocks than for ALH 77005. Thus, it is fair to say that the rock reached shock stage S6/7.

Based on radiometric data, only a small number of craters is needed to eject shergottites from the surface of Mars (e.g. Nyquist et al, 2001). All the shergottites show shock effects greater than the minimum pressure required to eject them from the near-surface of Mars. Fritz et al. (2015a) described these shock effects in several shergottite groups separated by ejection ages. A group of basaltic shergottites (Shergotty, Zagami, Los Angeles, and QUE 94201) was ejected at 3 Ma and three poikilitic shergottites (including ALH 77005) were ejected at 4 Ma. In both cases, the less shocked shergottites have shorter terrestrial residence times, and took more time to reach Earth-crossing orbits. Another, larger group of 11 depleted shergottites was ejected at ~1 Ma (Lapen et al., 2017).

Considering whether NWA 14672 belongs to the large group ejected from Mars at ~1 Ma, though its exposure age has not been determined, we can speculate on its possible relationship to other depleted shergottites. Its higher shock stage raises the question of whether this is compatible with derivation from the same crater as the 1 Ma group. Shock dwell times of 10–100 ms are consistent with craters of 14–104 km diameter but depend on impact velocity, and a high degree of melting suggests a long shock pulse and a rather large source crater (Sharp et al. 2019). Lagain et al. (2019) considered 90 million craters, and focused on Tooting crater (D ≈ 30 km), a rayed crater on Mars. Based on crater counting, its ejecta blanket has a formation model age of ~1 Myr, and the surrounding ground has a model age of 308 ± 41 Myr (Lagain et al., 2021). This is the only crater that matches both ejection and crystallization ages of the shergottites (e.g. Udry et al., 2020). The volume of impact melt produced at 30 km diameter lunar craters is approximately 30 km^3 (Silber et al., 2018) and at terrestrial craters approximately 80 km^3 (Pierazzo et al., 1997). We therefore estimate that the quantity of impact melt at the 30 km Tooting crater on Mars is about 1% of the volume excavated (Kizovski et al., 2019). The mass of ejecta that can escape from a planet like Mars is limited to <1% wt% of the projectile mass (Kurosawa et al., 2018). With only a little more than 200 shergottites found, it is not surprising that we have yet to find a totally shock melted shergottite. We conclude that NWA 14672 could have been ejected from Tooting crater like other depleted shergottites.

CONCLUSIONS

Compared to other olivine-phyric shergottites, the highly ferroan, ophitic, vesicular NWA 14672 is unusual mineralogically. It resembles the basaltic shergottites especially NWA 12335, Los Angeles, and NWA 7320, particularly in pyroxene compositions. As it is depleted in K, it could be genetically related to QUE 94201, to which it has almost identical plagioclase compositions but more ferroan pyroxene. The irregular morphology and ferroan overgrowths of olivine phenocrysts suggest scavenging of olivine autocrysts by a basaltic magma.

NWA 14672 contains shock-related features throughout. The plagioclase was melted congruently, vesiculated, and crystallized masses of plagioclase dendrites. Olivine, pyroxene, and ilmenite occur partly as granular aggregates with interstitial plagioclase, indicating growth after congruent melting and limited mixing. There are two coexisting multiphase impact melt components, one with barred plagioclase (mainly plagioclase-derived) and a glass with olivine dendrites (mainly pyroxene-derived), with limited mixing. Shock is indicated by silica particles containing coesite, quartz and silica glass, the vesiculation of plagioclase glass and growth of dendritic/barred plagioclase, the melting of olivine, and the presence of >50% fine-grained melt products. NWA 14672 is the most shocked shergottite so far with shock class S6/S7, and peak pressures >~65GPa. It is likely to belong to the large group of depleted shergottites ejected at ~1 myr from Tooting crater.

Acknowledgments— It is a mixed pleasure to contribute to this volume in memory of Ed Scott, as we remember his enormous contributions to meteorite science and the Meteoritical Society. The first author acknowledges many informative discussions with Ed, and happy moments spent in the company of his family. We are indebted to L. Labenne for the meteorite sample. We thank M. Fialin and N. Rividi for help with the electron probe, David Troadec for the high-quality FIB sections, Ahmed Addad and Maya Marinova for their assistance with the electron microscope instruments, M.J. Carr for IGPET, L. Danyushevsky for PETROLOG, and Axel Wittmann and Ludovic Ferrière for discussions. We are particularly grateful to an (almost) anonymous reviewer for a detailed and patient critique of the manuscript which led to many improvements. This work was partly supported by grant MARS-PRIME ANR-16-CE31-0012 (P.I., N. Mangold), the Programme National de Planétologie (PNP) of CNRS/INSU, co-funded by CNES, as well as ISITE ULNE (Université Lille Nord Europe) and the MEL (Métropole Européenne de Lille), and the Chevreul Institute, the European FEDER and Région Hauts-de-France, and the French RENATECH network.

Data availability Statement—Analytical data and SEM images supporting the results in the paper are available in Supporting Material.

REFERENCES

Balta J. B., Sanborn M., McSween Jr, H. Y., and Wadhwa M. 2013. Magmatic history and parental melt composition of olivine-phyric shergottite LAR 06319: Importance of magmatic degassing and olivine antecrysts in Martian magmatism. *Meteoritics & Planetary Science* 48: 1359-1382.

Barrat J. A., Jambon A., Bohn M., Gillet P., Sautter V., Göpel C., Lesourd M. and Keller F. 2002. Petrology and chemistry of the picritic shergottite North West Africa 1068 (NWA 1068). *Geochimica et Cosmochimica Acta* 66: 3505-3518.

Baumgartner R., Fiorentini M., Lorand J.-P., Baratoux D., Zaccarini F., Ferrière L., Prasek M., and Sener K. 2017. The role of sulfides in the fractionation of highly siderophile and chalcophile elements during the formation of martian shergottite meteorites. *Geochimica et Cosmochimica Acta* 210:1-24.

Bernard S., Beyssac O., and Benzerara K. 2008. Raman mapping using advanced line-scanning systems: geological applications. *Applied Spectroscopy* 62:1180-1188.

Bersani D., Aliatis I., Tribaudino M., Mantovani L., Benisek A., Carpenter M.A., Gatta G.D., and Lottici P.P. 2018. Plagioclase composition by Raman spectroscopy. *Journal of Raman Spectroscopy* 49:684-698.

Boehler R. 1992. Melting of the Fe-FeO and the Fe-FeS systems at high pressure: Constraints on core temperatures *Earth and Planetary Science Letters* 111:217-227.

Boesenberg J. and Hewins R.H. 2010. An experimental investigation into the formation of phosphoran olivine and pyroxene. *Geochimica et Cosmochimica Acta* 74:923-94.

Bogard D. D. and Johnson, P. 1983. Martian gases in an Antarctic meteorite? *Science* 221: 651-654.

Bottinga Y. and Weill D. F. 1972. The viscosity of magmatic silicate liquids; a model calculation. *American Journal of Science* 272: 438-475.

Bouvier A., Blichert-Toft J., and Albarède F. 2009. Martian meteorite chronology and the evolution of the interior of Mars. *Earth and Planetary Science Letters* 280: 285-295.

Campanale F., Mugnaioli E., Gemmi M., and Folco L. 2021. The formation of impact coesite. *Scientific Reports* 111:1-8.

Cavosie A. J., and Koeberl C. 2019. Overestimation of threat from 100 Mt–class airbursts? High-pressure evidence from zircon in Libyan Desert Glass. *Geology* 47: 609-612.

Cavosie A.J., Spencer C., Evans N., Rankenburg K., Thomas R.J., and Macey P.H. 2022 Granular titanite from the roter kamm crater in Namibia: Product of regional metamorphism, not meteorite impact. *Geoscience Frontiers* doi: https://doi.org/10.1016/j.gsf.2022.101350

Chen M. and El Goresy A. 2000. The nature of maskelynite in shocked meteorites: not diaplectic glass but a glass quenched from shock-induced dense melt at high pressures. *Earth and Planetary Science Letters* 179:489-502.

Danyushevsky L. V. and Plechov P. 2011. Petrolog 3: Integrated software for modeling crystallization processes. *Geochemistry, Geophysics, Geosystems* 12:Q07021

Darling J. R., Moser D. E., Barker I. R., Tait K. T., Chamberlain K. R., Schmitt A. K., and Hyde B. C. 2016. Variable microstructural response of baddeleyite to shock metamorphism in young basaltic shergottite NWA 5298 and improved U–Pb dating of Solar System events. *Earth and Planetary Science Letters* 444:1-12.

Day, J., Tait, K. T., Udry, A., Moynier, F., Liu, Y., and Neal, C. R. 2018. Martian magmatism from plume metasomatized mantle. *Nature Communications*, 9:1-8.

Donaldson C.H. 1976. An experimental investigation of olivine morphology. *Contributions to Mineralogy and Petrology* 57:187–213.

Drake M.J. 1976. Plagioclase-melt equilibria. *Geochimica et Cosmochimica Acta* 40:457-465.

El Goresy A., Gillet P., Miyahara M., Ohtani E., Ozawa S., Beck P., and Montagnac G. 2013. Shock-induced deformation of shergottites: shock-pressures and perturbations of magmatic ages on Mars. *Geochimica et Cosmochimica Acta* 101:233-262.

Erickson T. M. 2018. Shocked monazite: an impact barometer and geochronometer. In *Large Meteorite Impacts and Planetary Evolution VI*, Abstract #5109. LPI Contribution No. 2136, Lunar and Planetary Institute, Houston.

Fau A., Beyssac O., Gauthier M., Cousin A., Meslin P.Y., Benzerara K., Bernard S., Boulliard J.C., Gasnault O., Forni O., Wiens R.C., Morand M., Rosier P., Garino Y., Pont S. and Maurice S. 2019. Pulsed laser-induced heating of mineral phases: implications for laser-induced breakdown spectroscopy combined with Raman spectroscopy**.** *Spectrochimica Acta Part B: Atomic Spectroscopy* 160, doi: 10.1016/j.sab.2019.105687

Faure F., Trolliard G., Nicollet C., and Montel J.-M. 2003. A developmental model of olivine morphology as a function of the cooling rate and the degree of undercooling. *Contributions to Mineralogy and Petrology* 145:251-263.

Fazio G., Augello M., and Montalbano S. 2017. Coesite in suevite from the Ries impact structure (Germany): From formation to postshock evolution. *Meteoritics & Planetary Science*, *52*:1437-1448.

Fei Y. and Bertka C.M. 1999 Phase transitions in the Earth's mantle and mantle mineralogy. In: *Mantle petrology: field observations and high pressure experimentation*, edited by Fei Y., Bertka C.M., and Mysen B.O. Geochemical Society, New York, pp 189–207.

Filiberto J. and Dasgupta R. 2011. Fe^{2+}-Mg partitioning between olivine and basaltic melts: Applications to genesis of olivine-phyric shergottites and conditions of melting in the Martian interior. *Earth and Planetary Science Letters* 304:527–537.

Filiberto J., Gross J., Trela J., and Ferré E. C. 2014. Gabbroic shergottite Northwest Africa 6963: an intrusive sample of Mars. *American Mineralogist* 99:601-606.

First E. and Hammer J. 2016. Igneous cooling history of olivine-phyric shergottite Yamato 980459 constrained by dynamic crystallization experiments. *Meteoritics & Planetary Science* 51: 1233-1255.

Folco L., Mugnaioli E., Gemelli M., Masotta M., and Campanale F. 2018. Direct quartz-coesite transformation in shocked porous sandstone from Kamil Crater (Egypt). *Geology* 46:739-742.

Freeman J. J., Wang A., Kuebler K. E., Jolliff B. L., and Haskin L. A. 2008. Characterization of natural feldspars by Raman spectroscopy for future planetary exploration. *The Canadian Mineralogist* 46:1477-1500.

French B. M. and Koeberl C. 2010. The convincing identification of terrestrial meteorite impact structures: What works, what doesn't, and why. *Earth-Science Reviews*, *98*:123-170.

Fritz, J., Artemieva, N., & Greshake, A. (2005a) Ejection of Martian meteorites. *Meteoritics & Planetary Science*, *40*(9-10), 1393-1411.

Fritz J., Greshake A., and Stöffler D. 2005b. Micro-Raman spectroscopy of plagioclase and maskelynite in Martian meteorites: Evidence of progressive shock metamorphism. *Antarctic Meteorite Research*, 18:96-116.

Fritz J., Greshake A., and Fernandes V. A. 2017. Revising the shock classification of meteorites. *Meteoritics & Planetary Science* 52:1216-1232.

Fritz J., Assis Fernandes V., Greshake A., Holzwarth A., and Böttger, U. (2019). On the formation of diaplectic glass: Shock and thermal experiments with plagioclase of different chemical compositions. *Meteoritics & Planetary Science 54*: 1533-1547.

Frost B.R. and Lindsley D.H. 1991 Occurrence of iron titanium oxides in igneous rocks, In *Oxide Minerals: Petrologic and Magnetic Significance*; edited by D. H. Lindsley. Reviews in Mineralogy 25: 433-468.

Gillet P., Le Cléac'h A., and Madon M. 1990. High-temperature Raman spectroscopy of SiO_2 and GeO_2 polymorphs: Anharmonicity and thermodynamic properties at high-temperatures. *Journal of Geophysical Research: Solid Earth* 95:21635-21655.

Gnos E., Hofmann B., Franchi I. A., Al-Kathiri A., Huser M., and Moser L. 2002. Sayh al Uhaymir 094: A new martian meteorite from the Oman desert. *Meteoritics & Planetary Science* 37: 835-854.

Goodrich C. A. 2002. Olivine-phyric martian basalts: A new type of shergottite. *Meteoritics and Planetary Science* **37:**B31–B34.

Greenwood J.P. and Hess P.C. 1996. Congruent melting kinetics: constraints on chondrule formation. In *Chondrules and the Protoplanetary Disk*. Edited by Hewins R.H., Jones R.H., and Scott E.R.D. Cambridge:CambridgeUniv.Press. pp.205–211.

Greshake A. and Stöffler D. 2000. Shock-related melting phenomena in the SNC meteorite Dar al Gani 476 (abstract# 1043). 31st Lunar and Planetary Science Conference. CD-ROM.

Greshake A., Fritz J., and Stöffler D. 2004. Petrology and shock metamorphism of the olivine-phyric Shergottite Yamato 980459: Evidence for a two-stage cooling and single-stage ejection history. *Geochimica et Cosmochimica Acta* 68:2359-2377.

Gross J., Treiman A. H., Filiberto J., and Herd C. D. 2010. Primitive olivine-phyric shergottite NWA 5789: Petrography, mineral chemistry, and cooling history imply a magma similar to Yamato-980459. *Meteoritics & Planetary Science* 46:116-133.

Gross J., Filiberto J., Herd C. D., Daswani M. M., Schwenzer S. P., and Treiman A. H. 2013. Petrography, mineral chemistry, and crystallization history of olivine-phyric shergottite NWA 6234: A new melt composition. *Meteoritics & Planetary Science* 48: 854-871.

Grove T. L. 1982. Use of exsolution lamellae in lunar clinopyroxenes as cooling rate speedometers: an experimental calibration. *American Mineralogist* 67:251-268.

He Q., Xiao L., Balta J. B., Baziotis I. P., Hsu W., and Guan Y. 2015. Petrography and geochemistry of the enriched basaltic shergottite Northwest Africa 2975. *Meteoritics & Planetary Science* 50: 2024-2044.

Herd C. D., Walton E. L., Agee C. B., Muttik N., Ziegler K., Shearer C. K., ... and Caffee, M. W. 2017. The Northwest Africa 8159 martian meteorite: Expanding the martian sample suite to the early Amazonian. *Geochimica et Cosmochimica Acta* 218:1-26.

Hewins R.H., Humayun M., Barrat J.-A., Zanda B., Lorand J.-P., Pont S., Assayag N., Cartigny P., Yang S., and Sautter V. 2020. Northwest Africa 8694, a ferroan chassignite: bridging the gap between nakhlites and chassignites. *Geochimica et Cosmochimica Acta* 282:201-226.

Hu J., and Sharp T. G. 2022. Formation, preservation and extinction of high-pressure minerals in meteorites: temperature effects in shock metamorphism and shock classification. *Progress in Earth and Planetary Science* 9:1-22.

Hu S., Li Y., Gu L., Tang X., Zhang T., Yamaguchi A., Yangting L., and Changela H. 2020. Discovery of coesite from the martian shergottite Northwest Africa 8657. *Geochimica et Cosmochimica Acta* 286:404-417.

Hui H., Peslier A., Lapan T., Schafer J., Brandon A,. and Irving A. J. 2011. Petrogenesis of basaltic Shergottite Northwest Africa 5298: Closed system crystallization of an oxidized mafic melt. *Meteoritics & Planetary Science* 46:1313-1328.

Humayun M., Nemchin A., Zanda B., Hewins R. H., Grange M., Kennedy A., Lorand J.-P., Göpel C., Fieni C., Pont S., and Deldicque D. 2013. Origin and age of the earliest Martian crust from meteorite NWA7533. *Nature* 503:513–517.

Ikeda Y., Kimura M., Takeda H., Shimoda G., Kita N.T., Morishita, Y., Suzuki, A., Jagoutz E., and Dreibus, G. 2006. Petrology of a new basaltic shergottite: Dhofar 378, *Antarctic Meteorite Research* 19: 20–44

Irving A. J., Bunch T. E., Kuehner S. M., Herd C. D. K., Gellissen M., Lapen T. J., Rumble D. III, and Pitt D. 2011. Petrologic, elemental and isotopic characterization of shock-melted, enriched ultramafic poikilitic shergottite Northwest Africa 6342 (abstract #1608). 42nd Lunar and Planetary Science Conference. CD-ROM.

Irving A. J., Kuehner S. M., Ziegler K., Chen G., Herd C. D. K., ... and Hmani A. 2013. Northwest Africa 7635: The first depleted, highly ferroan and phosphate-free evolved olivine-plagioclase-phyric shergottite. *Meteoritics & Planetary Science* 47 (Suppl.): *Meteoritics & Planetary Science* 47 (Suppl.):5274.pdf.

Jensen L.S. and Pyke D.R. 1982. Komatiites in the Ontario portion of the Abitibi Belt. In *Komatiites,* edited by N. T. Arndt, and E. G. Nisbet. London, Boston, and Sydney : George Allen and Unwin). pp. 147-157.

Kanemaru R., Imae N., Yamaguchi A., Takenouchi A., and Nishido H. 2020. Estimation of shock degrees of eucrites using X-ray diffraction and petrographic methods. *Polar Science 26*: 100605.

Kavner A., Duffy T.S., and Shen G. 2001. Phase stability and density of FeS at high pressures and temperatures: implications for the interior structure of Mars. *Earth and Planetary Science Letters* 185:25-33.

Kayama, M., Nagaoka H., and Niihara T. 2018. Lunar and martian silica. *Minerals* 8: 267.

Keller L. P., Treiman A. H., and Wentworth S. J. 1992. Shock effects in the shergottite LEW 88516: optical and electron microscope observations. *Meteoritics*:27.

Kenney G. G., Karlsson A., Schmieder M., Whitehouse M. J., Nemchin A. A., and Bellucci J. J. 2019. A review of shock-metamorphic features in apatite from terrestrial impact structures and possible implications for extra-terrestrial phosphates (Abstract #1357). 50th Lunar and Planetary Science Conference CD-ROM.

Kieffer S. W. 1971. Shock metamorphism of the Coconino sandstone at Meteor Crater, Arizona. *Journal of Geophysical Research* 76: 5449-5473.

Kizovski T. V., Tait K. T., Di Cecco V. E., White L. F., and Moser D. E. 2019. Detailed mineralogy and petrology of highly shocked poikilitic shergottite Northwest Africa 6342. *Meteoritics & Planetary Science* 54:768-784.

Kring D. A., Gleason J. D., SwindleT. D., Nishiizumi, K., Caffee M. W., Hill D. H., Jull A. J. and Boynton W. V. 2003. Composition of the first bulk melt sample from a volcanic region of Mars: Queen Alexandra Range 94201. *Meteoritics & Planetary Science* 38:1833-1848.

Kurosawa K., Okamoto T., and Genda H. 2018. Hydrocode modeling of the spallation process during hypervelocity impacts: Implications for the ejection of Martian meteorites. *Icarus* 301:219-234.

Lagain A., Benedix G.K., Servis K., Baratoux D., Doucet L.S., Rajšic A., Devillepoix H.A.R., Bland P.A., Towner M.C., Sansom E.K. and Miljković K. 2021. The Tharsis mantle source of depleted shergottites revealed by 90 million impact craters. *Nature Communications* 12:1-9.

Lagain A., Bouley S., Zanda B., Miljković K., Rajšić A., Baratoux D., Payré V., Doucet L.S., Timms N.E., Hewins R., and Benedix, G.K., Malarewic V., Servis K. and Bland P. A. 2022. Early crustal processes revealed by the ejection site of the oldest martian meteorite. *Nature Communications* 13

3782. https://doi.org/10.1038/s41467-022-31444-8.

Lapen T.J., Righter M., Andreasen R., Irving A.J., Satkoski A.M., Beard B.L., Nishiizumi K., Jull A.T., and Caffee M.W. 2017. Two billion years of magmatism recorded from a single Mars meteorite ejection site. *Science Advances* 3(2) e1600922 2017.

Le Maitre R., Bateman P., Dudek A., Keller J., Lameyre J., Le Bas M., Sabine P., Schmid R., Sorensen H., Streckeisen A., Woolley A., and Zanettin, B. 1989. A classification of igneous rocks and glossary of terms: Recommendations of the International Union of Geological Sciences Subcommission on the Systematics of igneous rocks (edited by Le Maitre, R.W.;). Oxford: Blackwell. 193 p.

Liu Y., Tice M. M., Schmidt M. E., Treiman A. H., Kizovski T. V., Hurowitz J. A. ... and Zorzano M. P. 2022. An olivine cumulate outcrop on the floor of Jezero crater, Mars. *Science* 377:1513–1519.

Lorand J.-P., Chevrier V., and Sautter V. 2005. Sulfide mineralogy and redox conditions in some Shergottites. *Meteoritics & Planetary Science* 40:1257-1272.

Lorand J. P., Barrat, J. A., Chevrier V., Sautter V., and Pont S. 2012. Metal-saturated sulfide assemblages in NWA 2737: Evidence for impact-related sulfur devolatilization in Martian meteorites. *Meteoritics & Planetary Science* 47: 1830-1841.

Makoto K., Hiroshi T., Gen S., Kita N., Yuichi M., Akio S., Jagoutz E., and Dreibus G. 2006. Petrology of a new basaltic shergottite: Dhofar 378. *Antarctic Meteorite Research* 19:20-44.

Manthilake G., Chantel J. Monteux J., Andrault D., Bouhifd M.A. et al. 2019. Thermal conductivity of FeS and its implications for Mercury's long sustaining magnetic field. *Journal of Geophysical Research. Planets*124:2359-2368.

McCubbin, F. M., Phillips, B. L., Adcock, C. T., Tait, K. T., Steele, A., Vaughn, J. S., ... and Hausrath, E. M. 2018. Discreditation of bobdownsite and the establishment of criteria for the identification of minerals with essential monofluorophosphate (PO3F2^{-}). *American Mineralogist* 103:1319-1328.

McGregor M., McFarlane C. R., and Spray J. G. 2018. In situ LA-ICP-MS apatite and zircon U–Pb geochronology of the Nicholson Lake impact structure, Canada: shock and related thermal effects. *Earth and Planetary Science Letters* 504:185-197.

McGregor M., McFarlane C. R., and Spray J. G. 2019. In situ multiphase U–Pb geochronology and shock analysis of apatite, titanite and zircon from the Lac La Moinerie impact structure, Canada. *Contributions to Mineralogy and Petrology* 174:1-20.

McGregor M., Walton E. L., McFarlane C. R., and Spray J. G. 2020. Multiphase U-Pb geochronology of sintered breccias from the Steen River impact structure, Canada: Mixed target considerations for a Jurassic-Cretaceous boundary event. *Geochimica et Cosmochimica Acta* 274:136-156.

Mernagh T. P. 1991. Use of the laser Raman microprobe for discrimination amongst feldspar minerals. *Journal of Raman Spectroscopy* 22:453-457.

Meyer C., Fritz J., Misgaiski M., Stöffler D., Artemieva N. A., Hornemann U. ... and Rabbow E. 2011. Shock experiments in support of the Lithopanspermia theory: The influence of host rock composition, temperature, and shock pressure on the survival rate of endolithic and epilithic microorganisms. *Meteoritics & Planetary Science* 46:701-718.

Mikouchi T., Miyamoto M., and McKay G. A. 1998. Mineralogy of Antarctic basaltic shergottite Queen Alexandra Range 94201: similarities to Elephant Moraine A79001 (lithology B) martian meteorite. *Meteoritics & Planetary Science* 33:181-189.

Mikouchi T., Miyamoto M., and McKay G. A. 1999. The role of undercooling in producing igneous zoning trends in pyroxenes and maskelynites among basaltic Martian meteorites. *Earth and Planetary Science Letters* 173:235–256.

Mikouchi T., and McKay G. 2003. Shock heating and subsequent cooling of basaltic shergottites: the cases for QUE94201 and Dhofar 378. (abstract #1920). 34th Lunar and Planetary Science Conference. CD-ROM.

Mikouchi T., Koizumi E., McKay G., Monkawa A., Ueda Y., Chokai J., and Miyamoto M. 2004. Yamato 980459: Mineralogy and petrology of a new shergottite-related rock from Antarctica. *Antarctic Meteorite Research* 17:13.

Moser D. E., Chamberlain K. R., Tait K. T., Schmitt A. K., Darling J. R., Barker I. R., and Hyde B. C. 2013. Solving the Martian meteorite age conundrum using micro-baddeleyite and launch-generated zircon. *Nature* 499:454-457.

Nicklas R. W., Day J. M., Vaci Z., and Udry A. 2022. Petrogenesis of Northwest Africa 8686: A ferroan olivine-phyric shergottite. *Meteoritics & Planetary Science* 57 1–18. doi: 10.1111/maps.1380

Niihara T., Kaiden H., Misawa K., Sekine T., and Mikouchi T. 2012. U–Pb isotopic systematics of shock-loaded and annealed baddeleyite: implications for crystallization ages of Martian meteorite shergottites. *Earth and Planetary Science Letters* 341:195-210.

Nyquist L. E., Bogard D. D., Shih C. Y., Greshake A., Stöffler D., and Eugster O. 2001. Ages and geologic histories of Martian meteorites. In *Chronology and Evolution of Mars: Proceedings of an ISSI Workshop, 10–14 April 2000, Bern, Switzerland* (pp. 105-164). Springer Netherlands.

O'Neill C., Ikeda Y., and Delaney J. S. 1987. The compositional zoning of feldspathic phases in Allan Hills 77005,32 (abstract). Lunar and Planetary Science Conference XVIII, 750-751.

Orr K. J., Forman L. V., Rankenburg K., Evans N. J., McDonald B. J., Godel B., and Benedix G. K. 2022. Geochemical and mineralogical classification of four new shergottites: NWA 10441, NWA 10818, NWA 11043, and NWA 12335. *Meteoritics & Planetary Science* 57:1194-1223.

Ostertag R. 1983. Shock experiments on feldspar crystals. *Journal of Geophysical Research: Solid Earth* 88:B364-B376.

Pang R. L., Zhang A. C., Wang S. Z., Wang R. C., and Yurimoto, H. 2016. High-pressure minerals in eucrite suggest a small source crater on Vesta. *Scientific Reports* 6:26063.

Papike J. J., Karner J. M., Shearer C. K., and Burger P. V. 2009. Silicate mineralogy of martian meteorites. *Geochimica et Cosmochimica Acta* 73:7443-7485.

Papike J. J., Hodges F. N., Bence A. E., Cameron M., and Rhodes J. M. 1976. Mare basalts: Crystal chemistry, mineralogy, and petrology. *Reviews of Geophysics* 14:475-540.

Papike J. J., Karner J. M., Shearer C. K., and Burger P. V. 2009. Silicate mineralogy of martian meteorites. *Geochimica et Cosmochimica Acta* 73:7443-7485.

Pepin R. O. 1985. Meteorites: evidence of Martian origins. *Nature* 317:473-475.

Peslier A. H., Hnatyshin D., Herd C. D. K., Walton E. L., Brandon A. D., Lapen T. J., and Shafer J. T. 2010. Crystallization, melt inclusion, and redox history of a Martian meteorite: Olivine-phyric shergottite Larkman Nunatak 06319. *Geochimica et Cosmochimica Acta* 74:4543-4576.

Pierazzo E., Vickery A. M., and Melosh H. J. 1997. A reevaluation of impact melt production. *Icarus* 127: 408-423.

Rauch E. F. and Véron M. 2014. Automated crystal Orientation and Phase Mapping in TEM. *Materials Characterization* 98:1–9. doi:10.1016/j.matchar.2014. 08.010

Reid A. M. and Bunch T. E. 1975. The nakhlites, part II: Where, when, and how. *Meteoritics* 10:317–324:

Reimold W. U. and Stöffler D. 1978. Experimental shock metamorphism of dunite (abstract). Lunar and Planetary Science Conference Proceedings IX:2805-2824.

Rubin A. E., Warren P. H., Greenwood J. P., Verish R. S., Leshin L.A., Hervig R. L., Clayton R. N., and Mayeda T. K. 2000 Petrology of Los Angeles: A new basaltic shergottite find. *Geology* 28:1011–1014.

Saxena S. and Eriksson E. 2015. Thermodynamics of Fe–S at ultra-high pressure. *Calphad* 51:202–205.

Sharp T. G., Walton E. L., Hu J., and Agee C. 2019. Shock conditions recorded in NWA 8159 martian augite basalt with implications for the impact cratering history on Mars. *Geochimica et Cosmochimica Acta* 246:197-212.

Shearer C. K., Burger P. V., Papike J. J., Borg L. E., Irving A. J. and Herd C. 2008. Petrogenetic linkages among martian basalts. Implications based on trace element chemistry of olivine. *Meteoritics & Planetary Science* 43, 1241–1258.

Shearer C. K., Burger P. V., Papike J. J., McCubbin F. M., and Bell A. S. 2015. Crystal chemistry of merrillite from Martian meteorites: Mineralogical recorders of magmatic processes and planetary differentiation. *Meteoritics & Planetary Science* 50: 649-673.

Silber E. A., Zanetti M., Osinski G. R., Johnson B. C., and Grieve R. A. F. 2018. A combined modeling and observational study of the effect of impact velocity on production of melt in simple-to-complex lunar craters (abstract #2083). 49th Annual Lunar and Planetary Science Conference. CD-ROM.

Stöffler D. 1971. Coesite and stishovite: Identification and formation conditions in shock-metamorphosed rocks. *Journal of Geophysical Research* 76:5474-5488.

Stöffler D. and Langenhorst F. 1994. Shock metamorphism of quartz in nature and experiment: I. Basic observation and theory. *Meteoritics* 29:155–181.

Stöffler D., Ostertag R., Jammes C., Pfannschmidt G., Sen Gupta P.R., Simon S. B., Papike J. J., and Beauchamp R. H. 1986. Shock metamorphism and petrography of the Shergotty achondrite. *Geochimica et Cosmochimica Acta* 50:889-903.

Stöffler D., Hamann C., and Metzler K. 2018. Shock metamorphism of planetary silicate rocks and sediments: Proposal for an updated classification system. *Meteoritics & Planetary Science* 53:5-49.

Stolper E. M. and McSween H. Y. 1979. Petrology and origin of shergottite meteorites. *Geochimica et Cosmochimica Acta* 43:1475–1498.

Takenouchi A., Mikouchi T., Kobayashi T., and Yamaguchi A. 2017. Shock recovery experiment of olivine-phyric basalt for constraining formation conditions of brown olivine in martian meteorites (abstract #1897). 48th Annual Lunar and Planetary Science Conference. CD-ROM.

Treiman A. H., McKay G. A. , Bogard D. D., Mittlefehld D. W., Wang M-S. , Keller L., Lipschutz M. E., Lindstrom M. M. and Garrison. D. 1994. Comparison of the LEW88516 and ALHA77005 martian meteorites: Similar but distinct. *Meteoritics* 29:581-592.

Udry A. and Day J.M. 2018. 1.34 billion-year-old magmatism on Mars evaluated from the co-genetic nakhlite and chassignite meteorites. *Geochimica et Cosmochimica Acta* 238:292-315.

Udry A., Howarth, G.H., Lapen, T.J. and Righter, M. 2017. Petrogenesis of the NWA 7320 enriched martian gabbroic shergottite: Insight into the martian crust. *Geochimica et Cosmochimica Acta* 204:1-18.

Udry A., Howarth G. H., Herd C. D. K., Day J. M., Lapen T. J., & Filiberto J. 2020. What martian meteorites reveal about the interior and surface of Mars. *Journal of Geophysical Research: Planets*. e2020JE006523.

Usui T., McSween Jr H. Y., and Floss C. 2008. Petrogenesis of olivine-phyric shergottite Yamato 980459, revisited. *Geochimica et Cosmochimica Acta* 72:1711-1730.

Walton E. L. and Herd C. D. K. 2007. Localized shock melting in lherzolitic shergottite Northwest Africa 1950: Comparison with Allan Hills 77005. *Meteoritics and Planetary Science* 42:63-80.

Walton E. L., Jugo P. J., Herd C. D. K., and Wilke M. 2010. Martian regolith in Elephant Moraine 79001 shock melts? Evidence from major element composition and sulfur speciation. *Geochimica et Cosmochimica Acta* 74:4829-4843.

Walton E. L., Irving A. J., Bunch T. E., and Herd C. D. K. 2012. Northwest Africa 4797: a strongly shocked ultramafic poikilitic shergottite related to intermediate Martian meteorites. Meteoritics & Planetary *Science* 47:1449–1474.

Walton E. L., Sharp T. G., Hu J. and Filiberto J. 2014. Heterogeneous mineral assemblages in Martian meteorite Tissint as a result of a recent small impact event on Mars. *Geochimica et Cosmochimica Acta* 140:334-348.

Wang D., and Chen M. 2006. Shock-induced melting, recrystallization, and exsolution in plagioclase from the Martian lherzolitic shergottite GRV 99027. *Meteoritics and Planetary Science*, 41:519-527.

Wang H. and Salveson I. 2005. A review on the mineral chemistry of the nonstoichiometric iron sulphide, $Fe_{1-x}S$ ($0 \leq x \leq 0.125$): polymorphs, phase relations and transitions, electronic and magnetic structures. *Phase Transitions* 78:547-567.

Warren P. H., Greenwood J. P., and Rubin A. E. 2004). Los Angeles: A tale of two stones. *Meteoritics & Planetary Science* 39:137-156.

Wiens R. C., Udry A., Beyssac O., Quantin-Nataf C., Mangold N., Cousin A. ... and SuperCam Team. 2022. Compositionally and density stratified igneous terrain in Jezero crater, Mars. *Science Advances* 8: eabo3399.

Zanetta P.-M., Le Guillou C., Leroux H., Zanda B., Hewins R. H., Lewin E., and Pont S. 2019. Modal abundance, density and chemistry of micrometer-sized assemblages by advanced electron microscopy: Application to chondrites. *Chemical Geology* 514:27–41.

FIGURE CAPTIONS

Fig. 1. (a) BSE map of NWA 14672. Olivine off-white; pyroxene light grey; feldspar dark grey; vesicles black. (b) Phase map. Olivine red-orange; pyroxene light blue. Feldspar (dark blue with vesicles black) and fine-grained components (“glass”, purple) are seen throughout.

Fig. 2. BSE images. (a) Coarse-grained: vesicules (V) in plagioclase (PL), ophitic pyroxene (PX) and irregular olivine (OL). (b) Fine-grained: areas of glass with ferroan olivine dendrites (gd) and areas with feldspar bars (bp); also maskelynite/plagioclase (PL) patches, pyroxene and olivine.

Fig. 3 Raman spectra of selected phases.

Fig. 4. BSE images showing olivine and pyroxene zonation and relationships. Olivine (OC cores, medium grey and OR rims, white), both anhedral (a) and euhedral (c) is partly enclosed by pyroxene (patchy, dark grey - medium grey). (b,d) Patchy pyroxene with irregular “cores” embedded in ferroan pigeonite, and granular olivine. (e) Plagioclase (M), vesicles, anhedral olivine (OL), patchy pyroxene(PX), invaded by barred olivine and glass containing olivine dendrites. (f) Irregular distribution of small anhedral olivine grains.

Fig. 5. BSE images of Fe sulfides (A) A rare sulfide grain (S) with scalloped indentations like those in most shergottites and micron-size sulfide (S) in barred plagioclase (Pl), with interstitial P-rich olivine (Ol), pyroxene and vesicles (V)). (B) A sulfide spherule attached to a

vesicle (V), in glass with olivine dendrites (Ol) and plagioclase bars) with inclusions of glass (G) and ulvöspinel (Usp inside the sulfide).

Fig. 6. Compositions of olivine, pyroxene, feldspar, and spinel in NWA 14672. Olivine dendrites include fine olivine associated with barred feldspar.

Fig. 7. Barred plagioclase (bp) occurring (a) mainly between 'maskelynite' (PL) and pyroxene (PX and sometimes olivine, OL); (b) also as globules containing pyroxene or glass with olivine dendrites (gd) within 'maskelynite'; Il ilmenite, V vesicles; (c) between maskelynite (M) and glass with olivine dendrites (G+O), or pyroxene (PX) and olivine (OL); and (d) within plagioclase enclosed ophitically in pyroxene.

Fig. 8. Crystal morphology in a barred feldspar area. (a) Barred feldspar area surrounded by glass with olivine dendrites, showing locations of details b-g. (b) Aggregate of pyroxene granules overgrown by pyroxene blades interstitial to feldspar bars. (c) Large olivine dendrite associated with olivine interstitial to feldspar bars. (d) aggregate of ilmenite granules within a barred feldspar area. (e) Olivine dendrites overgrowing a mass of porous olivine and protruding into barred feldspar. (f) Detail of pyroxene below ilmenite in (d) showing it is surrounded by feldspar and partly by darker pyroxene.

Fig. 9. BSE images (a,c,e,g,i) with olivine (off-white), vesicles and plagioclase bars (black), with basaltic glass, pyroxene, and melilite (all grey), and also ulvöspinel and pyrrhotite, plus the corresponding Kα X-ray images: (b) Enlargement of rectangle in 'a'. Olivine dendrites (green) in glass (blue; pyrrhotite (yellow) surrounded by ulvöspinel (red). (d) Barred plagioclase green, olivine dendrites red, pyroxene orange, glass (bottom) and merrillite (top) dark blue, Fe sulfide light blue, Fe-Ti oxide pink. (f) Olivine (red) as large grains with unresolved overgrowths. Merrillite (light blue) resembles fragments. Plagioclase yellow. (h) Silica green, feldspar yellow, merrillite blue, olivine orange. (j) Feldspar blue, olivine yellow-green, pyroxene green, merrillite black between plagioclase bars.

Fig. 10. The major element compositions of the fine-grained components, barred plagioclase and glass with olivine dendrites, reflect melting of plagioclase and a ~50-50 pyroxene-olivine mixture. Deviations from simple mixing indicate the participation of merrillite, ilmenite and Fe_sulfide.

Fig 11. Pyroxene aggregate. (a.) HAADF image. (b) Tweed texture in pyroxene. (c) EDXS map shows strong chemical variation in pyroxene grains, an Fe-Ti-oxide dendrite (in red), plagioclase (dark blue), and the Ca-phosphate (in bright blue, middle top and close to the bottom left corner). (d) Automated crystal orientation mapping shows random orientation, i.e. crystallization from liquid, not neoblasts. (e) "Point" EDXS analyses were made of selected areas (ROI) 200x200 nm square, that show similar to compositions those of large crystals.

Fig.12. Heterogeneity of patchy pyroxene X-ray map (enhanced, Ca pink-white, Mg blue); glass with olivine and barred plagioclase are hard to distinguish from maskelynite (pinkish).

Fig. 13. (a) An aggregate of plagioclase dendrites (dPL) set in plagioclase glass (gPL). (b) Coesite (C) and quartz (Q) grown on the margins of a silica glass (gSi) particle in barred plagioclase (bPL).

Fig. 14. Schematic diagram for the decompression path of NWA 14672 for a peak pressure >65 GPa with release curve for the melt fraction extrapolated from Hu and Sharp (2022). This path passes through the stability fields of liquid silica, coesite, and then quartz (Kayama et al., 2018).

SUPPORTING INFORMATION

File Supporting Tables S1-7. Tables of analytical data.xlsx

Docx with all supporting figures. All Supp Figs.docx

Fig. S1. A large subhedral phenocryst with irregular rim extensions, and fine-grained enclaves or embayments containing vesicles.

Fig. S2. Variation in Fe X-ray intensity superimposed on BSE map (grey scale) of NWA 14672. (a) olivine: cores (yellow-green) are often inside pyroxene (grey); rims (red) are often in plagioclase (black). (b) pyroxene: rims red, cores blue (Ca-rich) or yellow-green. Variation in Fe intensity in olivine and pyroxene is represented by a 256-level jet colorbar. The minimum and maximum Fe intensities are normalized to 0 and 256 respectively.

Fig. S3. Nucleation of Ti-rich dendrites on Fe sulfide grains in the glass with olivine dendrites of Fig. 9a. (a) BSE - Glass with rectangle showing the location of (b) X-ray map: green olivine, yellow Fe sulfide, red Ti-rich phase, speckled red and blue glass. (c,d) BSE – note submicron ulvöspinel dendrites nucleated on sulfide globules.

Fig. S4. Olivine occurring between plagioclase bars is phosphoran (1.8-2.3 wt. % P_2O_5).

Fig. S 5. Individual X-ray spectra for Fig. 9c,d. Feldspar (high Al), pyroxene (Mg>Fe), olivine (Fe=Mg), glass (low P, low Ti), merrillite (P), Fe-rich (S and Ti).

Fig. S6. X-ray images accompanying Fig. 9. e,f. Feldspar (high Al), silica (high Si), olivine (high Fe), merrillite (P), ilmenite (high Ti), and sulfide (high S).

Fig. S7. Individual X-ray images for Fig. 9. g,h. Feldspar (high Al), olivine (Fe>Mg), glass (low P, low Ti), merrillite (high P), Fe-rich (S and Ti).

Fig. S8. Individual X-ray images for Fig. 9. i,j. Feldspar (high Al), olivine (Fe>Mg), glass (low P, low Ti), merrillite (high P), Fe-rich (S and Ti).

Fig. S9. Fine-grained regions have bulk compositions similar to those of picritic or tholeiitic basalts, in some respects (Le Maitre et al., 1989; Jensen and Pike, 1982).

Fig. S10. This fibrous-looking pyroxene composed of chains of granules is seen to the bottom right of the barred plagioclase seen in Fig. S9i,j, as identified in X-ray maps in Fig. S8.

Fig. S11. Ilmenite aggregate (a) with interstitial pyroxene, maskelynite, and an Si-rich phase (b). Ilmenite also contains 10-40 nm droplet-like feldspathic inclusions (c) and magnetite (d).

Fig. S12. Traverse across patchy pyroxene mixed with merrillite, glass and olivine. EMP analyses shown as wt. % oxide and as atomic proportion

Fig. S13. Patchy pyroxene: X-ray, BSE, and composite Ca-Mg map, and individual maps for Ca, Fe, and Mg, the latter three marked with mol % Wo, Fs, and En, respectively.

Fig. S14. Normal pyroxene (top) has a lower Ti/Al ratio than the later crystallized ferroan patchy pyroxene rims.

Fig. S15. Plagioclase glass (center and right, light grey in BSE, red in false color Raman signal) separating poorly crystalline plagioclase masses (dark grey in BSE, green in Raman signal). The lower mass (b) is dendritic (poorly crystalline) and differs spectrally from (a), though both have a single peak at ~500 cm^{-1}, replacing the plagioclase doublet.

Fig. S16. An Si Kα X-ray map shows the presence of 0.5% SiO_2 particles (bright blue specks).

Fig. S17. (a) Veined silica particle associate with pyroxene aggregates and glass with pyroxene dendrites. (b) Heavily veined silica particle with 'fizz' containing nanopores and Fe-rich particles (sulfide?). (c) Annotation of phases (Co coesite, Qz quartz, and silica glass) based on Raman spectral maps shown in (d) and (e).

Fig. S18. Pyroxene compositions in NWA 14672 match those of shergottite NWA 12335 (Orr et al., 2022), except for late ferroan phases.

Fig. S19. BSE Map of genomict eucrite breccia NWA 10784 showing shock melt vein (light grey)and location of detail images a, b, c. (a) Fine-grained melt vein with maskelynite schlieren (dark grey) and rounded pyroxene crystal clasts (off white). (b) Part of vein with 10-20 μm plagioclase needles. (c) Shocked pigeonite with displaced augite lamellae.

Fig. S20. Fractional crystallization trends calculated using PETROLOG, for plagioclase and pyroxene in the barred plagioclase component, and for olivine or olivine and pyroxene in the glass with dendrites. The two liquids are clearly generated independently.

Fig S21. Baddeleyite (white).

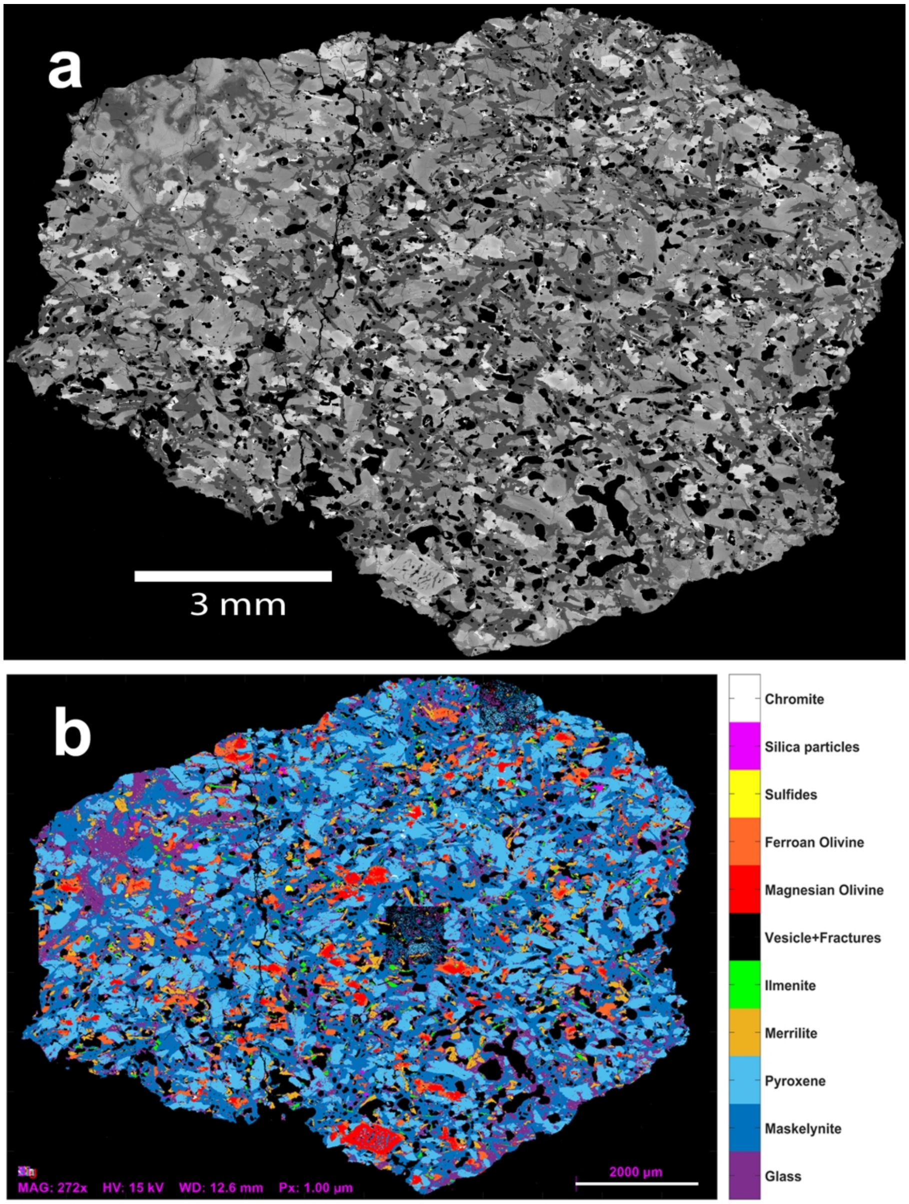

Fig. 1. (a) BSE map of NWA 14672. Olivine off-white; pyroxene light grey; feldspar dark grey; vesicles black. (b) Phase map. Olivine red-orange; pyroxene light blue. Feldspar (dark blue with vesicles black) and fine-grained components (“glass”, purple) are seen throughout.

170x225mm (300 x 300 DPI)

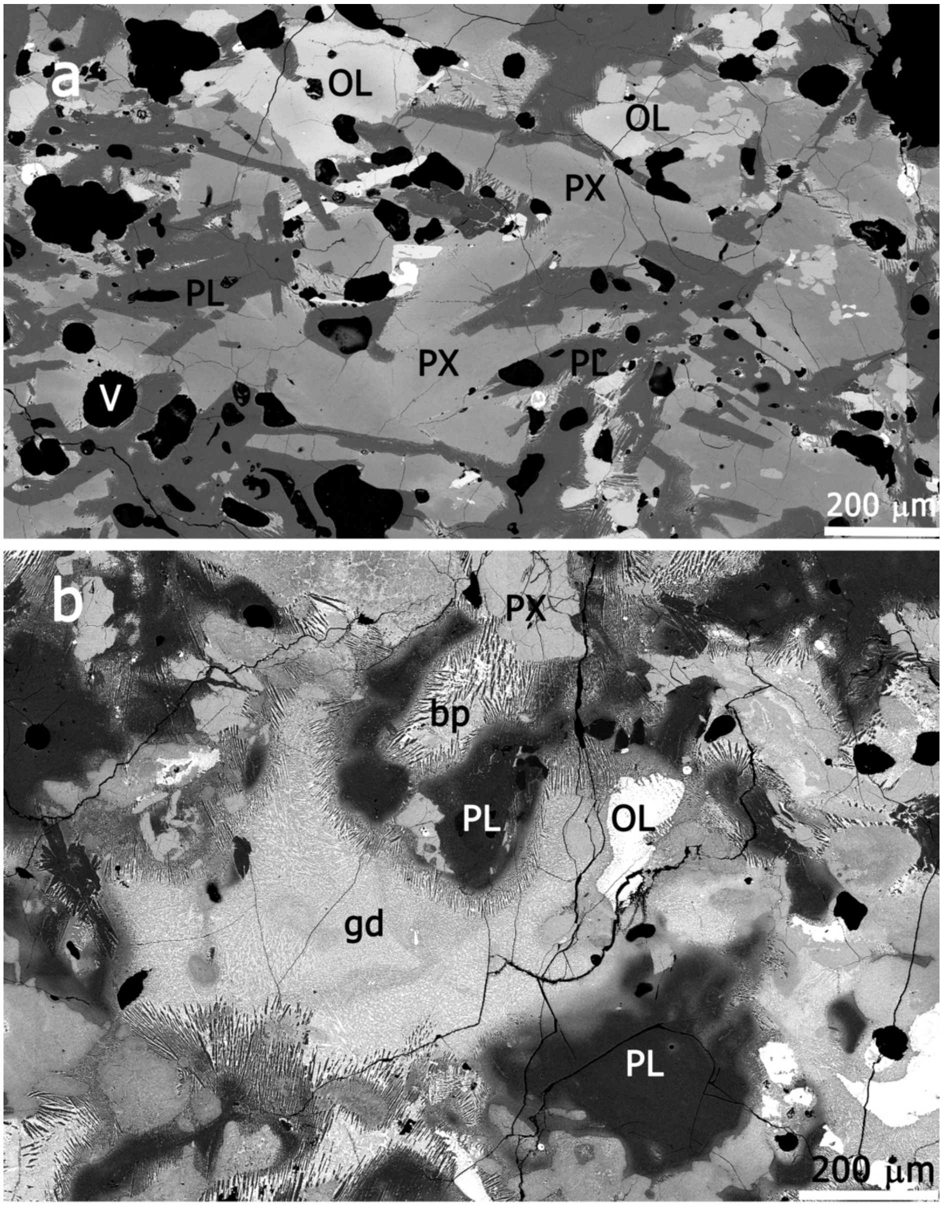

Fig. 2. BSE images. (a) Coarse-grained: vesicules (V) in plagioclase (PL), ophitic pyroxene (PX) and irregular olivine (OL). (b) Fine-grained: areas of glass with ferroan olivine dendrites (gd) and areas with feldspar bars (bp); also maskelynite/plagioclase (PL) patches, pyroxene and olivine.

170x217mm (300 x 300 DPI)

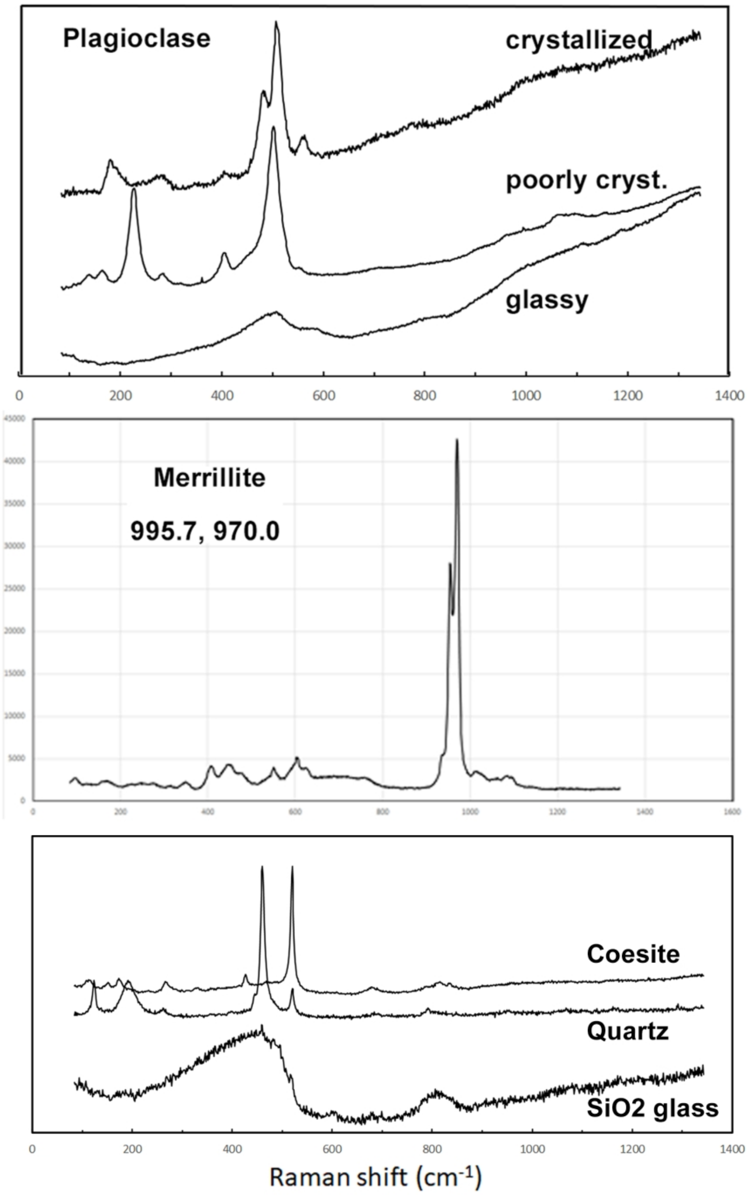

Fig. 3 Raman spectra of selected phases.

170x263mm (300 x 300 DPI)

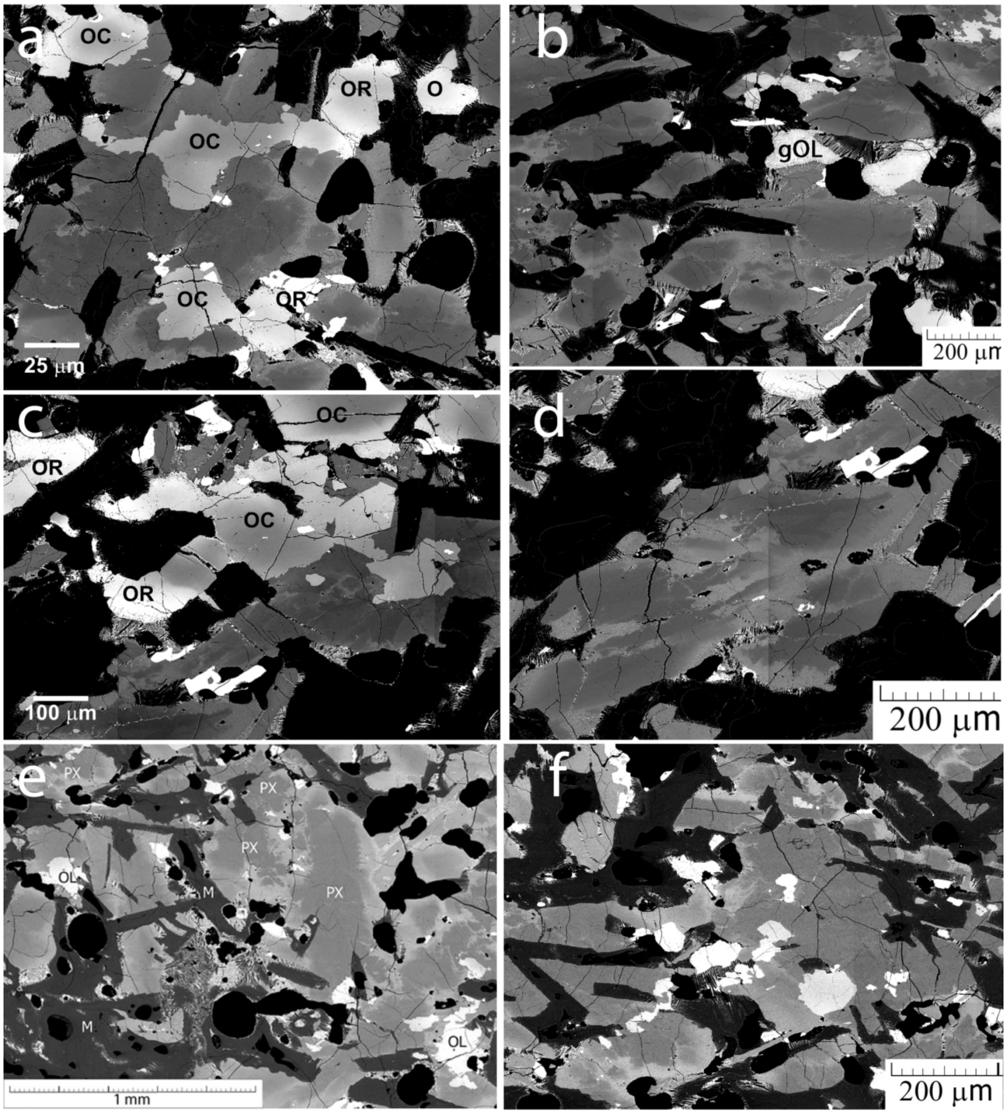

Fig. 4. BSE images showing olivine and pyroxene zonation and relationships. Olivine (OC cores, medium grey and OR rims, white), both anhedral (a) and euhedral (c) is partly enclosed by pyroxene (patchy, dark grey - medium grey). (b,d) Patchy pyroxene with irregular "cores" embedded in ferroan pigeonite, and granular olivine. (e) Plagioclase (M), vesicles, anhedral olivine (OL), patchy pyroxene(PX), invaded by barred olivine and glass containing olivine dendrites. (f) Irregular distribution of small anhedral olivine grains.

169x187mm (300 x 300 DPI)

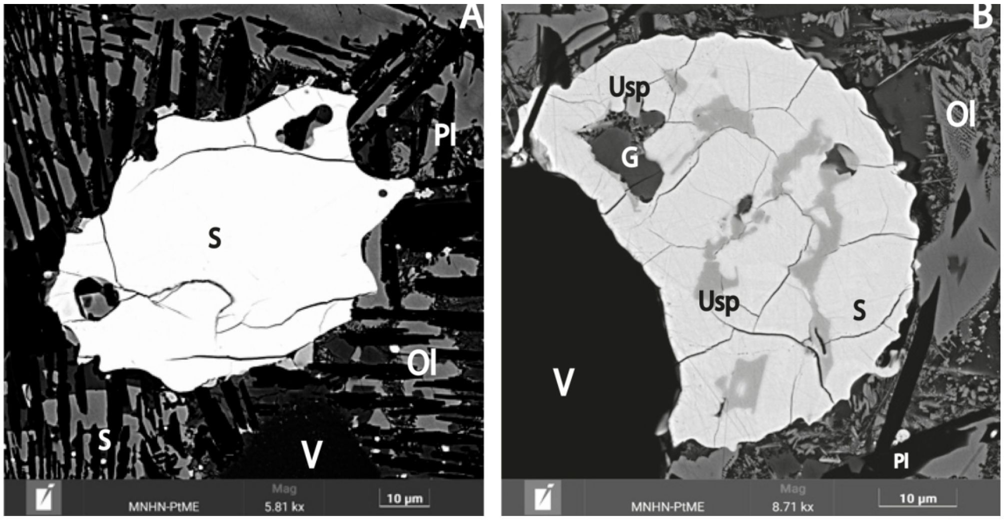

Fig. 5. BSE images of Fe sulfides (A) A rare sulfide grain (S) with scalloped indentations like those in most shergottites and micron-size sulfide (S) in barred plagioclase (Pl), with interstitial P-rich olivine (Ol), pyroxene and vesicles (V)). (B) A sulfide spherule attached to a vesicle (V), in glass with olivine dendrites (Ol) and plagioclase bars) with inclusions of glass (G) and ulvöspinel (Usp inside the sulfide).

170x87mm (300 x 300 DPI)

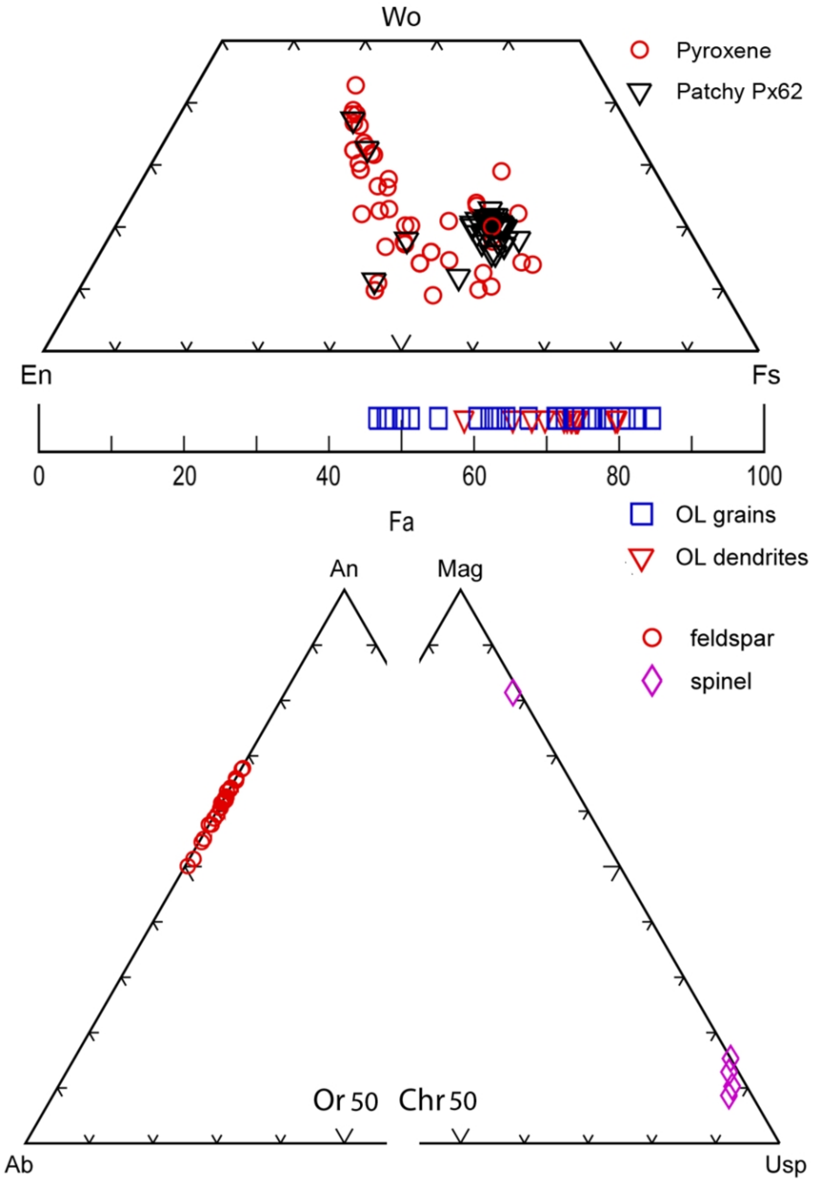

Fig. 6. Compositions of olivine, pyroxene, feldspar, and spinel in NWA 14672. Olivine dendrites include fine olivine associated with barred feldspar.

85x121mm (300 x 300 DPI)

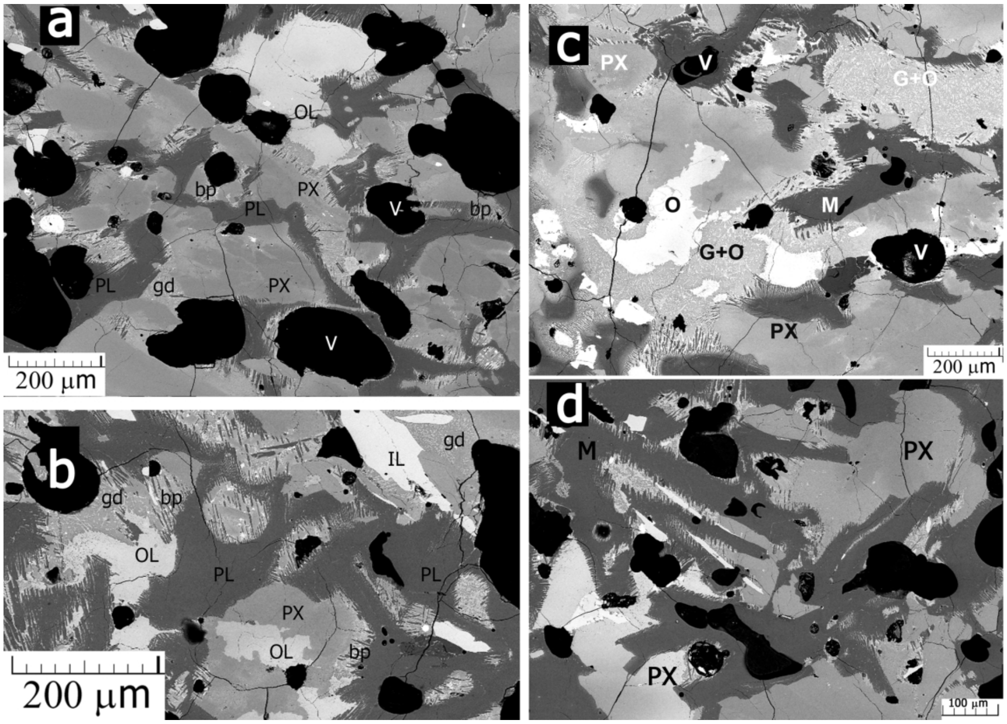

Fig. 7. Barred plagioclase (bp) occurring (a) mainly between 'maskelynite' (PL) and pyroxene (PX and sometimes olivine, OL); (b) also as globules containing pyroxene or glass with olivine dendrites (gd) within 'maskelynite'; Il ilmenite, V vesicles; (c) between maskelynite (M) and glass with olivine dendrites (G+O), or pyroxene (PX) and olivine (OL); and (d) within plagioclase enclosed ophitically in pyroxene.

170x121mm (300 x 300 DPI)

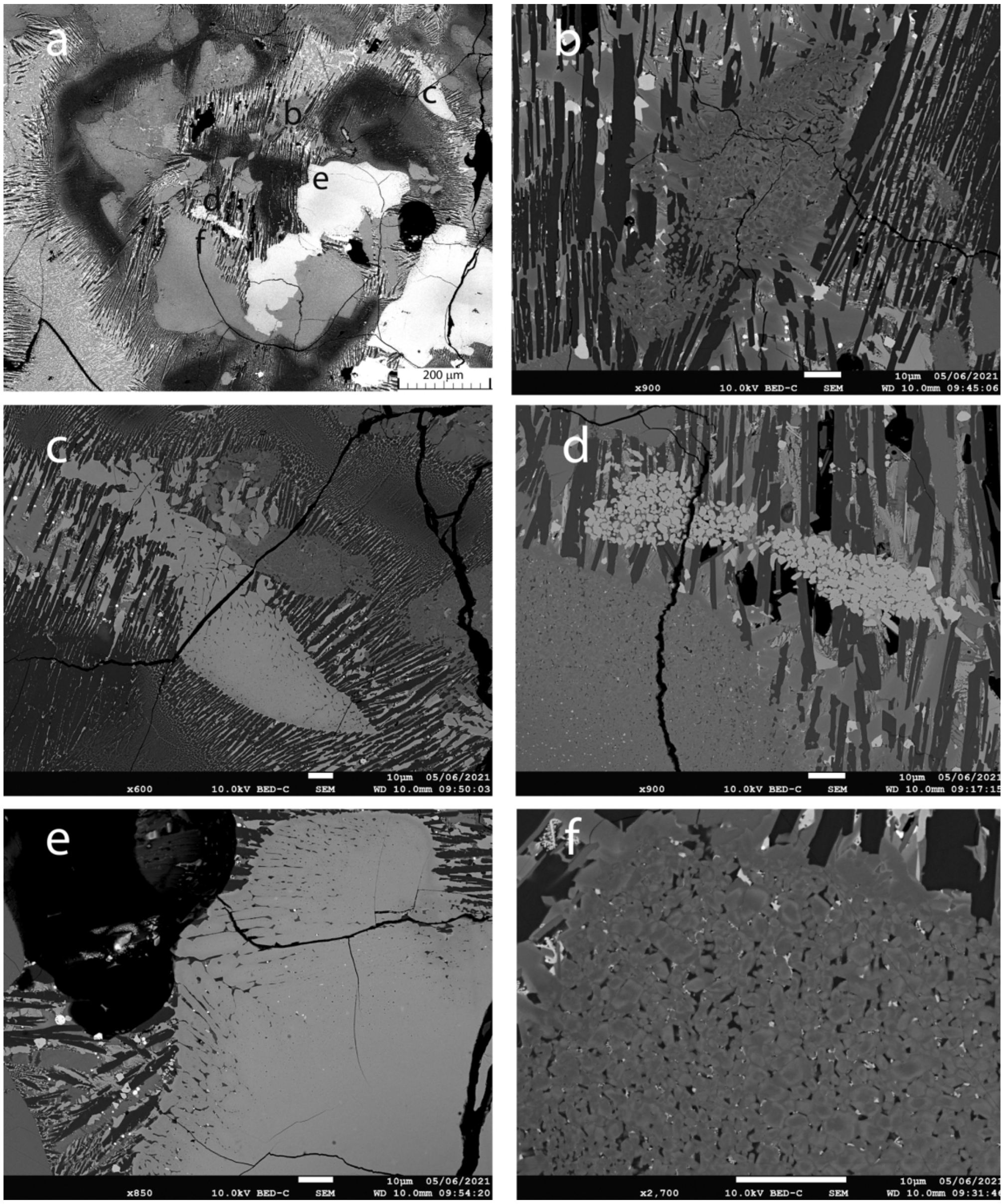

Fig. 8. Crystal morphology in a barred feldspar area. (a) Barred feldspar area surrounded by glass with olivine dendrites, showing locations of details b-g. (b) Aggregate of pyroxene granules overgrown by pyroxene blades interstitial to feldspar bars. (c) Large olivine dendrite associated with olivine interstitial to feldspar bars. (d) aggregate of ilmenite granules within a barred feldspar area. (e) Olivine dendrites overgrowing a mass of porous olivine and protruding into barred feldspar. (f) Detail of pyroxene below ilmenite in (d) showing it is surrounded by feldspar and partly by darker pyroxene.

163x195mm (300 x 300 DPI)

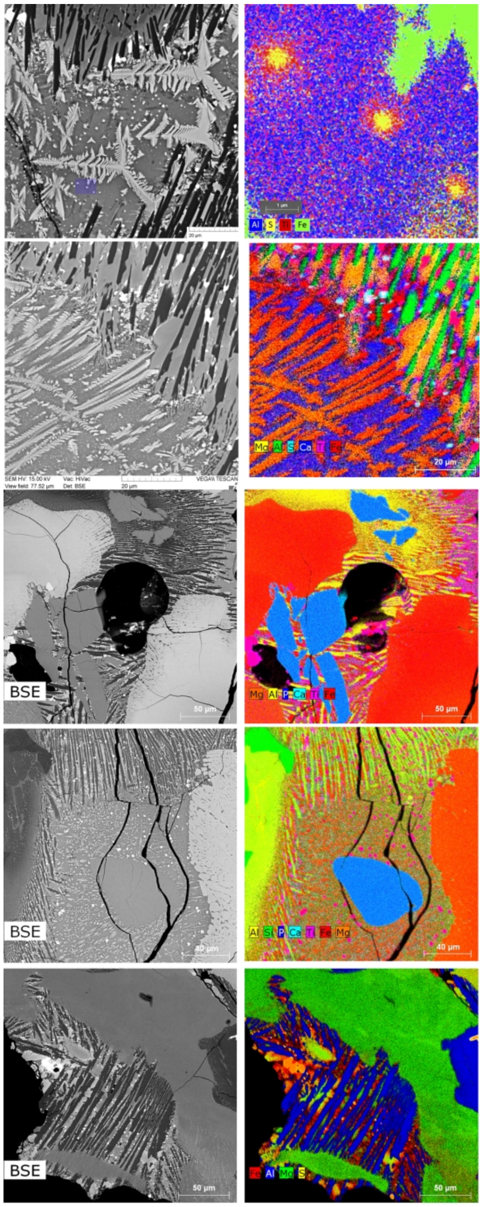

Fig. 9. BSE images (a,c,e,g,i) with olivine (off-white), vesicles and plagioclase bars (black), with basaltic glass, pyroxene, and melilite (all grey), and also ulvöspinel and pyrrhotite, plus the corresponding K□ X-ray images: (b) Enlargement of rectangle in 'a'. Olivine dendrites (green) in glass (blue; pyrrhotite (yellow) surrounded by ulvöspinel (red). (d) Barred plagioclase green, olivine dendrites red, pyroxene orange, glass (bottom) and merrillite (top) dark blue, Fe sulfide light blue, Fe-Ti oxide pink. (f) Olivine (red) as large grains with unresolved overgrowths. Merrillite (light blue) resembles fragments. Plagioclase yellow. (h) Silica green, feldspar yellow, merrillite blue, olivine orange. (j) Feldspar blue, olivine yellow-green, pyroxene green, merrillite black between plagioclase bars.

87x219mm (300 x 300 DPI)

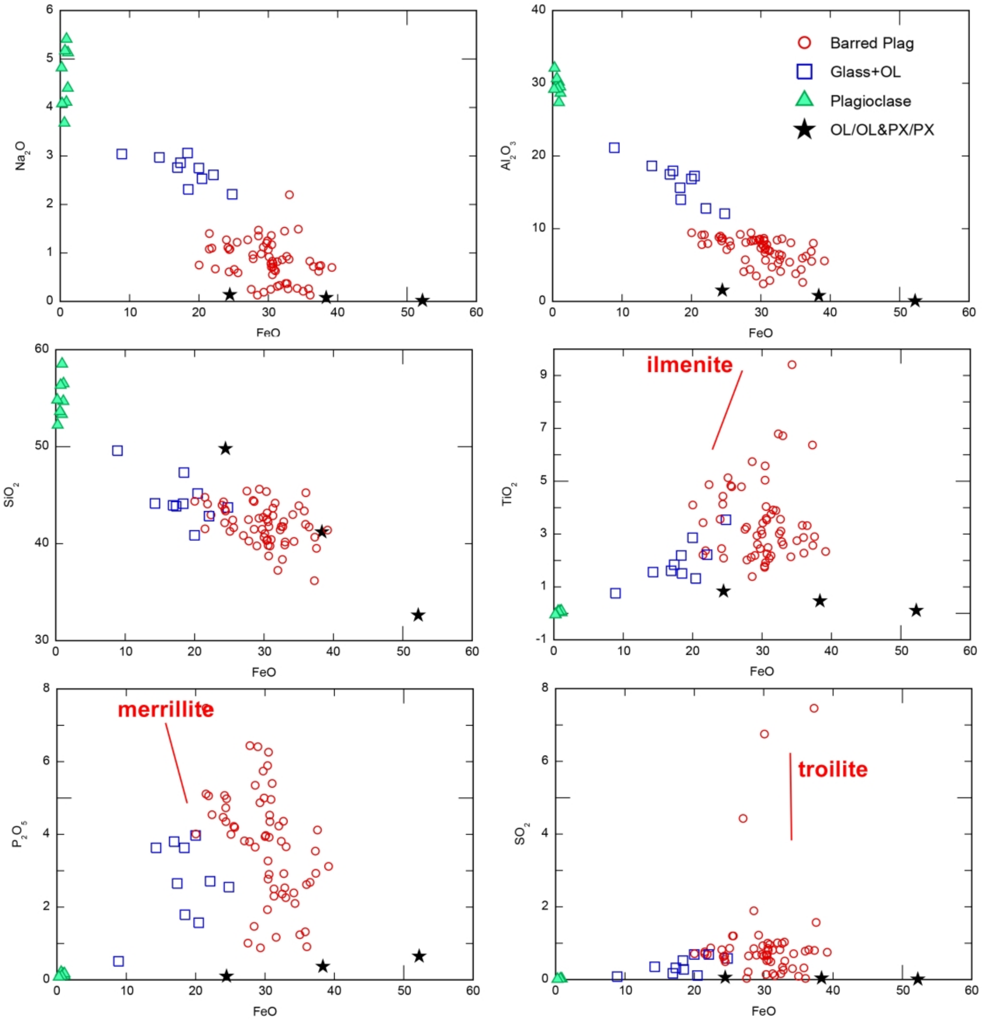

Fig. 10. The major element compositions of the fine-grained components, barred plagioclase and glass with olivine dendrites, reflect melting of plagioclase and a ~50-50 pyroxene-olivine mixture. Deviations from simple mixing indicate the participation of merrillite, ilmenite and Fe_sulfide.

282x289mm (300 x 300 DPI)

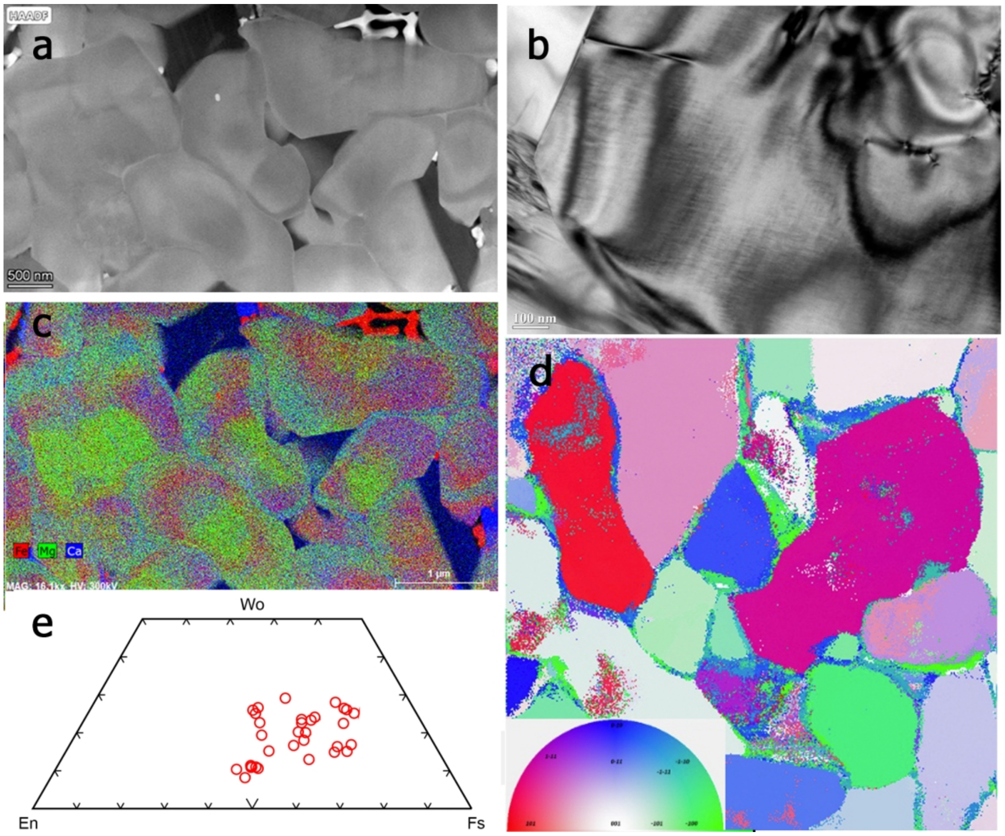

Ca-rich pyroxene (augite) often set in Ca-poor pyroxene (Ca-Mg map, Fig. 12).

159x132mm (300 x 300 DPI)

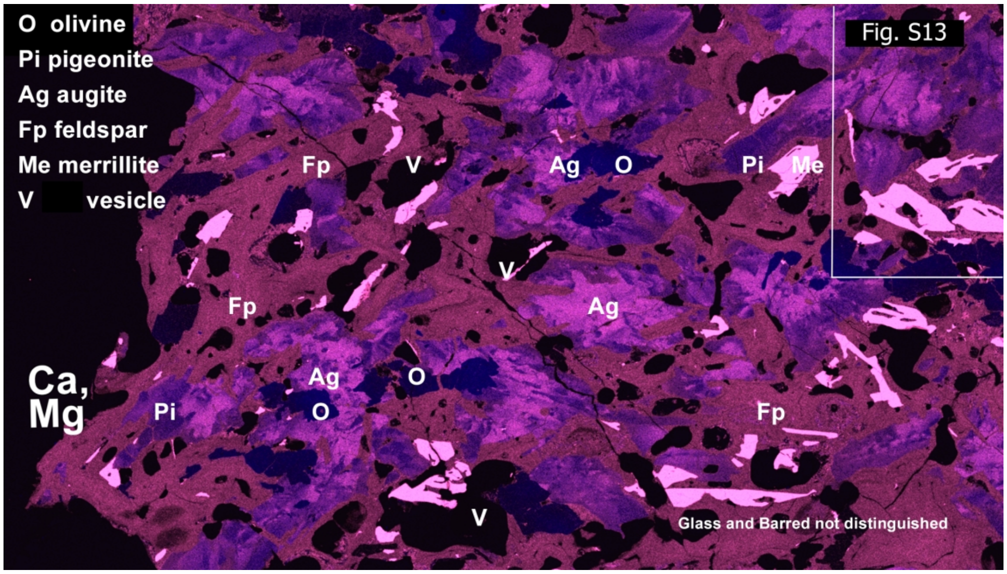

Fig.12. Heterogeneity of patchy pyroxene X-ray map (enhanced, Ca pink-white, Mg blue); glass with olivine and barred plagioclase are hard to distinguish from maskelynite (pinkish).

180x101mm (300 x 300 DPI)

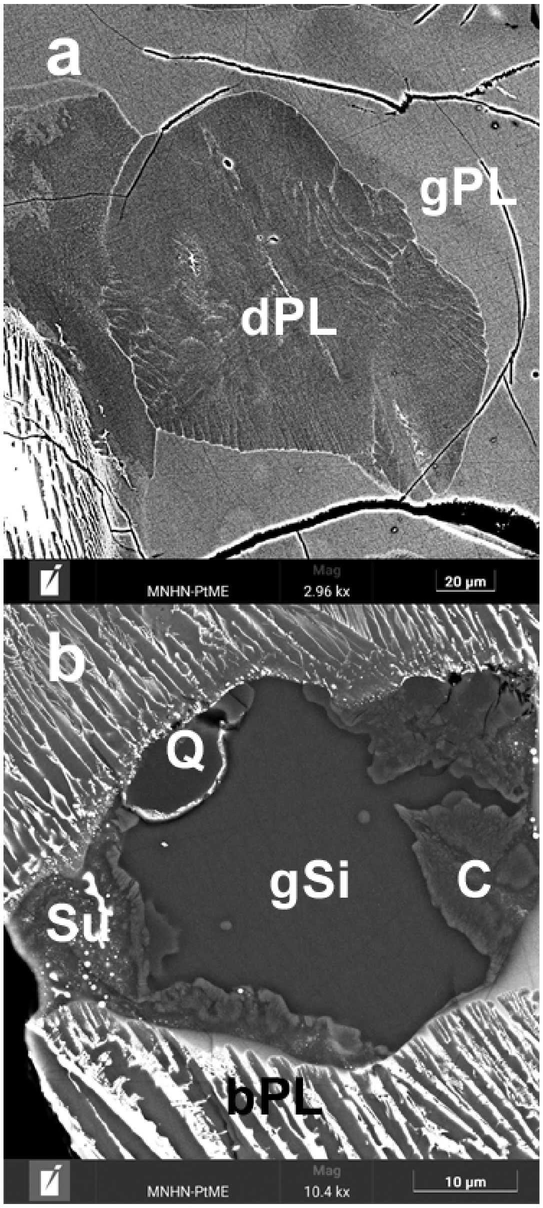

Fig. 13. (a) An aggregate of plagioclase dendrites (dPL) set in plagioclase glass (gPL). (b) Coesite (C) and quartz (Q) grown on the margins of a silica glass (gSi) particle in barred plagioclase (bPL).

131x293mm (72 x 72 DPI)

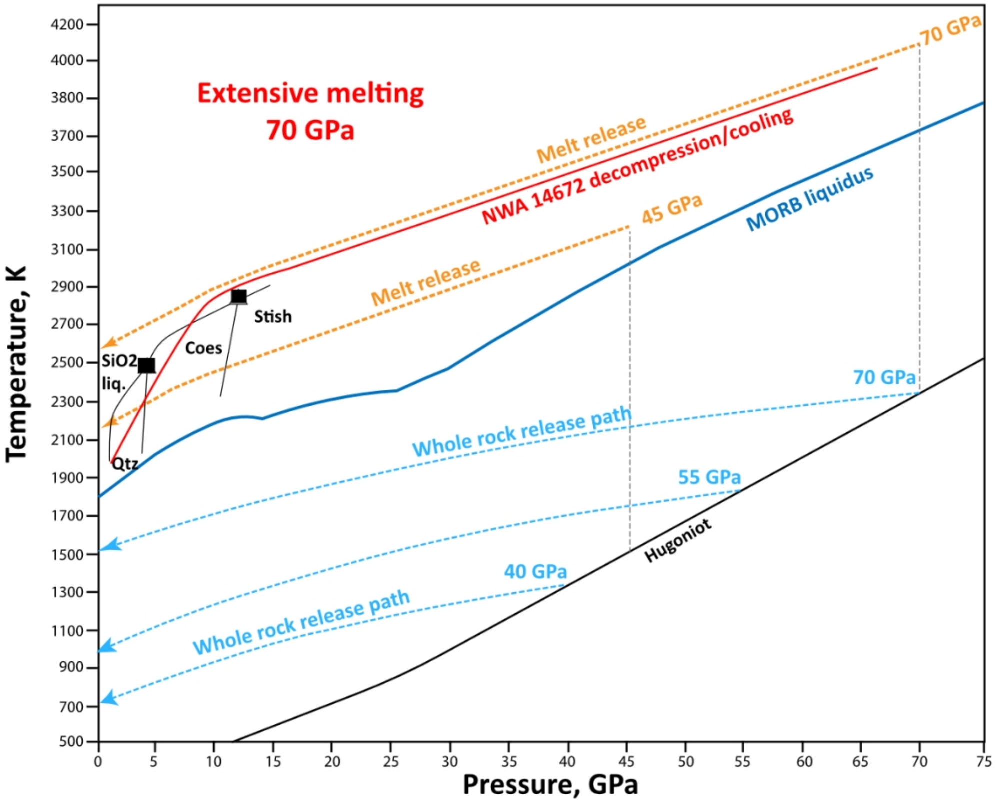

Fig. 14. Schematic diagram for the decompression path of NWA 14672 for a peak pressure >65 GPa with release curve for the melt fraction extrapolated from Hu and Sharp (2022). This path passes through the stability fields of liquid silica, coesite, and then quartz (Kayama et al., 2018).

352x282mm (96 x 96 DPI)

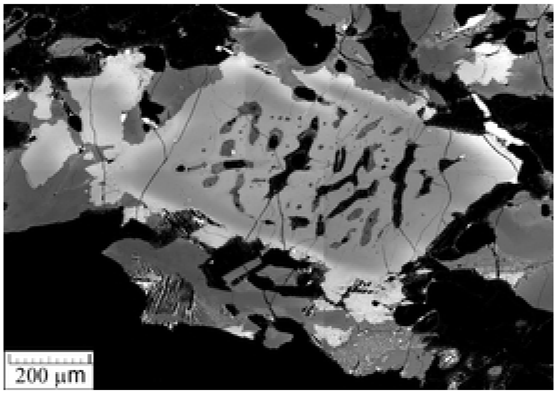

11x8mm (600 x 600 DPI)

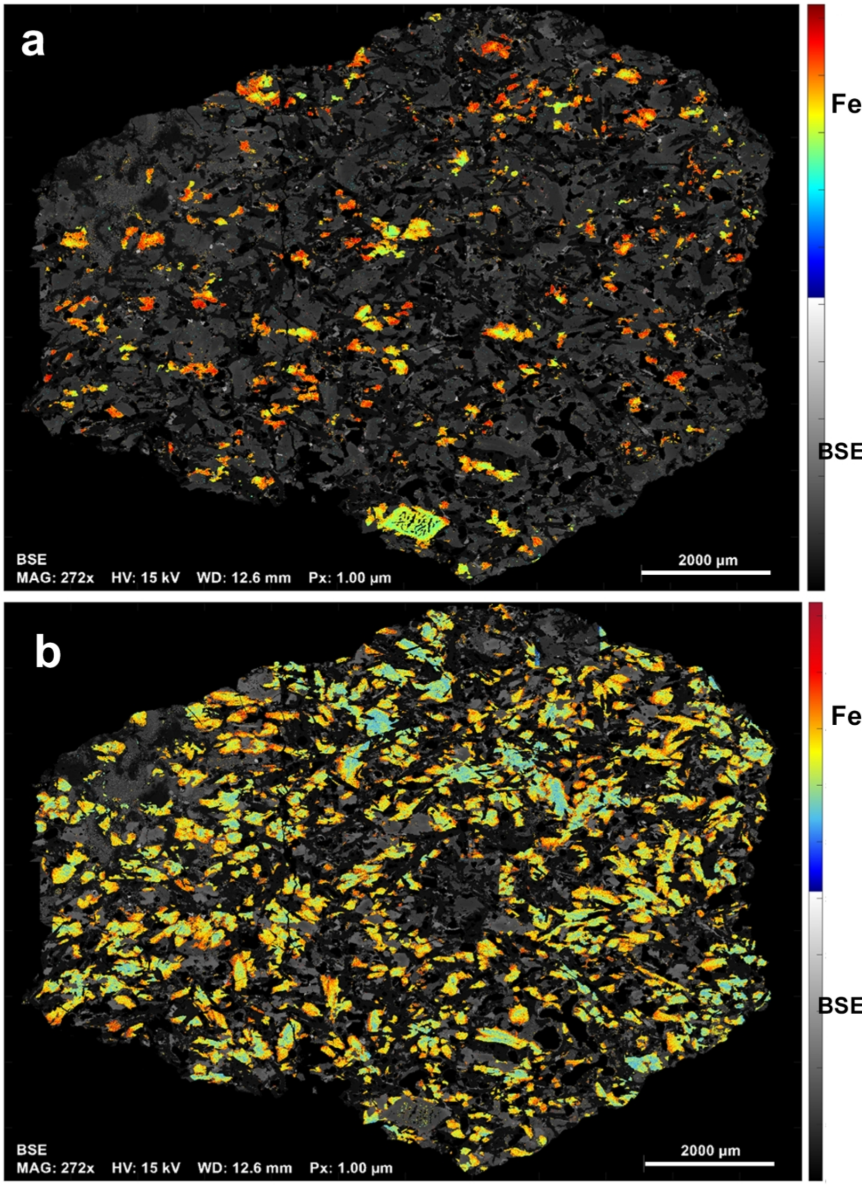

160x219mm (300 x 300 DPI)

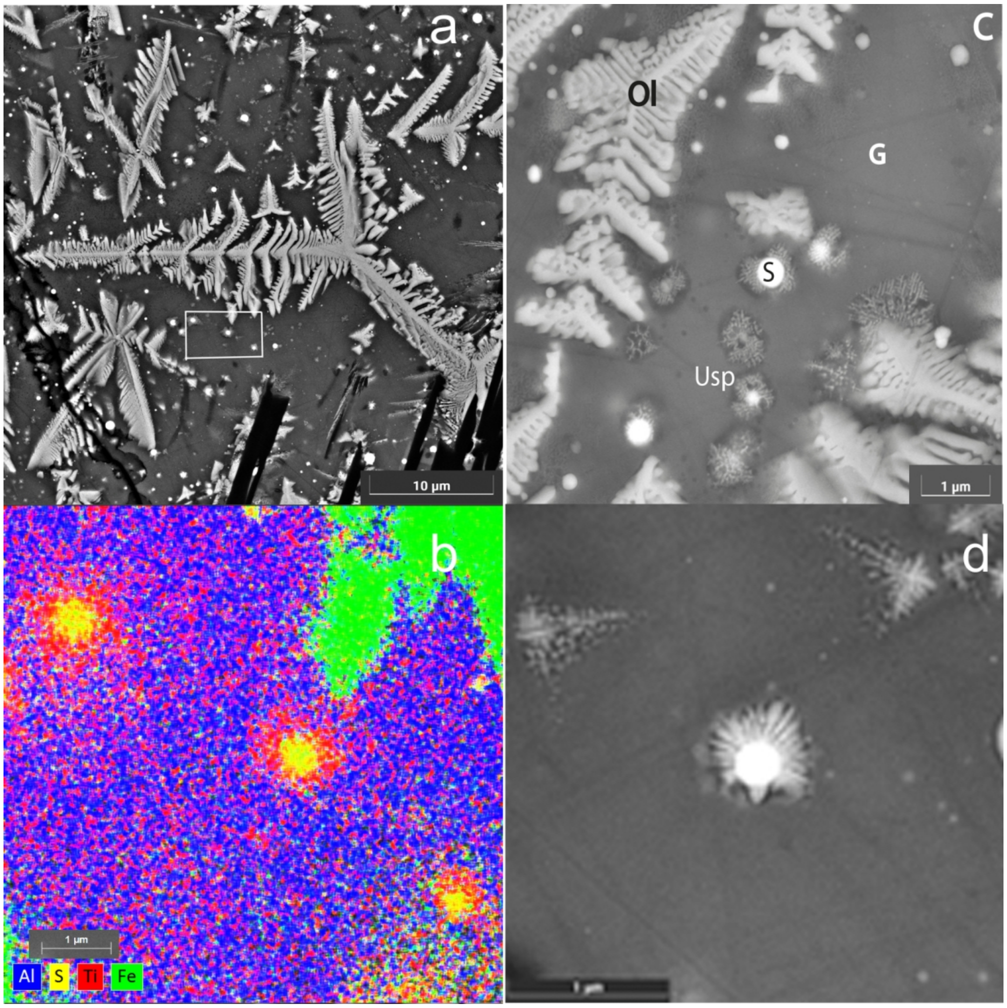

140x140mm (300 x 300 DPI)

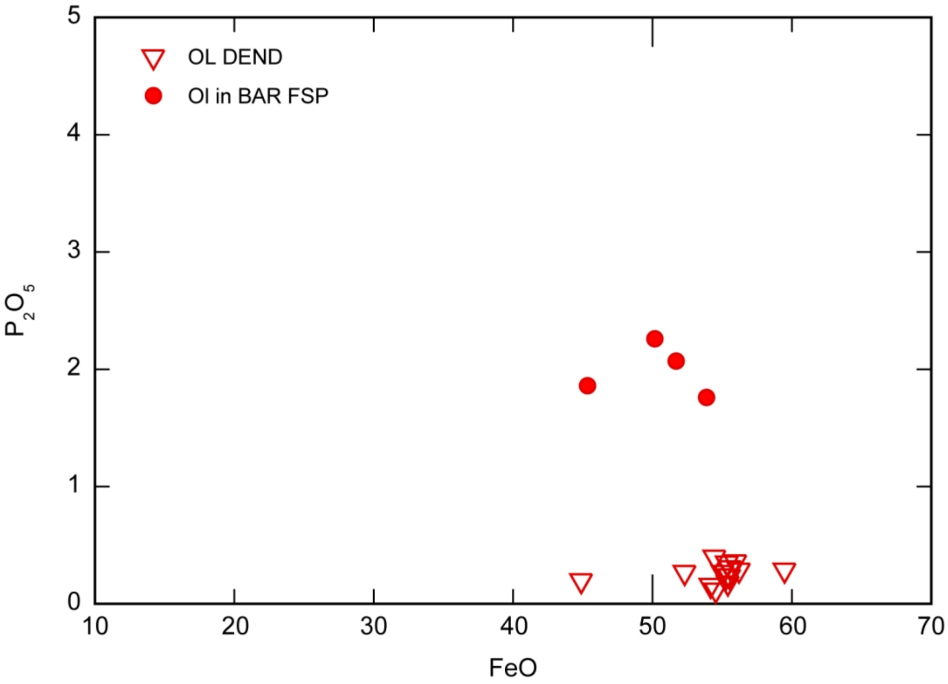

140x97mm (300 x 300 DPI)

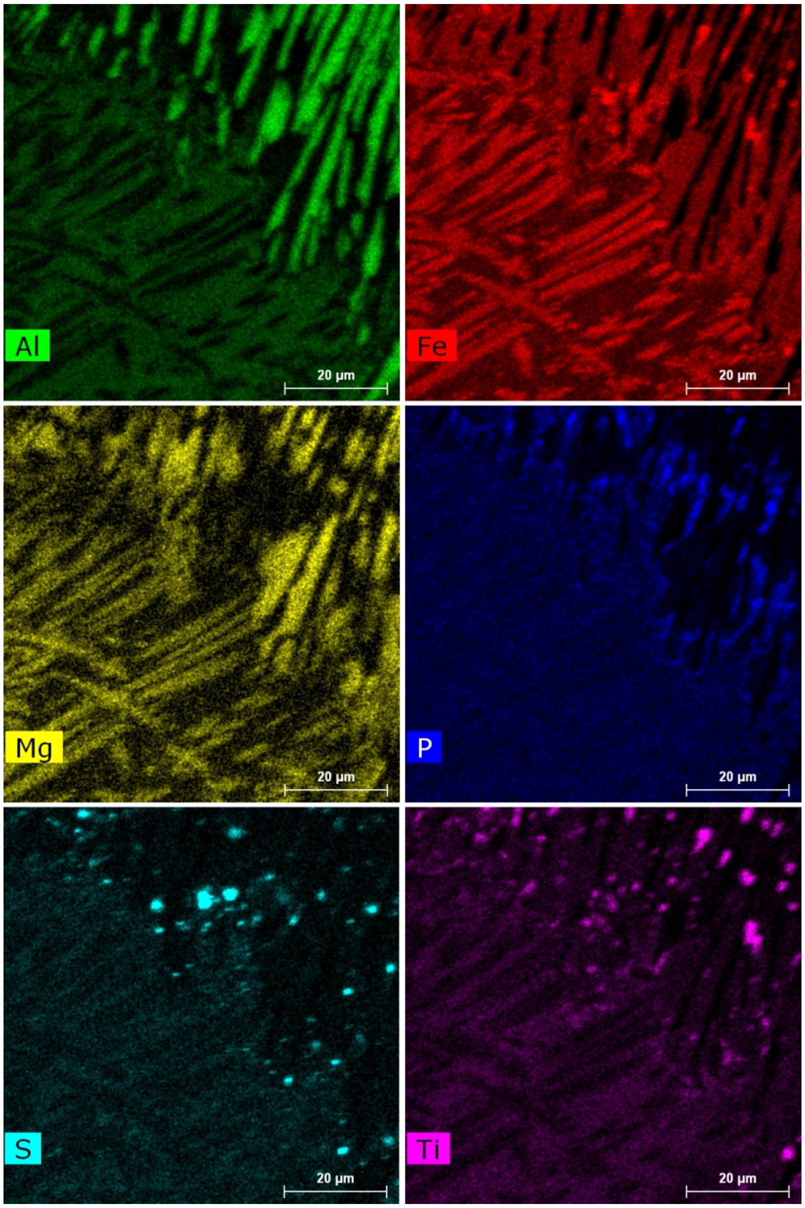

426x639mm (72 x 72 DPI)

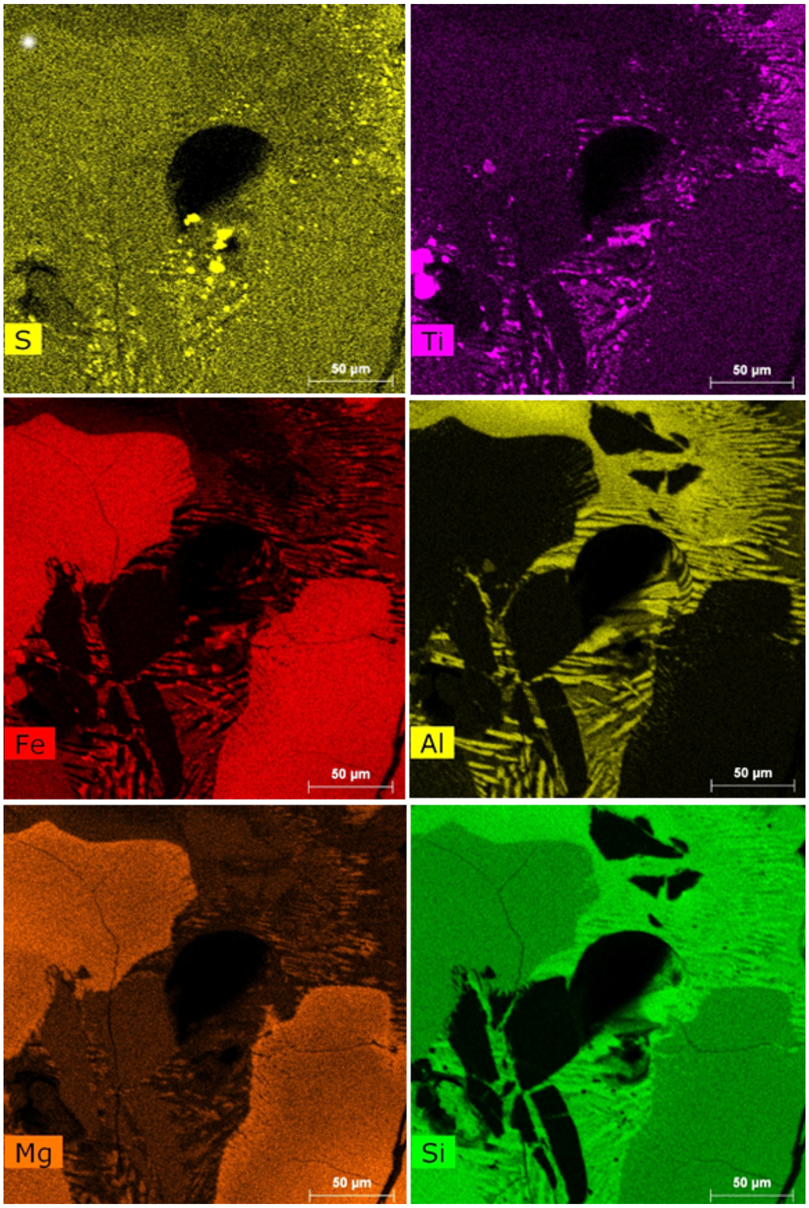

204x305mm (72 x 72 DPI)

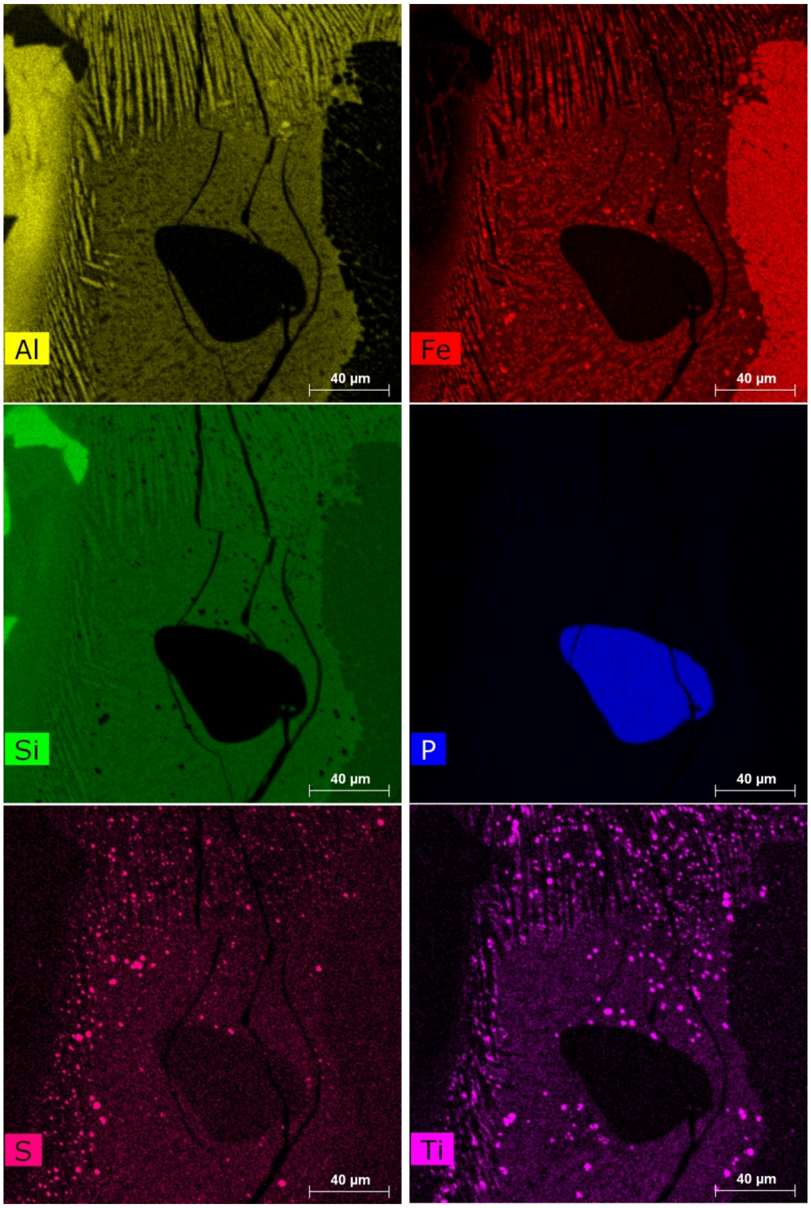

570x849mm (72 x 72 DPI)

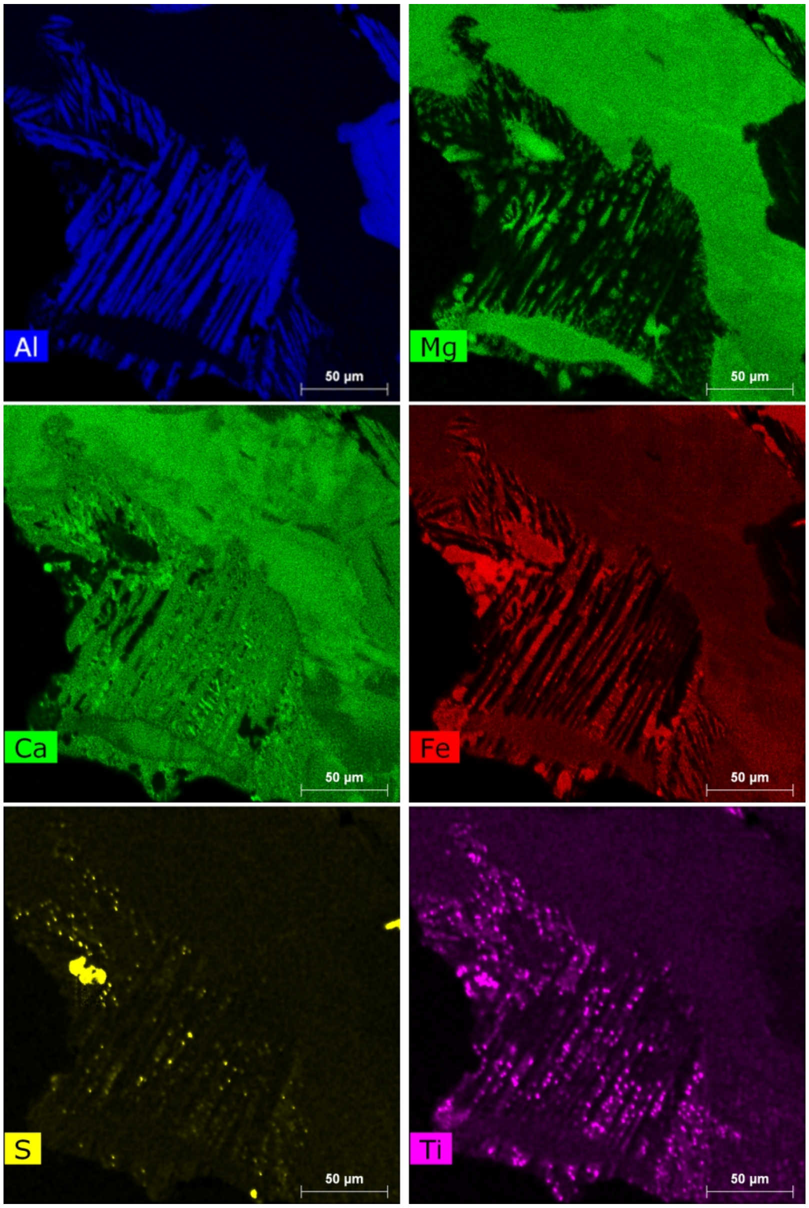

570x850mm (72 x 72 DPI)

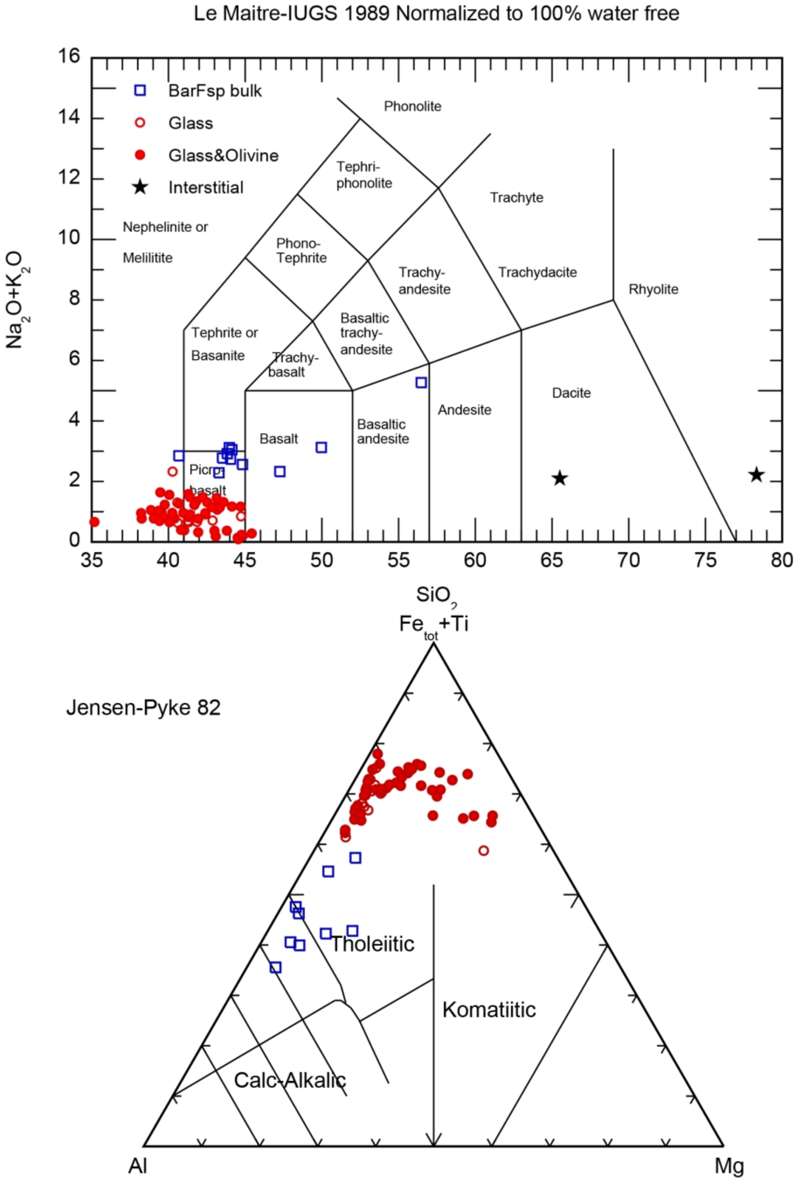

133x196mm (300 x 300 DPI)

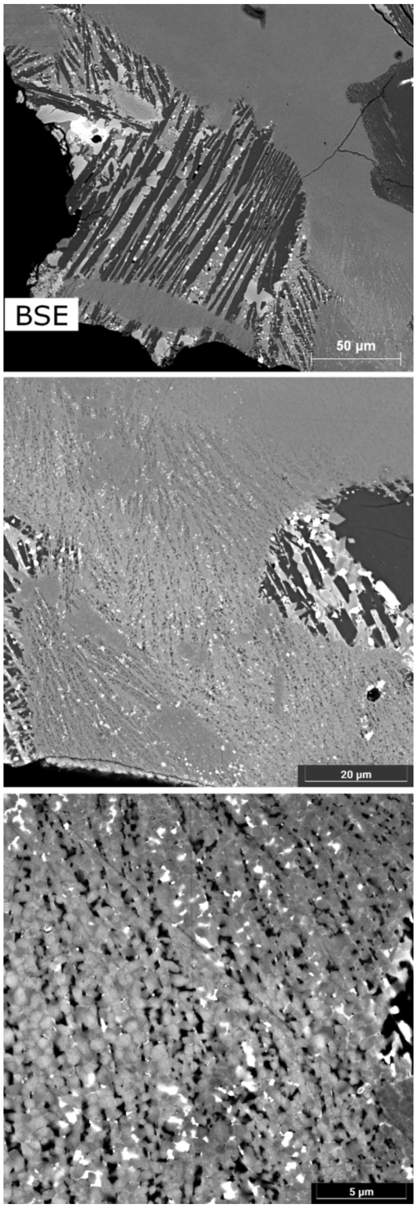

70x204mm (300 x 300 DPI)

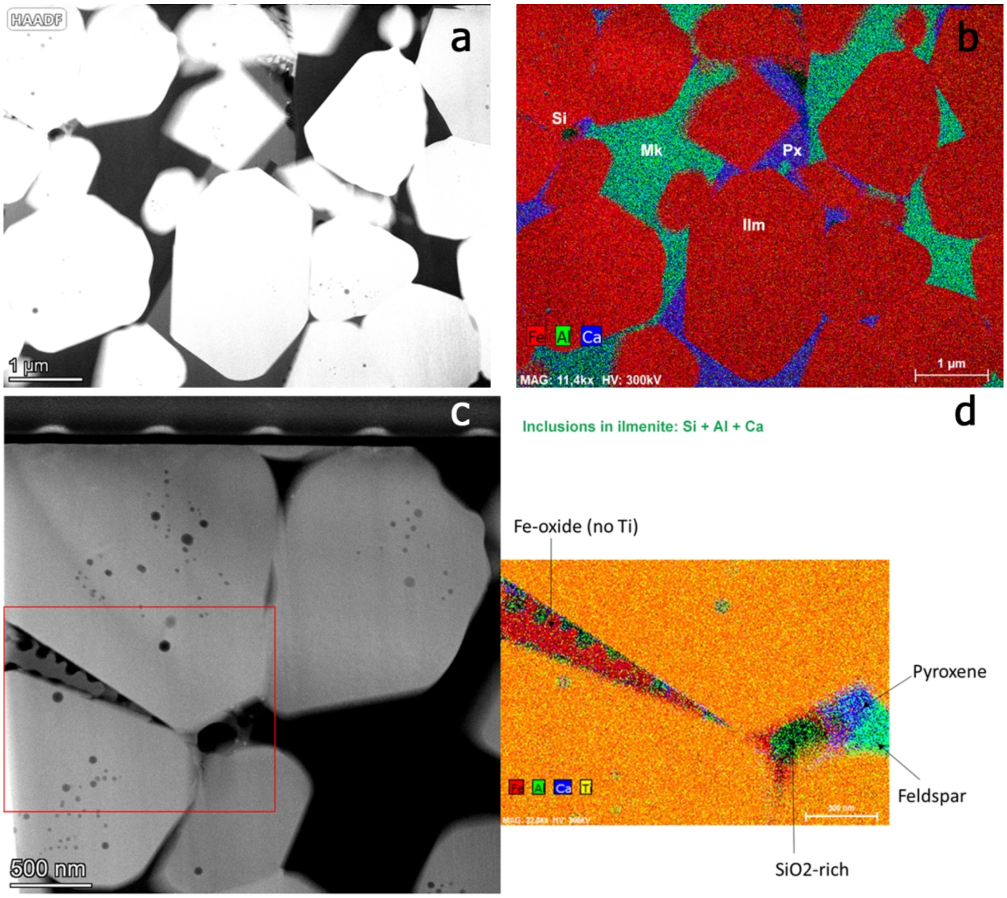

160x142mm (300 x 300 DPI)

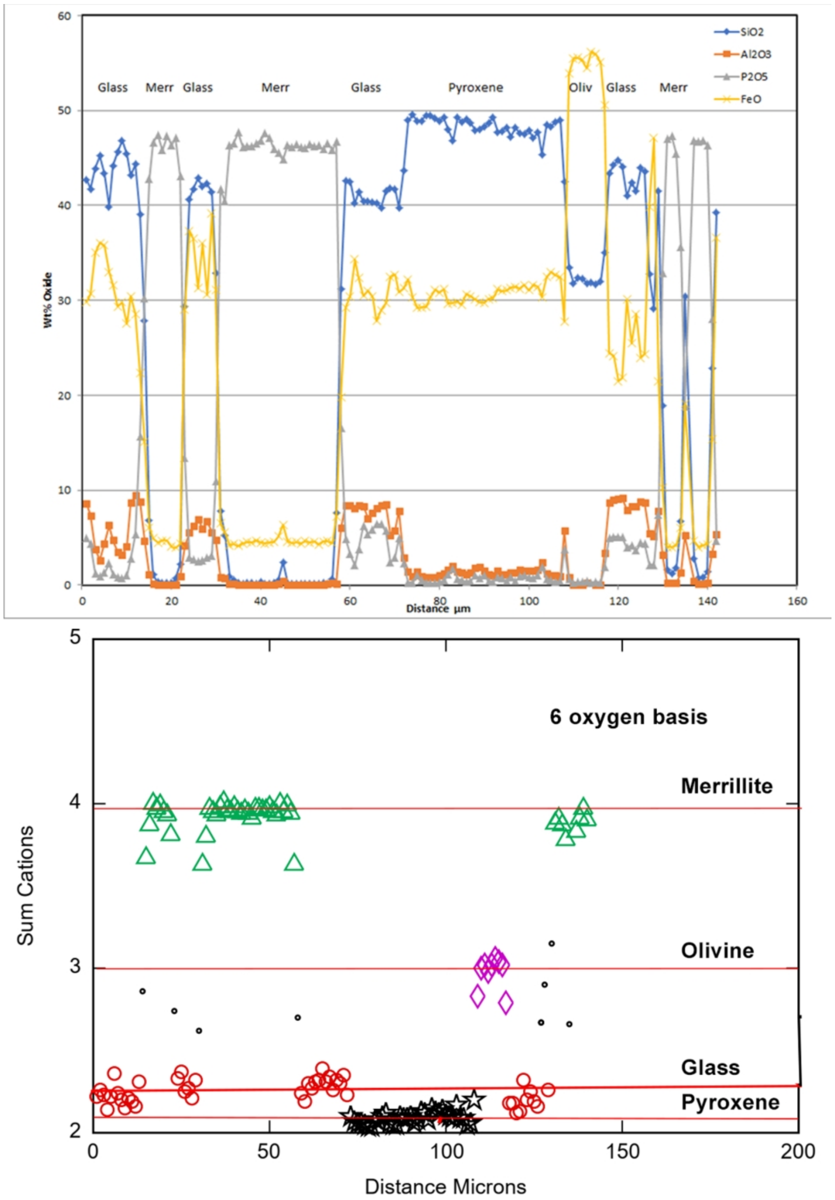

140x202mm (300 x 300 DPI)

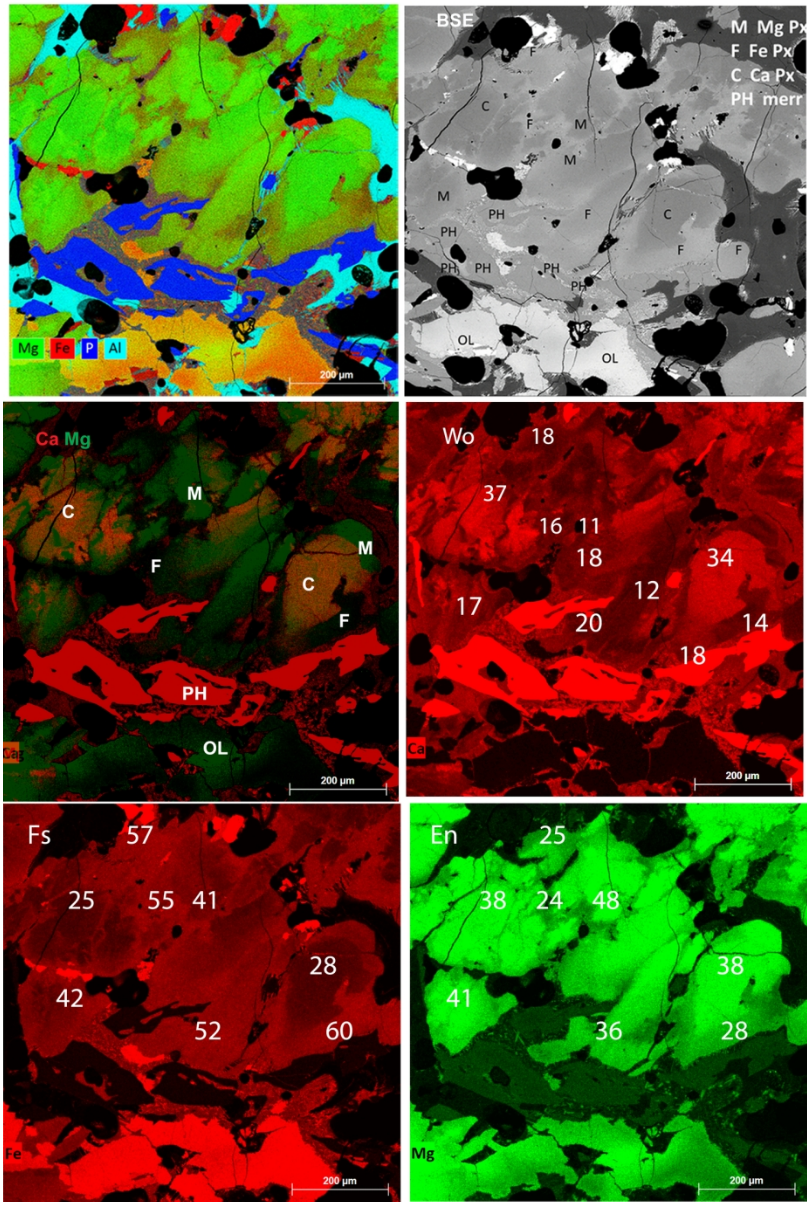

124x186mm (300 x 300 DPI)

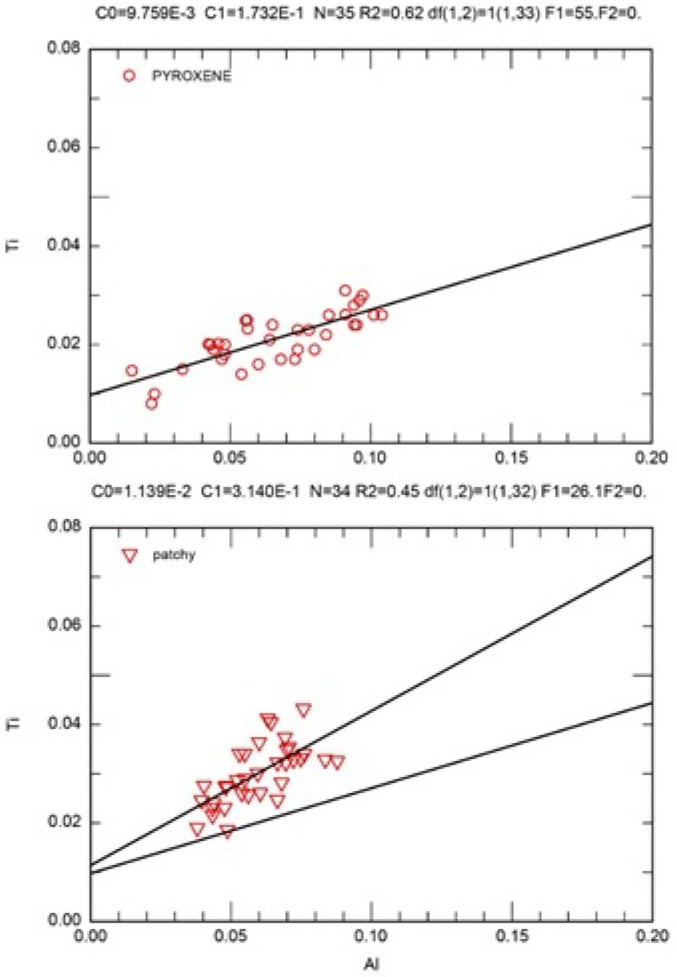

93x132mm (96 x 96 DPI)

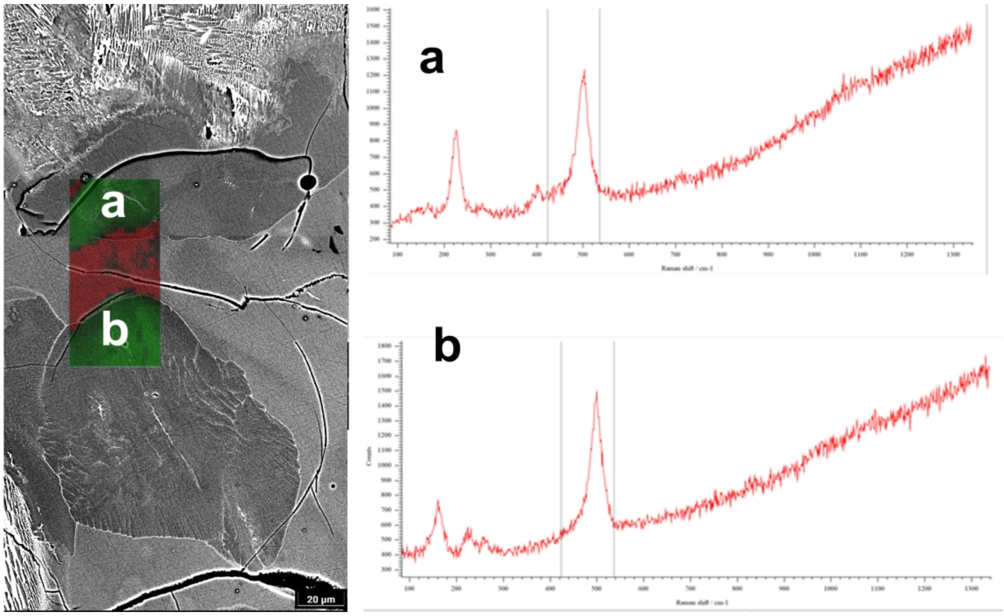

263x160mm (300 x 300 DPI)

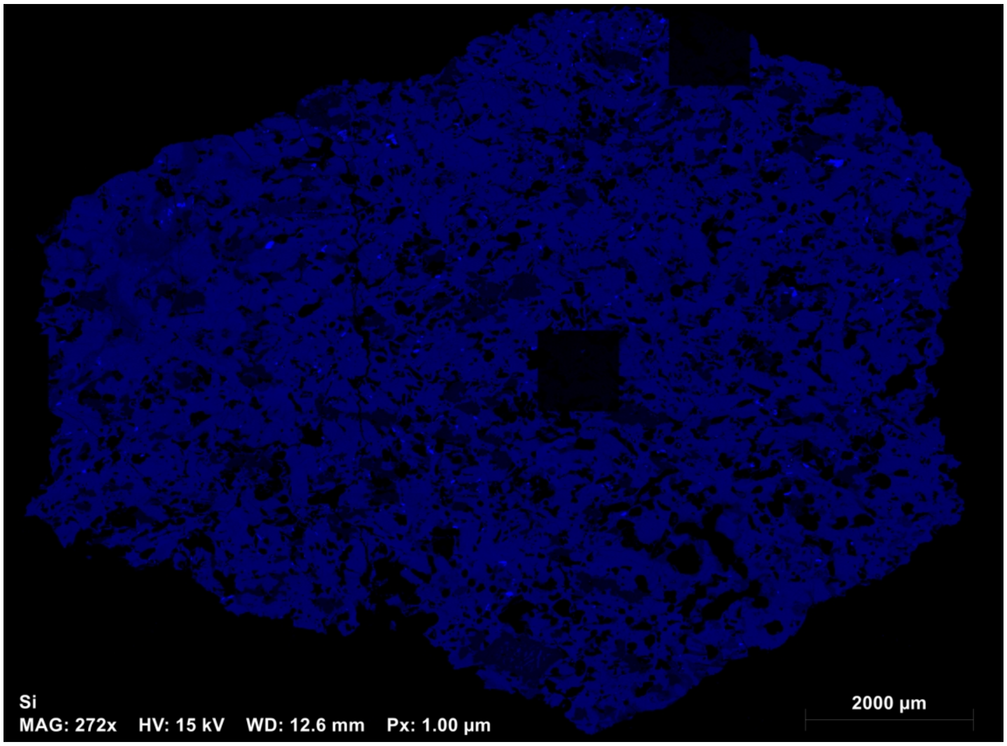

169x125mm (300 x 300 DPI)

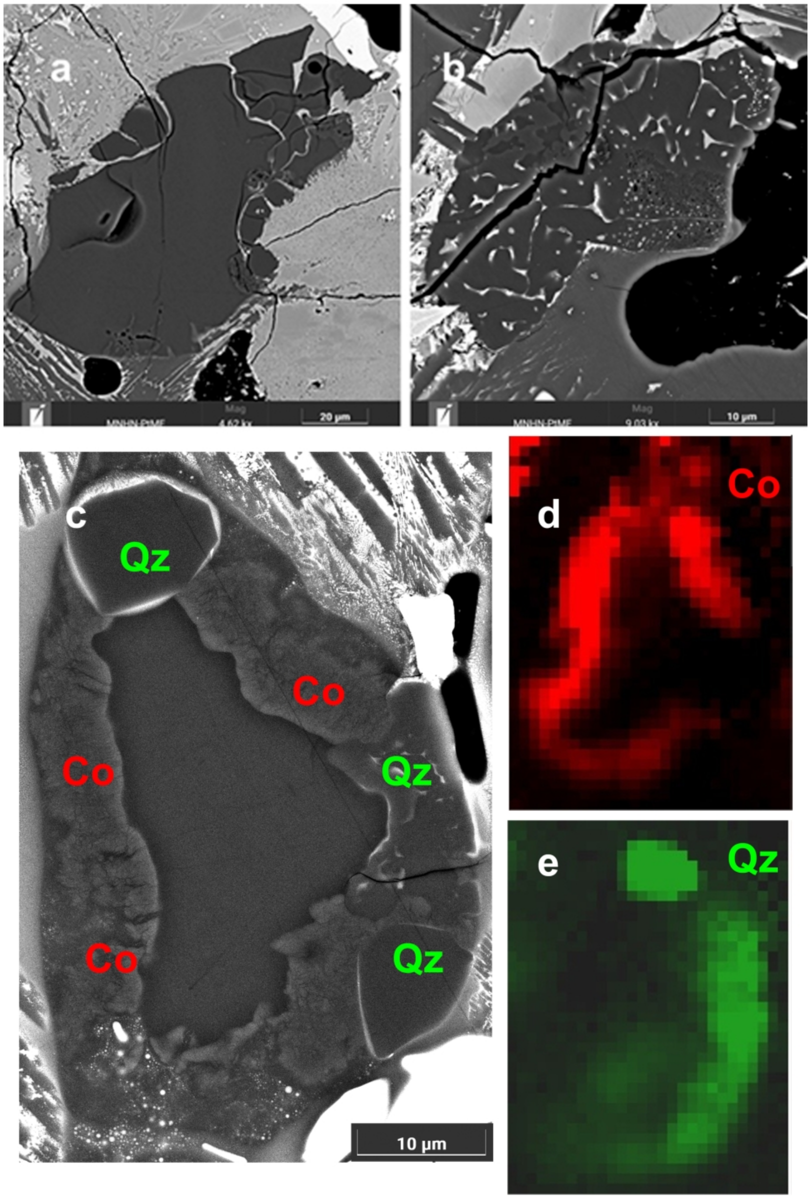

170x253mm (300 x 300 DPI)

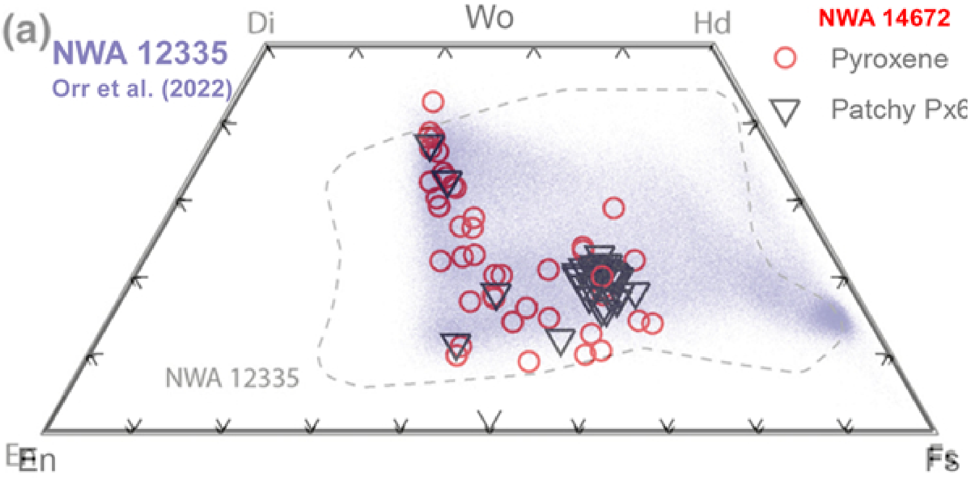

163x82mm (96 x 96 DPI)

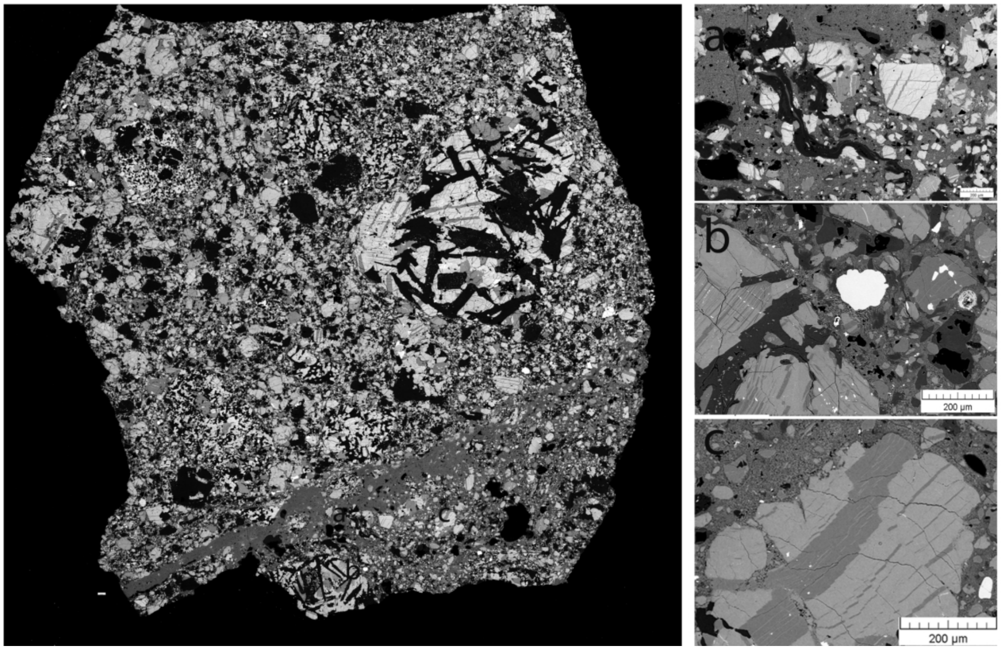

171x110mm (300 x 300 DPI)

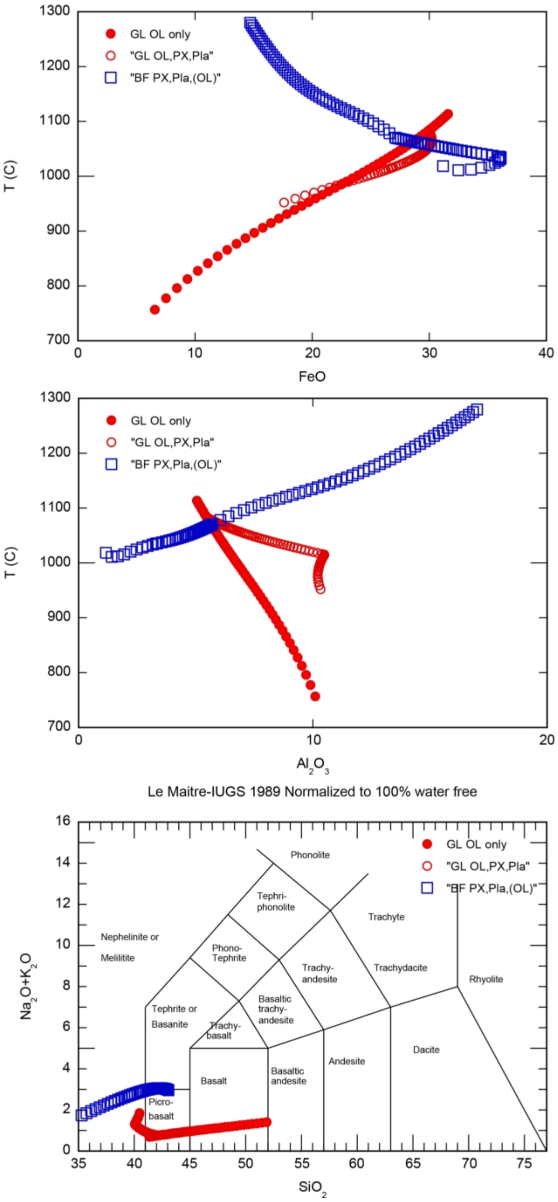

141x299mm (300 x 300 DPI)

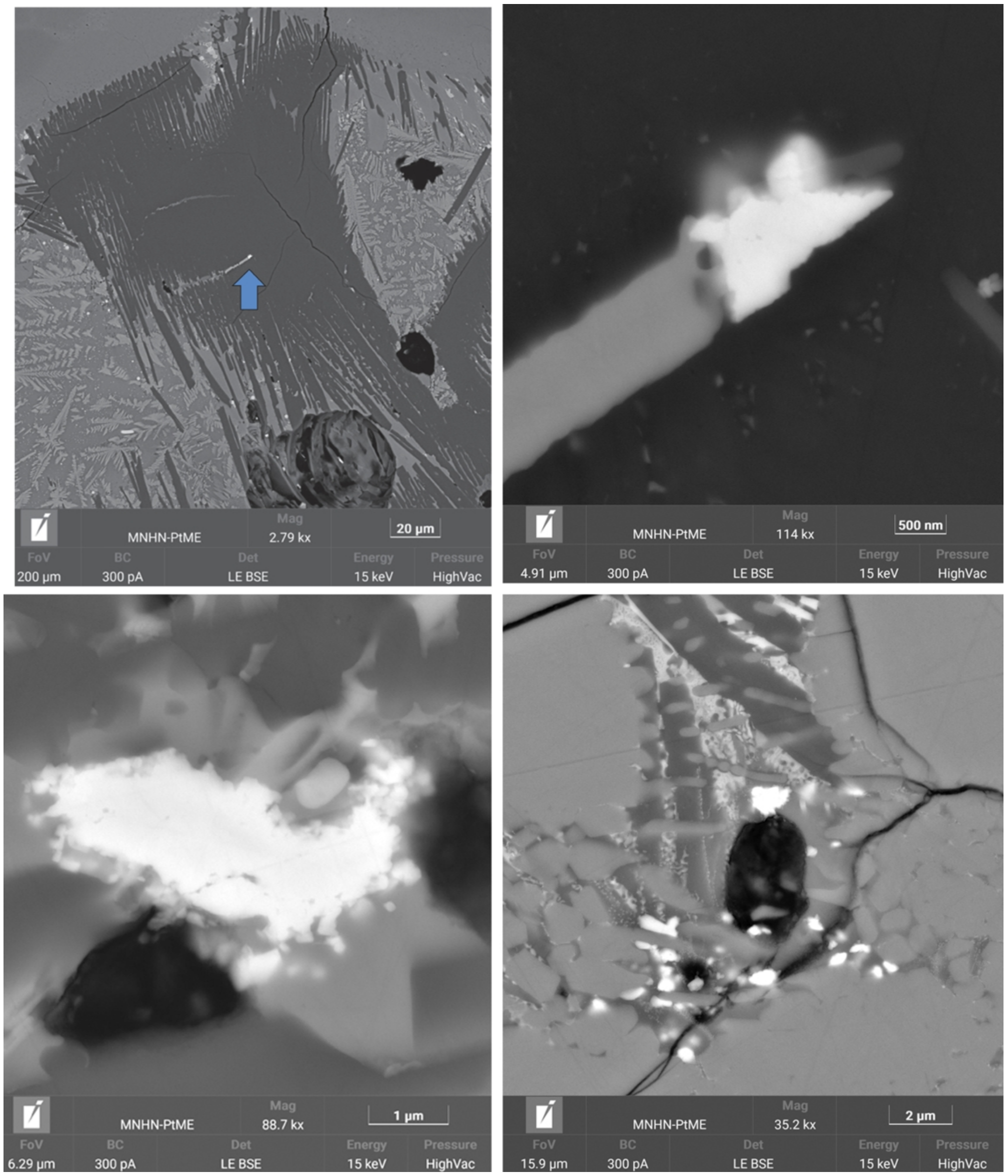

213x250mm (300 x 300 DPI)